INVESTIGATING THE FAR- AND NEAR-FIELD THERMAL

RADIATION IN CARBON-BASED NANOMATERIALS

A Dissertation
Presented to
The Academic Faculty

By

Zihao Zhang

In Partial Fulfillment
Of the Requirements for the Degree of
Doctor of Philosophy in the
George W. Woodruff School of Mechanical Engineering

Georgia Institute of Technology

December 2015

INVESTIGATING THE FAR- AND NEAR-FIELD THERMAL

RADIATION IN CARBON-BASED NANOMATERIALS

Approved by:

Dr. Zhuomin Zhang, Advisor
George W. Woodruff School of
Mechanical Engineering
Georgia Institute of Technology

Dr. Yogendra Joshi
George W. Woodruff School of
Mechanical Engineering
Georgia Institute of Technology

Dr. Satish Kumar
George W. Woodruff School of
Mechanical Engineering
Georgia Institute of Technology

Dr. Wenshan Cai
School of Electrical and
Computer Engineering
Georgia Institute of Technology

Dr. Andrew Peterson
School of Electrical and
Computer Engineering
Georgia Institute of Technology

Date Approved: September 30, 2015

ACKNOWLEDGEMENTS

TABLE OF CONTENTS

LIST OF TABLES

LIST OF FIGURES

NOMENCLATURE

Variables

A	Absorptance
A	Amplitude of forward wave from a forward emitting source
B	Amplitude of backward wave from a forward emitting source
C	Amplitude of forward wave from a backward emitting source
C_G	Gate capacitance, F/m^2
$\hat{\mathbf{c}}$	Optical axis
D	Amplitude of backward wave from a backward emitting source
$\mathbf{D}$	Transmission matrix
d	Layer or film thickness, m
f	Filling ratio
G	Fermi-Dirac difference function
g	Weyl component of electric Dyadic Green's function
H	Near-field gap distance, m
h	Weyl component of magnetic Dyadic Green's function
k_0	Wavevector in vacuum, rad/m
k_x	x component of the wavevector, rad/m
k_z	z component of the wavevector, rad/m
N	Number of periods
n	Refractive index
$\mathbf{P}$	Propagation matrix
Q	Heat flux, W/m^2

Q'	Spectral heat flux (J/m^2-rad)
R	Reflectance
r	Fresnel reflection coefficient
S	Poynting vector
T	Transmittance
T	Temperature, K
t	Fresnel transmission coefficient
v_F	Fermi velocity, m/s
V_G	Gate voltage, V
z	z-axis coordinate

Greek Symbols

α	Gradient ratio
β	Array tilting angle, degrees
γ	z component of the wavevector in vacuum, rad/m
Δ	Thickness of filament or sheet, m
δ	Penetration depth, m
ε	Dielectric function
$\in$	Emissivity
ϕ	Radiation azimuthal angle, degrees
η	Integrating variable, eV
Θ	Planck energy oscillator function, J
θ	Radiation polar angle, degrees

κ	Extinction coefficient
Λ	Period size, m
λ	Wavelength, m
μ	Chemical potential, eV
ν	Frequency, cm^{-1}
ξ	Alignment factor
σ	Sheet conductivity, S/m
$\mathcal{T}$	Near-field transmission coefficient
τ	Relaxation time, s
Ω	Solid angle, sr
ω	Angular frequency, rad/s

Superscripts and Subscripts

B	Brewster (angle)
BB	Blackbody
cr	Critical wavevector
d	Dielectric layer
E	Extraordinary
eph	Electron-phonon
g	Graphene
h	Host medium
Inter	Interband
Intra	Intraband

i	Incidence
j	Index
m	Metal layer
m	Source layer
n	Non-emitting layer
O	Ordinary
op	Optical phonon
P	Principal (angle)
p	TM wave polarization
s	TE wave polarization
ρ, θ, or z	Cylindrical coordinates for Green's dyadic function components
‖	Parallel to optical axis
⊥	Perpendicular to optical axis

Universal Constants

ε_0	Vacuum permittivity, 8.854×10^{-12} F/m
eV	Electronvolt, 1.602×10^{-19} J
$\hbar$	Reduced Planck's constant, 1.055×10^{-34} J·s
k_B	Boltzmann constant, 1.381×10^{-23} J/K
μ_0	Vacuum permeability, $4\pi \times 10^{-7}$ N/A^2
q	Elementary charge of electron, 1.602×10^{-19} C

Abbreviations

BB	Blackbody
CNT	Carbon nanotube
EMT	Effective medium theory
ENZ	Epsilon-near-zero
ESL	Energy streamline
HMM	Hyperbolic metamaterial
TACNT	Tilt-aligned carbon nanotube
TE	Transverse electric
TM	Transverse magnetic
TPV	Thermophotovoltaic
VACNT	Vertically aligned carbon nanotube

SUMMARY

Two classes of carbon nanomaterials—carbon nanotubes and graphene—have promoted the advancement of nanoelectronics, quantum computing, chemical sensing and storage, thermal management, and optoelectronic components. Studies of the thermal radiative properties of carbon nanotube thin film arrays and simple graphene hybrid structures reveal some of the most exciting characteristic electromagnetic interactions of an unusual sort of material, called hyperbolic metamaterials. The features and results on these materials in the context of both far-field and near-field radiation are presented in this dissertation.

Due to the optically dark nature of pyrolytic carbon in the wavelength range from visible to infrared, it has been suggested vertically aligned carbon nanotube (VACNT) coatings may serve as effective radiative absorbers. The spectral optical constants of VACNT are modeled using the effective medium theory (EMT), which is based on the anisotropic permittivity components of graphite. The effects of other EMT parameters such as volume filling ratio and local filament alignment factor are explored. Low reflectance and high absorptance are observed up to the far-infrared and wide range of oblique incidence angles. The radiative properties of tilt-aligned carbon nanotube (TACNT) thin films are illustrated. Energy streamlines by tracing the Poynting vectors are used to show a self-collimation effect within the TACNT thin films, meaning infrared light can be transmitted along the axes of CNT filaments.

Graphene, a single layer sheet of carbon atoms, produces variable conductance in the terahertz frequency regime by tailoring the applied voltage gating or doping. Periodically embedding between dielectric spacers, the substitution of graphene provides

low radiative attenuation compared to traditional metal-dielectric multilayers. The hyperbolic nature, namely negative angle of refraction, is tested on the graphene-dielectric multilayers imposed with varying levels of doping. EMT should be valid for graphene-dielectric multilayers due to the nanometers-thick layers compared to the characteristic wavelength of infrared light. For metal- or semiconductor-dielectric multilayers with thicker or lossier layers, EMT may not hold. The validity of EMT for these multilayers is better understood by comparing against the radiative properties determined by layered medium optics.

When bodies of different temperatures are separated by a nanometers-size vacuum gap, thermal radiation is enhanced several-fold over that of blackbodies. This phenomenon can be used to develop more efficient thermophotovoltaic devices. Due to their hyperbolic nature, VACNT and graphite are demonstrated to further increase evanescent wave tunneling. The heat flux between these materials separated by vacuum gaps smaller than a micron is vastly improved over traditional semiconductor materials. A hybrid structure composed of VACNT substrates covered by doped graphene is analyzed and is shown to further improve the heat flux, due to the surface plasmon polariton coupling between the graphene sheets.

CHAPTER 1

INTRODUCTION

The Lycurgus Cup, created around 300 A.D. during the Roman Empire, is possibly one of the earliest pieces of photonic metamaterials containing nanoscale materials [1]. The presence of fine gold dust, identified today as nanoparticles, gives the translucent artifact a yellow-green hue when illuminated from behind, but appears red when looking through the glass. In 1908, Gustav Mie used Maxwell's electromagnetic theory to explain this phenomenon: The size of the nanoparticles affects the wavelength of radiative absorption bands, called plasma oscillation (plasmon) resonance [2,3]. The understanding on how light interacts with subwavelength structures, or nanostructures, has just recently ignited theoretical and technological developments in engineering, physics, biology, and more. Among the examples are metallic nanoparticles called quantum dots for biomolecular imaging [4,5], nanowire/tube arrays for photonic emission and sensing [6-8], and engineered crystals consisting of patterned lattices for optical devices and thermophotovoltaic (TPV) components [9-12].

Carbon, the fourth most abundant element in the universe, holds surprising qualities that may enable renewable production and better sustainability in nanoscale technologies [13-15]. Modern treatments of graphite, such as carbon nanotubes and graphene, have resulted in mechanical and electronic components many orders of magnitude smaller than those produced using traditional semiconductors such as silicon [16,17]. The discovery of these carbon nano-allotropes accelerated the trend of ever-increasing electromechanical capabilities at smaller and smaller length scales. The

1

investigation of optical or thermal radiative properties of such aforementioned nanomaterials may provide solutions for pressing engineering problems, such as waste heat recovery, alternative energy sources, and spacecraft design.

1.1 Carbon Nanomaterials

In 1985, a group at Rice University, only later to become recipients of the Nobel Prize in Chemistry in 1996, discovered a soccer ball-shaped nanoparticle composed of 60 or so carbon atoms [18]. This stable carbon allotrope was called buckminsterfullerene (sometimes fullerene or buckyball), and fueled further developments in graphite-based synthetic chemistry. One of the most notable offsprings of this breakthrough was the carbon nanotube (CNT), first synthesized in 1991 by Sumio Iijima of NEC Corporation in Japan [19]. Composed of concentrically wrapped graphitic carbon sheets, this hollow needle-like tubule possessed surprising properties such as low mass density, mechanical strength, and electric conductivity [20-22]. Since then, CNTs have been incorporated in engineering technologies to exceed capabilities offered by traditional bulk semiconductors [14,23,24]. Applications utilizing CNTs include chemical storage, structural nanocomposites, transistor circuits, thermally conductive interfaces, and more continue to develop [13,25-28].

In this dissertation, we are interested in the light emission and absorption properties of carbon nanotube arrays for applications regarding thermal radiation heat transfer. The radiative properties of vertically aligned carbon nanotube (VACNT) arrays was first noticed after performing ellipsometry measurements, which looked similar to antireflecting glassy carbon films [29]. The antireflective nature of VACNT is due to the sparse packing density of CNT filaments, and the near-unity refractive index to match air

or vacuum incidence media [30,31]. Near-blackbody radiative properties such as ultralow reflectance and near-unity absorptance were observed in broad wavelengths regions, from the visible to mid-infrared [31-33]. The radiative properties of VACNT coatings have been recognized in many applications such as spacecraft radiometers and bolometers [34,35], pyroelectric radiation detectors [36-38], and solar cell collectors [39,40].

As thin films, CNT arrays have demonstrated wavelength-selective transparency that suggests applications in light filtering and waveguiding [41-43]. Surveys of randomly aligned single- or double-walled CNTs have obtained high reflectance in the far-infrared wavelength region [44-46]. Theoretical studies have reasoned that the radiative properties are due to the electronic interband transitions and the plasmonic resonances that depend on the chiral orientation of neighboring single-walled CNT filaments [47,48]. The composition of the CNT filaments, being either single-walled or multi-walled, is a crucial factor in determining the wavelength-selective radiative properties. Spectroscopic measurements in the infrared have shown high absorptance of multi-walled VACNT arrays [49-51], but leaves radiative properties in broader wavelength regions to be desired. In this dissertation, the spectral and angular radiative properties of VACNT arrays are theoretically investigated from the near- to far-infrared wavelengths. The optical constants of VACNT arrays are modeled using a coordinate transformation of the dielectric function of graphite, which is extracted from data available in wavelengths from 1 um to 1000 um.

To sample fresh surfaces of highly-ordered pyrolytic graphite, by practice scientists will remove thin carbon flakes using adhesive tape. On a whim, a group led by Andre Geim at the University of Manchester in the U.K. determined the electronic

properties of this byproduct, which resulted in a Nobel Prize in Physics in 2010 for Geim and his assistant Kostya Novoselov [52]. Called graphene, carbon sheets of single atom thickness hold a unique state of quantum superconductivity. As a consequence of the sp^2 type orbital structure of graphene, free electrons existing in the $\pi - \pi$ bond plane can be mobilized with linear variance under potential biasing [17,52]. Biasing methods such as voltage gating or chemical doping have initiated the development of atomic-scale transistors [53], molecular sensors [54], and thin touch-screen displays [55]. This new class of tunable semi-metal that is uniquely 2-dimensional has enabled remarkable technologies in optical cloaking of nanomaterials [56], transparent plasmonic metasurfaces [57,58], ultrafast photodetectors [59], and numerous other applications in terahertz wave physics [60].

The absorption spectrum of graphene is characterized by a transitioning energy band in the terahertz frequency regime [61,62]. The threshold between the regime obeying free electron absorption (intraband) to one of fixed universal conductivity (interband) can be tuned by modulating the chemical potential or Fermi level [63,64]. This specific behavior allows the design of photonic switches. Examples of nano-patterned photonic devices include graphene nanodisk and nanoribbon arrays [57,65], graphene-enhanced resonance gratings [66], and graphene-dielectric multilayers [67-69]. The latter option can be easily fabricated, since lattice-matching dielectrics can be deposited below and above single-layer graphene without interfering with the individual material properties [70-72]. While the graphene-dielectric multilayers are shown to tailor emission and transmission bands in the infrared [67,73,74], their qualities in thin film infrared optics have yet to be investigated.

1.2 Hyperbolic Metamaterials

Since the findings of Maxwell's equations and Mie's scattering theory of nanoparticles, theorists have wondered: Can there be artificial materials that exhibit negative refractive index? In 2000, John Pendry from the U.K. specified a nanometers-thin medium with negative dielectric permittivity and magnetic permeability [75]. In this manner, without the need for traditionally shaped lenses, light focusing of features below the diffraction limit can be achieved with thin flat films, called superlensing. Hyperbolic metamaterials (HMMs) are unconventionally designed and structured media that demonstrate negative refraction of electromagnetic waves [76-78]. Examples of HMMs include conductive nano-slabs [79], metallic nanowire arrays [80,81], and metal-dielectric multilayers [82-84]. Potential applications of metamaterials are not limited to just imaging: Others are optical cloaking [77,85], coherent radiative emission [86,87], and effective design of TPV components [88,89].

It is easier to construct nonmagnetic HMMs of single negative electrical permittivity, as the free electron motion is confined in one spatial direction [76]. In this case, the principal components of the dielectric tensor are opposite in sign, called single-negative hyperbolic. This anisotropy can be achieved through growth and patterning of common isotropic materials [81,83,87]. Ways to tilt the optical axis of the medium can introduce media of tunable optical dispersions [68,90]. Simple computational methods, which will be elaborated in the next section, have modeled the homogeneous and anisotropic dielectric function of various hyperbolic medium configurations [3,91-94]. An example of a naturally occurring HMM is graphite. Due to the bandgap-separated conduction regimes similar to that of graphene, graphite is shown to demonstrate

negative refraction in the UV and infrared wavelengths [95]. Since multi-walled CNT arrays are essentially long rolls of graphite placed on one end [91,96], hyperbolic characteristics may emerge.

The advantages of HMMs do not end in just propagating electromagnetic waves for far-field thermal radiation. For evanescent waves characterized by a complex wavevector space, photon tunneling between gaps and resonant coupling of surface plasmon polaritons (SPPs) exist to enhance energy transfer in near-field nanometer distances. Applications where these facets are relied upon include atomic probe microscopy [97-99], magneto-resistive data storage [100,101], and emitter-receiver interfaces in TPV cells [12,102]. Conventional semiconductor substrates in the near field have demonstrated amplification of photonic density of states [103,104], and enhancement of heat flux between heated emitter and receiver substrates [102,105,106].

It has been shown that hyperbolic media such as silicon nanowires and metal-dielectric multilayers can support extended photon tunneling modes, where near-unity radiative energy transmission across a vacuum gap is possible for wavevectors possessing large imaginary terms [107]. CNT arrays may be an analog to these known hyperbolic substrates. Furthermore, thin metal or semiconducting layers placed in between emitter/receiver substrates and the nanometer-size vacuum gap were found to excite SPP resonance coupling [108,109]. Graphene may be an ideal candidate for covering hyperbolic substrates, so naturally a hybrid graphene-CNT array heterostructure is proposed to enable tunable heat flux enhancement in near-field radiation heat transfer.

1.3 Objectives and Outline

The objective of this dissertation is to: Understand the thermal radiation properties of CNT arrays and graphene, in order to design thin films or photonic devices that demonstrate characteristics of HMMs in both far-field and near-field heat transfer. The electronic structure and data surveys of graphite are studied to derive the optical properties of CNT arrays. Effective medium theory (EMT) is used to determine the homogeneous medium properties of CNT arrays and multilayers. Case studies of various multilayer compositions are investigated to find limitations of EMT. The conductivity of graphene is modeled, and the radiative coefficients for both far- and near-field are given for interfaces containing 2D conductive sheets. Metrics are developed to ascertain the underlying mechanisms of near-field plasmon resonance and tunneling, which enhance heat flux enhancement over blackbody. The works presented in this thesis can potentially impact the advancement of thermal radiative converters, coatings, and interfaces for nano-electronic devices.

The Chapters in this dissertation are organized as followed: Chapter 2 is the theoretical background needed for understanding the subsequent chapters. Topics covered in this chapter include spectral dielectric functions, EMT, hyperbolic dispersion relations, layered medium optics, Poynting vectors, and fluctuation dissipation theory for near-field thermal radiation. Chapter 3 shows the results of the thermal radiative properties of VACNT, as well as tilt-aligned carbon nanotube arrays (TACNT). Conventional properties include specular reflectance, transmittance, and absorptance in either semi-infinite media or thin films. Specialized properties are radiation penetration depth, energy streamlines, and refraction and polarization angles. Chapter 4 involves the study of various metal-dielectric multilayers and their hyperbolic nature. This portion introduces

the radiative properties of graphene in multilayers, and the impact graphene has on tuning positive or negative angle of refraction. Various metal- or semiconductor-dielectric multilayers are investigated to better understand the use and limitation of effective medium theory in hyperbolic dispersion regimes. Chapter 5 presents graphite, VACNT, and graphene for near-field thermal radiation. The fundamental mechanisms of near-field thermal radiation are elucidated, and the advantages of using hyperbolic materials as thermally emitting or absorbing bodies are made clear. A hybrid structure consisting of both VACNT and graphene is devised in this chapter to further enhance near-field heat transport. The graphene-dielectric multilayer from the previous chapter is revisited in the near-field scheme. Chapter 6 concludes the dissertation, and discusses the outlook for research in thermal radiation of nanomaterials.

CHAPTER 2

THEORETICAL BACKGROUND

This chapter covers the theory and methods needed to determine the radiative properties of carbon nanomaterial media. Maxwell's equations relevant in this study are revisited, and the relative dielectric permittivity is defined. The photon absorption processes in graphite are discussed in the context of its spectral dielectric function. Similarly, the conduction models of graphene are laid out, and the 2D geometrical assumptions are clarified. Section 2.2 introduces the effective medium theory for various metamaterial configurations. Whether the medium reveals hyperbolic dispersion is qualified, and two types of single-negative hyperbolic dispersion are characterized. Section 2.3 presents the radiative properties and coefficients, calculated from the culmination of the previous two sections. A subsection details the energy flux pathways or energy streamlines by tracing the local Poynting vectors. Lastly, Section 2.4 provides fundamental theory of the fluctuational electrodynamics, and the coefficients needed to determine the near-field heat flux. In multilayered emitter and re ceiver substrates, the penetration depth is defined to provide qualification of semi-infinite substrates.

2.1 Dielectric Function of Materials

The Maxwell's equations describe the propagation of electromagnetic waves in media governed by the electric permittivity and magnetic permeability [3]. Nonmagnetic media have permeability matching that in vacuum (μ_0), which satisfy the category of materials considered in this dissertation. Materials that are called general dielectrics are isotropic, non-dissipative (lossless), homogeneous, and linear (independent of position,

time, and electromagnetic field). However, the first two qualities are not always the case for real and pure materials. The dielectric function (ε), defined as the permittivity in the medium divided by the vacuum permittivity (ε_0), may be anisotropic and expressed in a dyadic tensor (in bold). The electric and magnetic field vectors are therefore related by,

$$-i\omega\varepsilon_0\boldsymbol{\varepsilon}E = \nabla \times H \tag{2.1}$$

where ω is the electromagnetic wave angular frequency. The presence of a dyadic tensor affects the orthogonal transverse electric (TE) and transverse magnetic (TM) electromagnetic waves differently. In the standard Cartesian coordinates, TE contains component set (E_y, H_x, H_z), and TM has (E_x, E_z, H_y).

The dielectric function can be spectrally dependent, meaning it varies with the wavelength (λ) or angular frequency. For example, the radiative reflectance of aluminum shifts from near-zero to near-unity around $\lambda = 100$ nm [3,110]. In this particular example, the shift is due to the sudden increase in the dielectric function's imaginary term. This imaginary term, or loss, accounts for the conductivity of bound electrons or lattice vibrations in dielectrics and free electrons in metals. The spectral dielectric function is given by,

$$\varepsilon(\lambda) = \varepsilon'(\lambda) + i\varepsilon''(\lambda) \tag{2.2}$$

where the single prime ($'$) and double prime ($''$) correspond to the real and imaginary parts, respectively. In conductive metals and metamaterials, ε' can be negative as will be elaborated in further sections.

The dielectric function is related to the complex refractive index, given by,

$$\varepsilon = (n + i\kappa)^2 \tag{2.3}$$

where n is the refractive index and κ is the extinction coefficient. These terms are called the optical constants, which is somewhat a misnomer, since they are also wavelength or frequency dependent. Furthermore, the function pairs (real and imaginary parts) of both the dielectric function and the optical constants are dependent functions of each other. This obeys the principle of causality, which states that effect cannot precede the cause [3]. The analytic functions that impose restrictions of the frequency-dependent function pairs, called the Kramers-Kronig relations, are given by [3,111],

$$\varepsilon'(\omega) = 1 + \frac{2}{\pi}\left[\int_0^{\omega^-} d\omega' \frac{\omega'\varepsilon''(\omega')}{\omega'^2 - \omega^2} + \int_{\omega^+}^{\infty} d\omega' \frac{\omega'\varepsilon''(\omega')}{\omega'^2 - \omega^2}\right] \tag{2.4a}$$

$$n(\omega) = 1 + \frac{2}{\pi}\left[\int_0^{\omega^-} d\omega' \frac{\omega'\kappa(\omega')}{\omega'^2 - \omega^2} + \int_{\omega^+}^{\infty} d\omega' \frac{\omega'\kappa(\omega')}{\omega'^2 - \omega^2}\right] \tag{2.4b}$$

where ω' is the dummy integrating variable over frequency. The equations presented above are simplified from Cauchy's residue theorem for complex integration. The aforementioned definitions and functions are applied to graphite in the following subsection.

2.1.1 Dielectric Function of Graphite

Highly ordered pyrolytic graphite, or just graphite for short, is a semimetal and is characterized by its layered structure containing sheets of single atom-thick carbon. The in-plane carbon atoms each having three carbon atom neighbors are held together by strong covalent bonds. The result is an sp^2 orbital structure that dangles a single electron orbital (π orbital) perpendicular to the in-plane carbon atoms [112]. This gives weak out-of-plane (z-axis) electrical conductivity and strong in-plane (x-y plane) conductivity. Thus, graphite is an optically anisotropic medium, where the optical axis ($\hat{\mathbf{c}}$) is parallel to

11

the z-axis. The dielectric permittivity is characterized by a diagonal tensor, in which the in-plane terms ε_{xx} and ε_{yy} are equal. The in-plane dielectric function is denoted by $\varepsilon_\perp$ (perpendicular to optical axis), and the out-of-plane by $\varepsilon_\parallel$ (parallel to optical axis). Electromagnetic waves with in-plane electric field components are called ordinary, and with electric fields interacting along the z-axis are called extraordinary. Figure 2.1 plots the anisotropic optical constants in the (a) ordinary and (b) extraordinary polarizations.
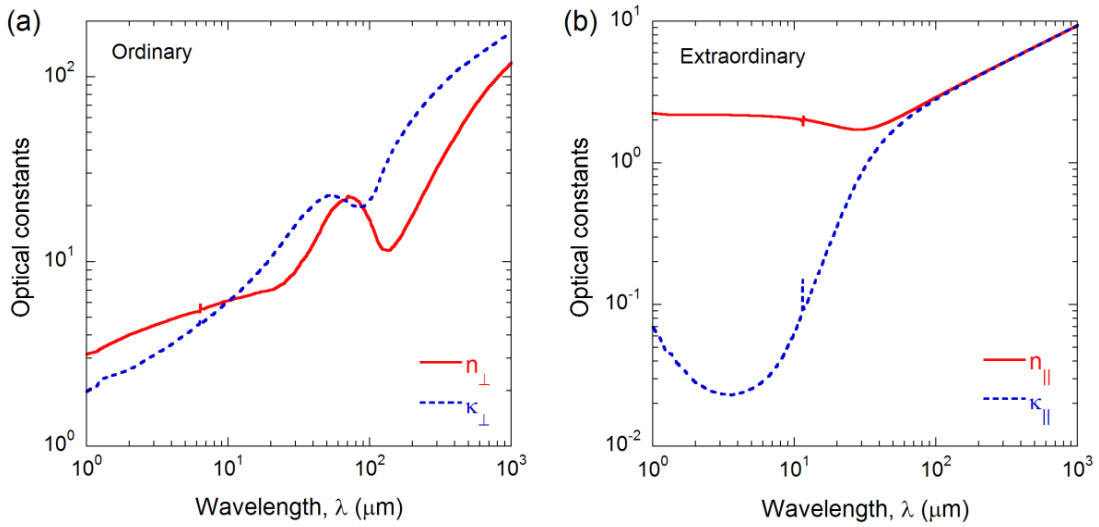
Figure 2.1 Optical constants (n and κ) of graphite: (a) Electric field perpendicular to the optical axis (ordinary), and (b) electric field parallel to the optical axis (extraordinary).

The trends in Fig. 2.1 are explained in the following: The far-infrared absorption for ordinary waves is due to the interband transition and free electrons described by the Drude model for metals [112,113]. At the interband transition, an electron is excited from the valence band to the conduction band by absorbing a photon of energy greater than the bandgap energy. In contrast, free electron absorption or an intraband process is governed by oscillations and damping of electrons perturbed by low-energy photons [3]. The interband absorption in graphite can be attributed to the interlayer interactions that result

in a bandgap energy of about 0.01 to 0.02 eV (centered around 93 μm) at the H point of the hexagonal Brillouin zone [112,114]. For extraordinary waves, only weak free-electron absorption exists, which explains the gradual upward slope at wavelengths longer than 20 μm [3,115]. The narrow and sharp peaks are due to lattice vibrations in the mid-infrared for both ordinary and extraordinary waves [116]. The constant $n_{\parallel} \approx 2$ and the small extinction coefficients suggest graphite behaves as an absorbing dielectric in the near-infrared wavelength region.

Spectroscopic measurements of graphite were challenging, especially for surfaces that were cut perpendicular to the in-plane carbon sheets [117]. The Kramers-Kronig relations have commonly been used to obtain the dielectric function if the reflectance is obtained in a large spectrum and reasonably extrapolated to zero and infinite frequencies, as demonstrated in Eq. (2.4). However, the lack of broadband spectroscopic instruments at the time meant limited tabulated optical constants [113,117,118]. In 1984, Draine and Lee of Princeton University performed a comprehensive analysis of the previous compositions to provide broadband spectra from the UV to far-infrared [119]. The far-infrared optical constants up to 1240 μm were fitted to Drude model parameters [113]. The lattice vibrations at around 6.3 μm for ordinary waves and 11.5 μm for extraordinary waves were matched with Lorentz model parameters [116]. The dielectric functions excluding the contributions from Lorentz oscillations and Drude absorption were extracted from Draine and Lee using data grabbing software (PlotDigitizer). The Lorentz and Drude models were superimposed after extraction. Figure A.1 in Appendix A verifies that the Kramers-Kronig relations are roughly satisfied after extracting the dielectric function within the frequency range that was made available.

2.1.2 Dielectric Function of Graphene

The unit that forms graphite, graphene, has similar optical properties. However, because graphene is a 2D material, determination of its dielectric function cannot be done in traditional ways. Graphene modeled in this dissertation is assumed to be isolated in single-layer form and free of defects [120,121]. Graphene does not bond or electrically interact with substrates [122]. To model the sheet conductivity (σ) of graphene in the infrared, both intraband and interband contributions need to be considered. The sheet conductivity is a function of the electromagnetic wave frequency, chemical potential or Fermi level (μ), relaxation time (τ), and temperature (T). In the frequency range corresponding to mid-infrared wavelength, the dominant contribution from the intraband conductivity is given by,

$$\sigma_{\text{Intra}}(\mu,\omega,T) = \frac{i}{\omega+i/\tau}\frac{q^2}{\pi\hbar^2}2k_BT\ln\left[2\cosh\left(\frac{\mu}{2k_BT}\right)\right] \qquad (2.5)$$

which behaves similar to the Drude model for free electrons [63,64]. In the limit whereby $|\mu| \gg k_BT$, the latter term $2k_BT\ln\left[2\cosh\left(\mu/2k_BT\right)\right]$ can be approximated as μ. The DC relaxation time due to carrier-impurity scattering typically ranges from 10^{-13} s to 10^{-12} s, and increases with higher chemical potential [64,123-126]. For Eq. (2.5) to be valid, the scattering rate (τ^{-1}) must be smaller than ω [63,127]. This criterion is satisfied since the majority of thermal radiation near room temperature falls in the mid-infrared region.

The interband conductivity for direct bandgap transitions of electrons at non-zero temperatures is modeled using,

$$\sigma_{\text{Inter}}(\mu,\omega,T) = \frac{q^2}{4\hbar}\left[G\left(\frac{\hbar\omega}{2}\right) + i\frac{4\hbar\omega}{\pi}\int_{\eta=0}^{\infty}\frac{G(\eta)-G(\hbar\omega/2)}{(\hbar\omega)^2-4\eta^2}d\eta\right] \qquad (2.6)$$

where $G(\eta) = \sinh(\eta/k_{\text{B}}T)/[\cosh(\eta/k_{\text{B}}T) + \cosh(\mu/k_{\text{B}}T)]$ is the difference function from the Fermi-Dirac distribution [63,127]. Numerically, the integrating variable η is taken from 0 to 10μ, which provides a sufficient upper bound at near room temperatures. Toward high frequencies, the interband conductivity approaches the universal 2D conductivity for undoped graphene, such that $\sigma_0 \equiv \sigma(\omega\to\infty) = q^2/4\hbar$ [61,62]. The total sheet conductivity of graphene is the sum of both intraband and interband contributions, given by $\sigma = \sigma_{\text{Intra}} + \sigma_{\text{Inter}}$. Figure B.1 in Appendix B demonstrates similarities of graphene conductivity extracted from Ref. [61] with that obtained from Eqs. (5) and (6). The latter portrays the conductivity having distinct intraband- and interband-dominant frequency regimes under ideal conditions.

Graphene can be expressed with a dielectric function with a finite medium thickness, and is expressed as,

$$\varepsilon_{\text{g}}(\mu,\omega,T) = \varepsilon_{\text{h}} + \frac{i\sigma(\mu,\omega,T)}{\Delta_{\text{g}}\omega\varepsilon_0} \qquad (2.7)$$

where the thickness of graphene obtained from the interlayer distance resolved from graphite is $\Delta_{\text{g}} = 0.335$ nm [67,128,129]. The dielectric function of the adjacent host medium is ε_{h}. The expression in Eq. (2.7) only applies to the dielectric function of graphene in-plane, and the out-of-plane dielectric function is identical to the host's. The magnitude of conduction perpendicular to the hexagonal axis (out-of-plane) is many times smaller and therefore negligible [130]. Results shown in the following chapters

verify that graphene can be treated as either a conductive sheet or anisotropic medium, with very little difference.

2.2 Hyperbolic Metamaterials

Carbon nanotubes are elementally similar to graphite, but certainly have different geometries. CNTs are typically formed by thermal catalytic decomposition of hydrocarbons at metal (i.e., iron) catalyst particle sites during a plasma-enhanced chemical vapor deposition process [131-133]. Multi-walled CNTs are characterized to have graphitic layers forming in parallel to the growth direction [96]. In other words, one can visualize them as many graphene sheets rolled together into tubes and positioned on a flat horizontal substrate at one end of the tube. A bandgap or pseudogap similar to that of graphite was observed for CNTs in the far-infrared, which have been attributed to the curvature and intertube interactions [46,134,135]. The optical properties of VACNT arrays can be modeled using the dielectric functions of graphite.

2.2.1 Effective Medium Theory

Figure 2.2 shows a representative array of VACNT on a substrate. The defining dimensions of the VACNT array are the diameter (Δ_{CNT}) and unit cell width (a), as highlighted in the inset of Fig. 2.2(a). The VACNT medium or film of thickness (d) is naturally an inhomogeneous medium since it is composed of periodic CNTs and voids (either air or vacuum). Effective medium theory (EMT) homogenizes the medium, provided that the wavelength of the incidence electromagnetic radiation is much longer than the unit cell width. Based on 10 to 30 nm diameter multi-walled CNT filaments [50,136], and 50 to 150 nm wide unit cells, wavelengths from the near-infrared

16

$(\lambda > 1\,\mu\text{m})$ can be studied. VACNT arrays can be treated as a uniaxial medium whose optical axis is parallel to the tube or along the z-axis. Based on the Maxwell-Garnett theory, the effective dielectric functions for perfectly aligned VACNT can be expressed in terms of the filling ratio (f) and the dielectric function of graphite. The ordinary and extraordinary dielectric functions are respectively given by [50,91],

$$\varepsilon_{\text{CNT,O}} = \frac{\varepsilon_{\parallel}(1+f) + \sqrt{\varepsilon_{\parallel}/\varepsilon_{\perp}}(1-f)}{\varepsilon_{\parallel}(1-f) + \sqrt{\varepsilon_{\parallel}/\varepsilon_{\perp}}(1+f)} \tag{2.8a}$$

$$\varepsilon_{\text{CNT,E}} = f\varepsilon_{\perp} + (1-f) \tag{2.8b}$$

The filling ratio defined in terms of the VACNT array dimensions is $f = \pi\Delta_{\text{CNT}}^2/(4a^2)$. Note that the ordinary component can only be physically represented along the x or y coordinates, and no component in between.

The CNT in the subscripts from Eq. (2.8) only represents the dielectric function of perfectly aligned VACNT arrays, as shown in Fig 2.2(b). Considering defects from sample fabrication such as random and local tilting and fiber entanglements, the dielectric functions are modified with a weighting constant ξ, called the alignment factor. The alignment factor for perfectly aligned VACNT arrays is $\xi = 1.0$. The misalignment is quantified with $\xi < 1$, as shown in Fig. 2.2(c). For typical CVD-grown VACNT films, ξ ranges from 0.950 to 0.995, which are obtained from fitting measured reflectance spectra and scanning electron microscope surveys of CNT filaments [50,137]. It should be noted that the component weighted model is only applied for slight misalignment, when ξ is sufficiently large. The dielectric functions of VACNT accounting for alignment factor are given by,

$$\varepsilon_O = \xi \varepsilon_{CNT,O} + (1-\xi)\varepsilon_{CNT,E} \qquad (2.9a)$$

$$\varepsilon_E = \xi \varepsilon_{CNT,E} + (1-\xi)\varepsilon_{CNT,O} \qquad (2.9b)$$

The EMT-based expression for the dielectric function of VACNT is therefore dependent on both the filling ratio and alignment factor.
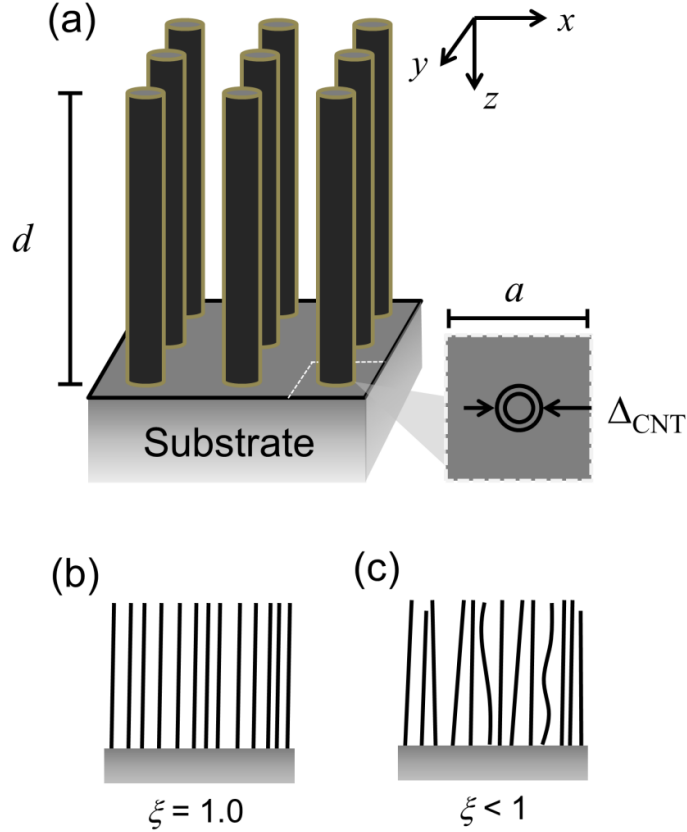
Figure 2.2 (a) Illustration of VACNT film of thickness d grown on a substrate (i.e., silicon). The inset shows a unit cell of width a containing a multi-walled CNT of diameter Δ_{CNT} in a periodic array. (b) Perfectly aligned CNTs with an alignment factor of $\xi = 1.0$. (c) Locally imperfectly aligned CNTs where $\xi < 1$. Typical VACNT coatings produced from experiment range from $\xi = 0.95$ to $\xi = 0.99$.

Other EMT formulations can also apply to similar vertical tube arrays, such as nanowires made of silicon or silver [80,138]. One of the earliest EMT formulations was on periodically structured stratified media [139]. This uniaxial crystal, often called multilayers, is often used for antireflection and selective radiation applications. Figure 2.3

illustrates the multilayers containing alternating dielectric (d) and metal (m) media. The period Λ is the sum of one of dielectric and metal layers' thicknesses. The incidence angle from vacuum is denoted as θ_i. The zeroth-order expressions of the dielectric function is applicable if $\lambda \gg \Lambda$, and are given by,

$$\varepsilon_O = f\varepsilon_{m,O} + (1-f)\varepsilon_{d,O} \tag{2.10a}$$

$$\varepsilon_E = \frac{\varepsilon_{d,E}\varepsilon_{m,E}}{f\varepsilon_{d,E} + (1-f)\varepsilon_{m,E}} \tag{2.10b}$$

where the filling ratio in this particular geometry is $f = d_m / (d_d + d_m)$. The ordinary and extraordinary dielectric functions in both the constituent dielectric and metal layers are preserved in the anisotropic dielectric function of the multilayers. In Chapter 5, the size of successive periods are changed (i.e., $\Lambda_1 < \Lambda_2 < \Lambda_3 \cdots$) while preserving the filling ratio. In this case, it is unknown how EMT accounts for Λ.
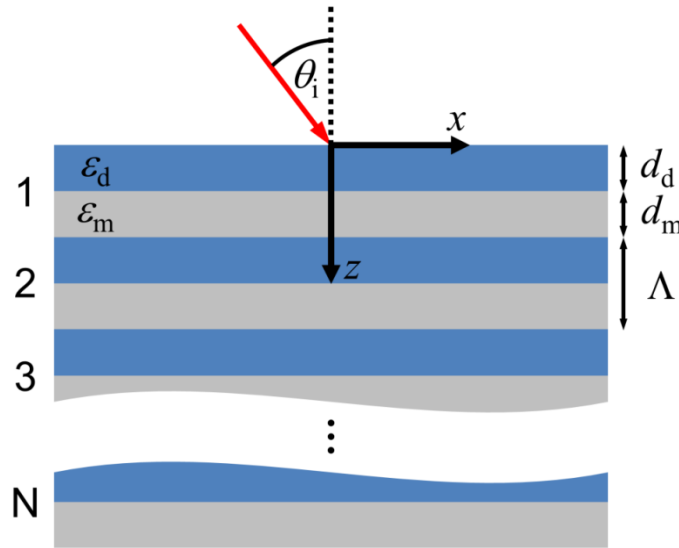
Figure 2.3 Illustration of a periodic metal-dielectric multilayer thin film with associated nomenclature. The incidence and outgoing media are vacuum.

2.2.2 Dispersion Relations

Since graphite is nonmagnetic, and is optically anisotropic, the carbon-based nanomaterials are mostly of single-negative electric permittivity hyperbolic. Graphite is hyperbolic in two regions: At wavelengths above 90 μm ($\omega < 2.1 \times 10^{13}$ rad/s), the real part of $\varepsilon_\perp$ is negative due to the intraband absorption of electrons. Another region exists between 10 μm (1.8×10^{14} rad/s) and 63 μm (3.0×10^{13} rad/s), in which the region between 63 μm and 90 μm is due to the interband transition. This attests to the high attenuation of thermal radiation in graphite in the far-infrared.

While graphite has negative permittivity in the ordinary wave direction, VACNT may have negative permittivity in the extraordinary wave direction. The two hyperbolic types are categorized as followed: Type I hyperbolic dispersion is defined by $\varepsilon'_O > 0$ and $\varepsilon'_E < 0$ [89,140,141]. Type II hyperbolic dispersion is defined by $\varepsilon'_E > 0$ and $\varepsilon'_O < 0$. In any case, if $\varepsilon' = 0$, it is called an epsilon-near-zero (ENZ) material. The contrasting effects of the two hyperbolic dispersion is explained using the dispersion relation of an anisotropic medium, which is given by,

$$\frac{k_x^2}{\varepsilon_E} + \frac{k_z^2}{\varepsilon_O} = k_0^2 \tag{2.11}$$

where the k_x and k_z are the wavevectors in the resultant homogeneous medium, and k_0 is the wavevector in free space (vacuum) [142]. The wavevectors in hyperbolic media also depends on the polarization of the incidence electromagnetic waves. For TE waves (s-polarization from the German word *senkrecht*), $k_z^S = \sqrt{k_0^2 \varepsilon_O - k_x^2}$, and for TM waves

(p-polarization from the German and English word *parallel*), $k_z^{\text{p}} = \sqrt{k_0^2 \varepsilon_{\text{O}} - k_x^2 \varepsilon_{\text{O}}/\varepsilon_{\text{E}}}$.

The k_x wavevector is preserved throughout ($k_x = k_0 \sin \theta_i$ for propagating waves).

To help illustrate the wave propagation into the resulting medium, or the lack thereof, Figure 2.4 draws two isofrequency contour plots of hyperbolic media. Fig. 2.4(a) is Type I HMM defined by $\varepsilon_{\text{O}} = 2$ and $\varepsilon_{\text{E}} = -2$. The hyperbolic shape is evident in the upward and downward facing curves shown in the normalized wavevector space. In vacuum, the wavevector (k_i) and Poynting vector (S_i), which points to the direction of energy flow, are co-linear. In the resulting hyperbolic medium, the wavevector (k_2) is refracted and remains in phase of the incidence wavevector. The resultant Poynting vector (S_2), on the other hand, is distended leftward, which signifies negative refraction of energy fronts. Theoretical prediction of sideways-turned graphite demonstrates this negative angle of refraction [95].

On the other hand, for Type II hyperbolic dispersion shown in Fig. 2.4(b), the orthogonal permittivities have switched ($\varepsilon_{\text{O}} = -2$ and $\varepsilon_{\text{E}} = 2$). While the incidence vectors remain largely the same, in order to obtain a Poynting vector in the Type II hyperbolic medium, the resultant wavevector must be evanescent ($k_x > k_0$). Unless the incidence wave is evanescent and greater than the critical wavevector $\left(k_{\text{cr}} = k_0 \sqrt{\varepsilon_{\text{E}}}\right)$, Type II HMMs are highly reflecting and do not demonstrate negative refraction of Poynting vectors [141,142]. For uniaxial metamaterials, no negative refraction can occur for TE waves since the electric field is perpendicular to the plane of incidence. The isofrequency contour is circular in the wavevector space, and follows the dispersion

21

relation of $k_x^2 + k_z^2 = \varepsilon_O k_0^2$. This primer for the characteristics of two HMM types will be applied and reanalyzed for VACNT, tilted CNT arrays, and multilayers in the remaining Chapters.
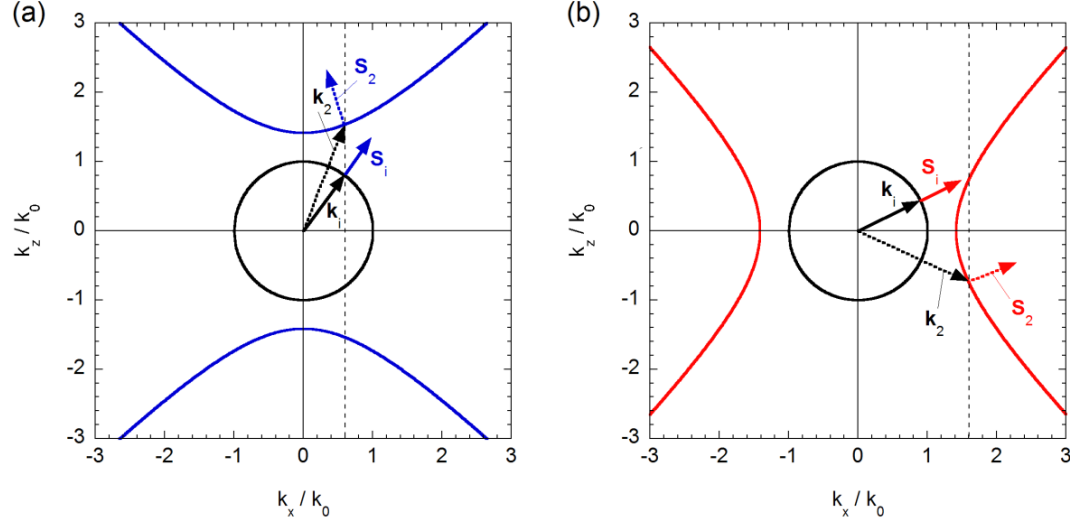
Figure 2.4   Diagrams of hyperbolic dispersion for: (a) Type I defined by $\varepsilon_O > 0$ and $\varepsilon_E < 0$, and (b) Type II by $\varepsilon_O < 0$ and $\varepsilon_E > 0$. The black circle represents the dispersion of incidence light with wavevector k_i and Poynting vector S_i. The resultant wavevector and Poynting vector in the hyperbolic medium are represented by k_2 and S_2, respectively.

2.3 Thin-Film Optics and Energy Streamlines

The radiative properties of semi-infinite media can be formulated using the Fresnel coefficients expressed in terms of the surface admittance (TE waves) or impedance (TM waves) [3,93]. The Fresnel coefficients are derived from the ratio of reflected or transmitted electric (TE wave) and magnetic (TM wave) fields to the incidence fields. In wavevector notation, the TE wave Fresnel reflection and transmission coefficients from medium of index j into medium $j+1$ are expressed as,

$$r_{j,j+1}^{\text{s}} = \frac{k_{z,j}^{\text{s}} - k_{z,j+1}^{\text{s}}}{k_{z,j}^{\text{s}} + k_{z,j+1}^{\text{s}}} \tag{2.12a}$$

$$t_{j,j+1}^{\text{s}} = \frac{2k_{z,j}^{\text{s}}}{k_{z,j}^{\text{s}} + k_{z,j+1}^{\text{s}}} \tag{2.12b}$$

which assumes that the media are nonmagnetic. Even for uniaxial and anisotropic permittivity materials, the TE wave radiative properties are isotropic. For TM waves, the reflection coefficient is derived from the differences in the impedances of the neighboring media, and is given by,

$$r_{j,j+1}^{\text{p}} = \frac{k_{z,j}^{\text{p}}\varepsilon_{\text{O},j+1} - k_{z,j+1}^{\text{p}}\varepsilon_{\text{O},j}}{k_{z,j}^{\text{p}}\varepsilon_{\text{O},j+1} + k_{z,j+1}^{\text{p}}\varepsilon_{\text{O},j}} \tag{2.13}$$

The Fresnel transmission coefficient is more complex due to possible phase reversal of magnetic fields as waves travel from optically dense to optically thin media. This is especially true for HMMs where refracted waves become inhomogeneous and the TE and TM wave Poynting vectors split into different directions [3,143]. The transmission coefficient for TM waves is expressed as,

$$t_{j,j+1}^{\text{p}} = \frac{\sqrt{\left(k_{z,j+1}^{\text{p}}\big/\varepsilon_{\text{O},j+1}\right)^2 + \left(k_{x,j+1}\big/\varepsilon_{\text{E},j+1}\right)^2}}{\sqrt{\left(k_{z,j}^{\text{p}}\big/\varepsilon_{\text{O},j}\right)^2 + \left(k_{x,j}\big/\varepsilon_{\text{E},j}\right)^2}} \frac{2k_{z,j}^{\text{p}}\varepsilon_{\text{O},j+1}}{k_{z,j}^{\text{p}}\varepsilon_{\text{O},j+1} + k_{z,j+1}^{\text{p}}\varepsilon_{\text{O},j}} \tag{2.14}$$

The radiative properties defined by the reflectance and transmittance are the ratios of power flow or energy flux in the direction normal to the interface. For both TE and TM waves, the reflectance is the square of the magnitudes of the electric and magnetic fields, respectively. The reflectance in terms of the Fresnel reflection coefficient of either polarization is,

$$R = \left| r_{j,j+1} \right|^2 \qquad (2.15)$$

assuming that the resultant medium is semi-infinite. The reflectance defined here is directionally specular (denoted by a prime or implied), meaning that the reflected angle is identical to the incidence angle. This holds that the surface is perceived as smooth, in which for most cases is true for incidence infrared wavelength radiation [3,51]. The TM wave transmittance is given by,

$$T^p = \left| t^p_{j,j+1} \right|^2 \frac{\mathrm{Re}\left(Z^+_{j+1} \right)}{\mathrm{Re}\left(Z^+_j \right)} \qquad (2.16)$$

where $Z^{\pm}_j = \left(k_{x,j}\varepsilon_{j,xz} + k^{\pm}_{j,z}\varepsilon_{j,zz} \right) \big/ \left(\omega\varepsilon_0\varepsilon_{j,O}\varepsilon_{j,E} \right)$ is the surface impedance, needed in the formula to account for dissipation and wave inhomogeneity in the resultant medium. In semi-infinite media, the reflectance and transmittance are related by $R+T=1$.

For thin films or stratified media, the radiative absorptance or fraction of energy dissipated in a homogeneous medium is defined by $A=1-R-T$. To model the multiple internal reflections, ray tracing method can be used [3,92,93]. However, this method is only suitable for incoherent waves where the interference from internally reflected waves can be neglected. The incoherent limit is settled when the wavelength is smaller than the thickness of the layers. In the case of micron-scale coatings and nanometers-thick deposited layers, the phase change or wave coherence must be accounted for. The following subsection introduces a method that includes the effects of wave interference for layers of various thicknesses or material compositions.

24

2.3.1 Transfer Matrix Method and Poynting Vector

The transfer matrix method (TMM) has been used for calculation of radiation properties of thin-film multilayers and left-handed photonic crystals [86,92,144,145]. The TMM solves for the electric or magnetic field amplitudes in the wave equation. The equation for a TE-polarized monochromatic plane wave in medium j is given by,

$$E_{y,j}(x,z) = \left[A_j e^{ik_{z,j}z} + B_j e^{-ik_{z,j}z} \right] e^{i(k_x x - \omega t)} \tag{2.17}$$

where A_j and B_j are the forward- and backward-propagating electric field amplitudes, respectively. For TM waves, which is of main interest, the magnetic field perpendicular to the plane of incidence (x-z plane) is given by,

$$H_{y,j}(x,z) = \left[A_j e^{ik_{z,j}^+ z} + B_j e^{ik_{z,j}^- z} \right] e^{i(k_x x - \omega t)} \tag{2.18}$$

where the forward (+) and backward (-) TM-polarized wavevectors are defined by the dielectric tensor components,

$$k_z^\pm = \frac{-k_x \varepsilon_{xz} \pm \sqrt{\left(\varepsilon_{xx}\varepsilon_{zz} - \varepsilon_{xz}^2 \right)\left(k_0^2 \varepsilon_{zz} - k_x^2 \right)}}{\varepsilon_{zz}} \tag{2.19}$$

In order to solve for the electric and magnetic field vectors, Eq. (2.1) is implemented along with the field amplitudes determined by the TMM. The TMM assigns a pair of 2×2 transmission matrices and a diagonal propagation matrix for every layer. The transmission matrices are defined in terms of the Fresnel reflection and transmission coefficients, given by,

$$\mathbf{D}_j^{-1}\mathbf{D}_{j+1} = \frac{1}{t_{j,j+1}} \begin{pmatrix} 1 & r_{j,j+1} \\ r_{j,j+1} & 1 \end{pmatrix} \tag{2.20}$$

The propagation matrix is given by an exponential decay term dependent upon the thickness of the layer (d_j),

$$\mathbf{P}_j = \begin{pmatrix} e^{-ik_{z,j}^+ d_j} & 0 \\ 0 & e^{-ik_{z,j}^- d_j} \end{pmatrix} \tag{2.21}$$

The field amplitudes can be solved in the following system of equations,

$$\begin{bmatrix} A_j \\ B_j \end{bmatrix} = \mathbf{P}_j \mathbf{D}_j^{-1} \mathbf{D}_{j+1} \begin{bmatrix} A_{j+1} \\ B_{j+1} \end{bmatrix} \tag{2.22}$$

The field amplitudes in any layer can be solved by the consecutive products of the PDD matrix set from the semi-infinite incidence layer (medium 1) to the semi-infinite outgoing layer (medium N+1) corresponding to Fig. 2.3. The boundary condition of radiation incidence from medium 1 is $A_1 = 1$, and the lack of backward reflection in the outgoing medium is described by $B_{N+1} = 0$. The exact solutions or Airy's formulae for field amplitudes in 3 layers, the center containing a thin film, can be found in Refs. [92] and [146].

The known electric fields and magnetic fields in every layer of stratified media can be used to solve for the Poynting vector. The time-averaged Poynting vector components are determined by,

$$S_x = 0.5 \mathrm{Re}\left(E_z \times H_y^* \right) \tag{2.23a}$$

$$S_z = 0.5 \mathrm{Re}\left(E_x \times H_y^* \right) \tag{2.23b}$$

where the * signifies the Hermitian complex transform of the function. The Poynting vector is only a function of z, since the x and temporal term are cancelled. A simple spatial extrapolation method of the Poynting vector maps the energy streamlines.

2.3.1 Tilted Uniaxial Medium Transform

The traditional uniaxial medium is characterized by a diagonal permittivity tensor. This medium can be tilted within the plane of incidence without causing TE and TM wave coupling in the Fresnel reflection and transmission coefficients [3,94]. The tilting angle is characterized by β in Figure 2.5. In this thin film of thickness d_2, the optical axis is no longer aligned with the fixed z-axis. Here, the permittivity tensor contains off-diagonal components, as evidenced by ε_{xz} and ε_{zx} in,

$$\overline{\overline{\varepsilon}} \equiv \begin{pmatrix} \varepsilon_{xx} & 0 & \varepsilon_{xz} \\ 0 & \varepsilon_{yy} & 0 \\ \varepsilon_{zx} & 0 & \varepsilon_{zz} \end{pmatrix} = \begin{pmatrix} \varepsilon_O \cos^2 \beta + \varepsilon_E \sin^2 \beta & 0 & (\varepsilon_E - \varepsilon_O) \sin \beta \cos \beta \\ 0 & \varepsilon_O & 0 \\ (\varepsilon_E - \varepsilon_O) \sin \beta \cos \beta & 0 & \varepsilon_O \sin^2 \beta + \varepsilon_E \cos^2 \beta \end{pmatrix} \quad (2.24)$$

The effect of tilting is evident in the wavevector defined in Eq. (2.19). The wavevector in the forward direction is distinct from the wavevector in the backward direction.
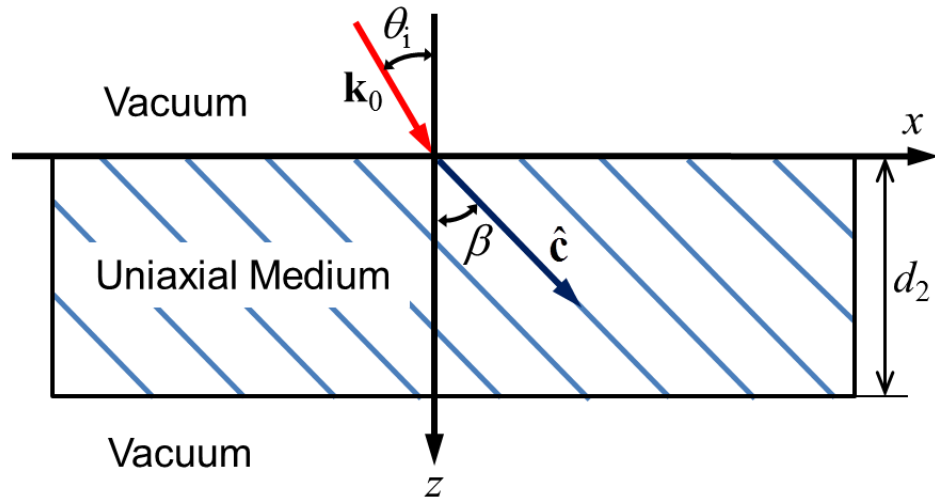
Figure 2.5 Illustration of a uniaxial slab of thickness d_2 made of TACNT array having a tilting angle β, for a plane wave incidence from the top vacuum medium. The uniaxial CNT array is modeled as an effective dielectric tensor whose optical axis $\hat{\mathbf{c}}$ is along the nanotube filament.

Furthermore, the hyperbolic dispersion relation from Eq. (2.11) is altered. Here, the wavevector components are crossed with trigonometric components of the tilting angle, as shown in

$$\frac{(k_z \cos \beta + k_x \sin \beta)^2}{\varepsilon_O} + \frac{(k_z \sin \beta - k_x \cos \beta)^2}{\varepsilon_E} = k_0^2 \qquad (2.25)$$

The consequences of in-plane tilting on VACNT arrays are explored in the next Chapter.

2.4 Near-Field Thermal Radiation

According to Snell's law, light from an optically dense medium to an optically thin medium cannot be transmitted past a certain incidence angle. Past this incidence angle, called the critical angle, total internal reflection occurs. However, not precisely everything is obstructed. No energy or propagating waves pass through, but electromagnetic fields exist near the surface of the optically thin medium. These surface waves can exchange energy with optically dense media at any instant in time. When another optically dense medium sandwiches the optically thin medium into a very thin (nanometers) layer, photon tunneling can occur even at incidence angles greater than the critical angle. Figure 2.6 illustrates two optically dense semi-infinite substrates surrounding a vacuum gap that is comparable or smaller than the wavelength of incidence radiation. The two interfaces are infinite in the radial (x) direction. For a TPV-like application, the emitter temperature is T_1 and receiver temperature is T_2.

2.4.1 Fluctuational Electrodynamics

In the far field, the net radiative heat flux between two semi-infinite and opaque flat surfaces is governed by the Stefan-Boltzmann law. More precisely, the heat flux is

obtained from the integration of near-infinite wavelengths and hemispherical emissivity in both polarizations. Called the heat flux between blackbodies, this does not include the effects of wave interference and photon tunneling.
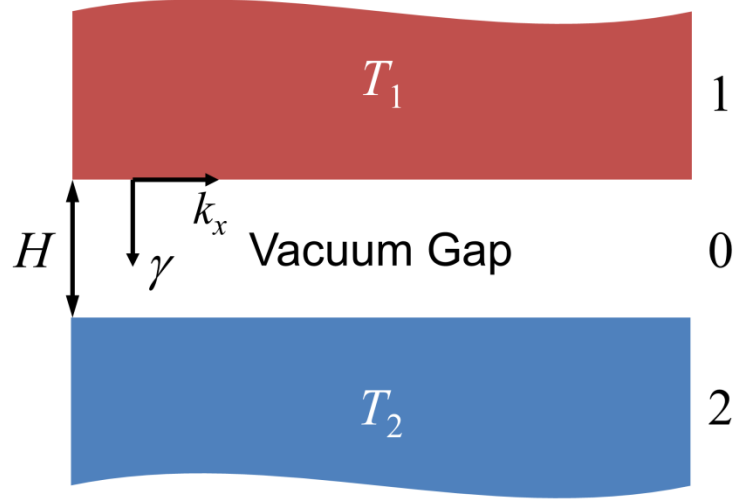
Figure 2.6 Representation of a near-field device composed of a semi-infinite emitter medium at temperature T_1, a vacuum gap size of H, and a semi-infinite receiver medium at temperature T_2. The wavevector components are outlined.

In the near field, obtaining the heat flux is complicated by the random thermal fluctuations in a body. Assuming a nonmagnetic body, there exist fluctuating electric currents that cause distributions of electromagnetic fields in space and time [147]. In any point in space shown in Fig. 2.6, its electromagnetic fields are a superposition of contributions from point sources in the emitting body (medium 1). The point sources are represented by a Fourier transformed electric current density $\mathbf{j}(\mathbf{r}, \omega)$, where $\mathbf{r}$ is the cylindrical unit spatial vector [148]. The electric and magnetic fields in the frequency domain can be expressed as a volume integration of $\mathbf{j}$ dot-product with the dyadic Green's function $\mathbf{G}(\mathbf{r}, \mathbf{r}', \omega)$,

$$\mathbf{E}(\mathbf{r},\omega) = \mathbf{i}\omega\mu_0 \int_V \mathbf{G}(\mathbf{r},\mathbf{r}',\omega) \cdot \mathbf{j}(\mathbf{r}',\omega) d\mathbf{r}' \tag{2.26a}$$

$$\mathbf{H}(\mathbf{r},\omega) = \int_V \nabla \times \mathbf{G}(\mathbf{r},\mathbf{r}',\omega) \cdot \mathbf{j}(\mathbf{r}',\omega) d\mathbf{r}' \tag{2.26b}$$

where the primed spatial vector is located at the current source. In the geometry faced in Fig. 2.6, the Green's function is defined as,

$$\mathbf{G}(\mathbf{r},\mathbf{r}',\omega) = \int_0^\infty \frac{i}{4\pi k_{z,1}} \left(\hat{\mathbf{s}} t_{12}^{\mathrm{s}} \hat{\mathbf{s}} + \hat{\mathbf{p}}_2 t_{12}^{\mathrm{p}} \hat{\mathbf{p}}_1 \right) e^{i\left(k_{z,2}z - k_{z,1}z'\right)} e^{ik_x(r-r')} k_x dk_x \tag{2.27}$$

where unit vectors $\hat{\mathbf{s}} = \hat{\mathbf{r}} \times \hat{\mathbf{z}}$, and $\hat{\mathbf{p}}_j = \left(k_x \hat{\mathbf{z}} - k_{z,j} \hat{\mathbf{x}} \right)/k_j$ [3]. By projecting the time-averaged Poynting vector in the z-direction, evaluated using Eq. (2.26), the spectral energy flux in the direction from the emitter to the receiver is,

$$Q'_{12}(k_x,\omega,T_1) = \frac{\Theta(\omega,T_1)}{4\pi^2} \int_0^\infty \mathcal{T}_j(\omega,k_x) k_x dk_x \tag{2.28}$$

The mean energy of a Planck oscillator in thermal equilibrium is given by,

$$\Theta(\omega,T) = \frac{\hbar\omega}{e^{\hbar\omega/k_{\mathrm{B}}T} - 1} \tag{2.29}$$

and the near-field transmission coefficient (exchange function) of polarization type j (either $j = \mathrm{s}$ or $j = \mathrm{p}$) is given by [3,149],

$$\mathcal{T}_j(\omega,k_x) = \begin{cases} \dfrac{\left(1 - \left|r_{01}^j\right|^2\right)\left(1 - \left|r_{02}^j\right|^2\right)}{\left|1 - r_{01}^j r_{02}^j e^{-2i\gamma H}\right|^2}, & k_x < k_0 \\[2em] \dfrac{4\,\mathrm{Im}\left(r_{01}^j\right)\mathrm{Im}\left(r_{02}^j\right)e^{-2\,\mathrm{Im}(\gamma)H}}{\left|1 - r_{01}^j r_{02}^j e^{-2i\gamma H}\right|^2}, & k_x > k_0 \end{cases} \tag{2.30}$$

Here, the z-direction wavevector in the vacuum gap is $\gamma = \sqrt{k_0^2 - k_x^2}$. The net heat flux is taken from the integration over zero to infinite frequencies of Q'_{12} minus Q'_{21} (exchanging 1 with 2 in subscripts), which gives,

$$Q(k_x, \omega, T_1, T_2) = \frac{1}{4\pi^2} \int_0^\infty [\Theta(\omega, T_1) - \Theta(\omega, T_2)] d\omega \int_0^\infty \sum_{j=s,\,p} \mathcal{T}_j(\omega, k_x) k_x dk_x \quad (2.31)$$

This expression is applicable to both near- and far-field situations. The second term in Eq. (2.30) is expected to diminish with increasing H comparable to the order of the infrared wavelength.

2.4.2 Near-Field Poynting Vector

The exact expression of the Poynting vector can be obtained by evaluating the Green's function integrations in the electric and magnetic field equations, i.e. Eq. (2.27) into Eq. (2.26). The TM wave Poynting vector for a uniaxial medium is given by,

$$\langle S_z(z, \omega, T) \rangle = \Theta(\omega, T) \frac{k_0^2 k_x}{2\pi^3} \mathrm{Re} \left[i \int_z \begin{pmatrix} \varepsilon_O'' g_{\rho\rho}(k_x, \omega, z, z') h_{\theta\rho}^*(k_x, \omega, z, z') \\ + \varepsilon_E'' g_{\rho z}(k_x, \omega, z, z') h_{\theta z}^*(k_x, \omega, z, z') \end{pmatrix} dz' \right] \quad (2.32)$$

The Weyl representation of the electric (g) and magnetic (h) dyadic Green's function components are listed below:

$$g_{\rho\rho}(k_x, \omega, z, z') = \frac{ik_{z,n}^p}{2\gamma_m\gamma_n} \begin{pmatrix} A_n^p e^{i[k_{z,n}^p(z-z_0) - k_{z,m}^p z']} - B_n^p e^{i[-k_{z,n}^p(z-z_0) - k_{z,m}^p z']} \\ - C_n^p e^{i[k_{z,n}^p(z-z_0) + k_{z,m}^p z']} + D_n^p e^{i[-k_{z,n}^p(z-z_0) + k_{z,m}^p z']} \end{pmatrix} \quad (2.33a)$$

$$g_{\rho z}(k_x, \omega, z, z') = \frac{ik_{z,n}^p k_x}{2k_{z,m}^p \gamma_m\gamma_n} \begin{pmatrix} -A_n^p e^{i[k_{z,n}^p(z-z_0) - k_{z,m}^p z']} + B_n^p e^{i[-k_{z,n}^p(z-z_0) - k_{z,m}^p z']} \\ - C_n^p e^{i[k_{z,n}^p(z-z_0) + k_{z,m}^p z']} + D_n^p e^{i[-k_{z,n}^p(z-z_0) + k_{z,m}^p z']} \end{pmatrix} \quad (2.33b)$$

31

$$h_{\theta\rho}(k_x,\omega,z,z') = \frac{\gamma_n}{2\gamma_m}\left(\begin{array}{l} -A_n^{\mathrm{p}}e^{i[k_{z,n}^{\mathrm{p}}(z-z_0)-k_{z,m}^{\mathrm{p}}z']} - B_n^{\mathrm{p}}e^{i[-k_{z,n}^{\mathrm{p}}(z-z_0)-k_{z,m}^{\mathrm{p}}z']} \\ +C_n^{\mathrm{p}}e^{i[k_{z,n}^{\mathrm{p}}(z-z_0)+k_{z,m}^{\mathrm{p}}z']} + D_n^{\mathrm{p}}e^{i[-k_{z,n}^{\mathrm{p}}(z-z_0)+k_{z,m}^{\mathrm{p}}z']} \end{array}\right) \tag{2.33c}$$

$$h_{\theta z}(k_x,\omega,z,z') = \frac{\gamma_n k_x}{2\gamma_m k_{z,m}^{\mathrm{p}}}\left(\begin{array}{l} A_n^{\mathrm{p}}e^{i[k_{z,n}^{\mathrm{p}}(z-z_0)-k_{z,m}^{\mathrm{p}}z']} + B_n^{\mathrm{p}}e^{i[-k_{z,n}^{\mathrm{p}}(z-z_0)-k_{z,m}^{\mathrm{p}}z']} \\ +C_n^{\mathrm{p}}e^{i[k_{z,n}^{\mathrm{p}}(z-z_0)+k_{z,m}^{\mathrm{p}}z']} + D_n^{\mathrm{p}}e^{i[-k_{z,n}^{\mathrm{p}}(z-z_0)+k_{z,m}^{\mathrm{p}}z']} \end{array}\right) \tag{2.33d}$$

where m and n are the indices for a source medium and non-emitting medium, respectively [150-152]. The coordinate system, illustrated in Figure 2.7, is defined such that $z = z_0$ is located at the interface closest to $z = 0$ of a non-emitting medium. $z = 0$ is fixed at the interface between the first and second media, regardless of the source location. The source point dummy spatial variable (z') is integrated for each source layer individually. In this respect, the Poynting vector with multiple sources (i.e., $m = 1, 2, 3...$) requires the summation of Eq. (2.32) for the number of sources.
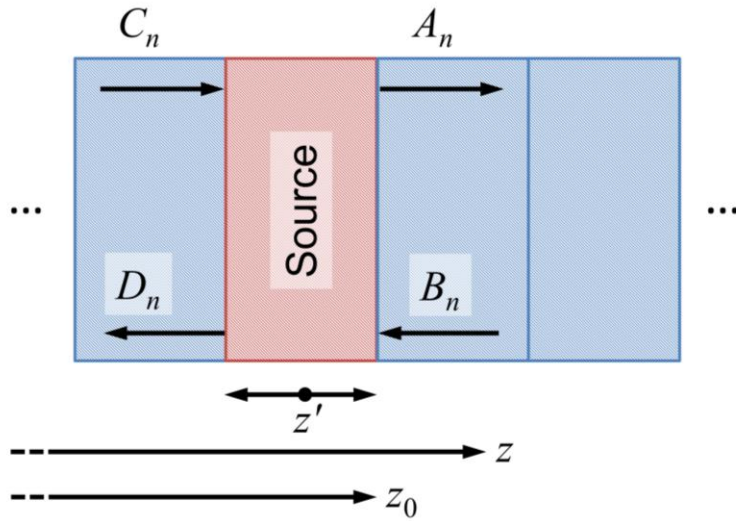
Figure 2.7 Drawing of associated nomenclature used in determining the near-field heat flux components in a 1D multilayer containing a source.

The amplitudes of the forward and backward traveling waves in a non-emitting medium, from a source medium emitting in the positive z direction, are denoted by A_n and B_n, respectively. These coefficients can be solved similarly to the TMM described in Eq. (2.22). A more tedious alternative to this method called the scattering matrix method can be used to avoid singularities in the propagation matrix due to very large complex wavevectors [153,154]. C_n and D_n are the forward and backward amplitudes from a source medium that is emitting in the negative z direction, respectively. The TMM expression for C_n and D_n is given by,

$$\begin{bmatrix} C_n \\ D_n \end{bmatrix} = \left(\prod_{j=n}^{m-1} \mathbf{P}_j \mathbf{D}_j^{-1} \mathbf{D}_{j+1} \right) \begin{bmatrix} C_m \\ D_m \end{bmatrix}$$

(2.34)

The Poynting vector in the z-direction can be used to determine the depth of energy flux within both emitter and receiver, as revisited in Chapter 5.

CHAPTER 3

RADIATIVE PROPERTIES OF CARBON NANOTUBES

In this Chapter, the far-field radiative properties of CNT arrays are modeled and the salient features are discussed. Section 3.1 shows the spectral optical properties or dielectric function of VACNT arrays in the infrared wavelength region. The optical properties are perturbed by filling ratio and alignment factor changes to predict the outcomes of surface reflection. The next section displays the radiative properties of VACNT arrays. Both the angular and incidence angle-dependencies are illustrated. Some special angles such as Brewster angle and principal angle are explained and determined. Penetration depth is defined, and the refraction angles in VACNT are demonstrated within both non-hyperbolic and hyperbolic regions. Section 3.3 introduces tilting to CNT arrays, and primarily addresses the collimation by showing the energy streamlines through the TACNT thin film. In this context, the transmission profiles are studied instead of the absorptance within the coating. The outcomes are summarized in the last section of this Chapter.

3.1 Optical Properties of Carbon Nanotubes

The dielectric functions of a VACNT medium is plotted in Figure 3.1. The filling ratio and alignment factor are $f = 0.05$ and $\xi = 0.98$, respectively. These values are used as the default case for the remaining dissertation regarding CNT arrays. In Fig. 3.1(a), the real part of the dielectric function in the ordinary direction (ε'_O) is close to unity. This suggests impedance matching between VACNT medium and vacuum, resulting in low reflectance and high broadband absorption [31,33,155,156]. Note that the dielectric

function in the extraordinary direction (ε_E') becomes negative at certain wavelengths due to the high conductivity along the CNT axis. The shaded regions indicate the wavelength ranges where the hyperbolic dispersion exists, in this case of Type I since both are defined by $\varepsilon_O' > 0$ and $\varepsilon_E' < 0$. The wavelength region bounds are: 14.4 μm $< \lambda < 63.4$ μm (Region 1), and 90.1 μm $< \lambda < 133$ μm (Region 2). Fig. 3.1(b) shows the imaginary parts of the dielectric function in both ordinary and extraordinary directions. The magnitude of the ordinary component is almost two orders magnitude smaller than its extraordinary counterpart.
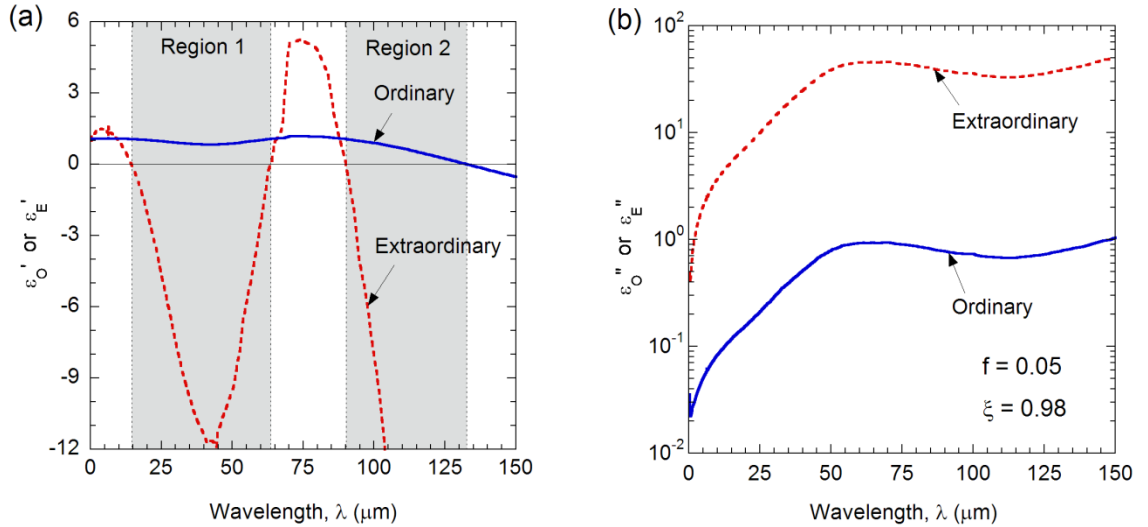
Figure 3.1   Ordinary and extraordinary relative permittivities of VACNT with fixed filling ratio ($f = 0.05$) and alignment factor ($\xi = 0.98$). These values are used as default in the calculations unless otherwise specified. (a) Real parts with hyperbolic regions identified as Region 1 and Region 2, and (b) the imaginary parts.

Figure 3.2 shows the optical constants of VANCT films for wavelength from 1 μm to 1000 μm. The upper wavelength bound is close to the minimum frequency ($\hbar\omega = 0.001$ eV) obtained from Ref. [119]. Here, both filling ratio and alignment factor are slightly varied individually to illustrate the effect of these deviations on the optical

constants. The range of filling ratio in fabricated VACNT films is typically between 0.01 and 0.15 [50]. At wavelengths from 1 μm to about 30 μm, n_O is close to 1 and κ_O is relatively small. This results in an impedance matching and high absorptance for incidence from air at least for normal incidence. In this region, n_O is insensitive to both f and ξ, κ_O depends on both because decreasing the packing density or alignment factor can result in less loss (or a reduction of κ_O). Beyond 30 μm, the effect of interband transition results in a resonance feature that appears in the optical constants of VACNT. Furthermore, free electron absorption becomes important beyond 100 μm, resulting in an increase in the predicted optical constants of CNTs toward longer wavelength. While the trends of extraordinary optical constants are similar, the values are much higher than the corresponding ordinary optical constants, especially κ_E, which is about an order of magnitude higher than κ_O. However, at oblique incidence, high values of ε_E'' relative to ε_O'' do not necessarily mean poor absorption as described by Feng [82,157].

At longer wavelengths, the filling ratio affects the optical constants significantly. On the other hand, only the ordinary components appear to be dependent on the alignment factor. This is because the extraordinary optical constants are much greater than the ordinary counterparts. A small change in alignment factor has a bigger impact on the weighted average according to Eq. (2.9). The dielectric function model presented in Eq. (2.8) is in good agreement with the mid-infrared transmittance measurements at normal incidence [137]. The optical constants obtained in the far-infrared, especially for the extraordinary components, are much higher than those reported in Ref. [49], by transmission ellipsometry in the wavelength between 190 μm and 750 μm. The

disagreement could be due to the CNT density or filament structure of the fabricated VACNT samples. It should also be mentioned that while interband transitions were also observed for single-walled CNT arrays, the strength is often much weaker than that in graphite [46]. Because of the limited data on the far-infrared optical properties of CNTs, the optical constants of graphite are adopted in the present work.
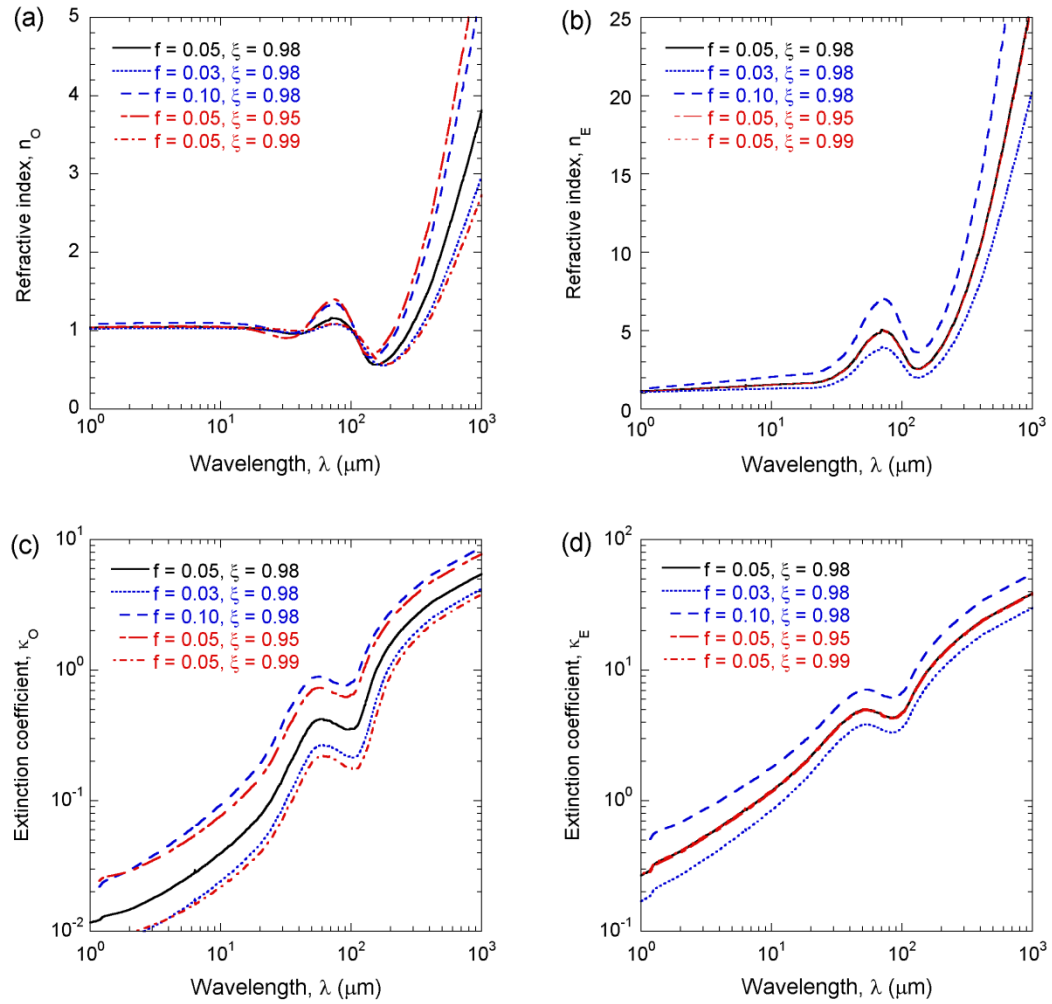
Figure 3.2 Optical constants of VACNT with varying filling ratios and alignment factors up to wavelength $\lambda = 1000\ \mu\mathrm{m}$. (a) and (b) Refractive indices for ordinary and extraordinary waves, respectively. (c) and (d) Extinction coefficient for ordinary and extraordinary waves, respectively.

3.2 Vertically Aligned Carbon Nanotube Arrays

The radiative properties of semi-infinite uniaxial medium can be formulated using the surface admittance or impedance coefficients [93,155]. Detailed formulation and simplified expressions of the radiative properties are discussed in Section 2.3. Since the VACNT coating is generally thicker than the characteristic wavelength, Airy's formulae can be applied to obtain the reflectance and transmittance for a CNT film on a substrate.

3.2.1 Reflectance of Semi-Infinite Arrays

The normal reflectance of a VACNT medium is shown in Figure 3.3 for varying filling ratios and alignment factors. For $\lambda < 20$ μm, the reflectance $R'_\lambda < 0.01$ for all cases, and $R'_\lambda < 0.0015$ for the default filling ratio and alignment factor values. Reducing the filling ratio can further reduce the reflectance. In the interband transition region (30 μm < $\lambda < 100$ μm), the reflectance increases to 0.03-0.04 in the default case and differs greatly with the changes in either f or ξ. VACNT becomes highly reflecting at far-infrared ($R'_\lambda > 0.5$) when the wavelength exceeds 200 μm for the default case and the reflectance is smaller with reduced filling ratio or increased alignment factor. It appears that the filling ratio affects more in the near- to mid-infrared region, while the alignment factor has a stronger effect in the far-infrared. The absorptance, $A'_\lambda = 1 - R'_\lambda$, is very close to unity in the near- and mid-infrared region. In the far-infrared, the absorptance decreases. However, reducing the filling ratio and improving alignment can increase the absorptance. It should be noted that high absorptance was reported for single-walled VACNT films at wavelengths up to 200 μm [33]. The experimentally observed high
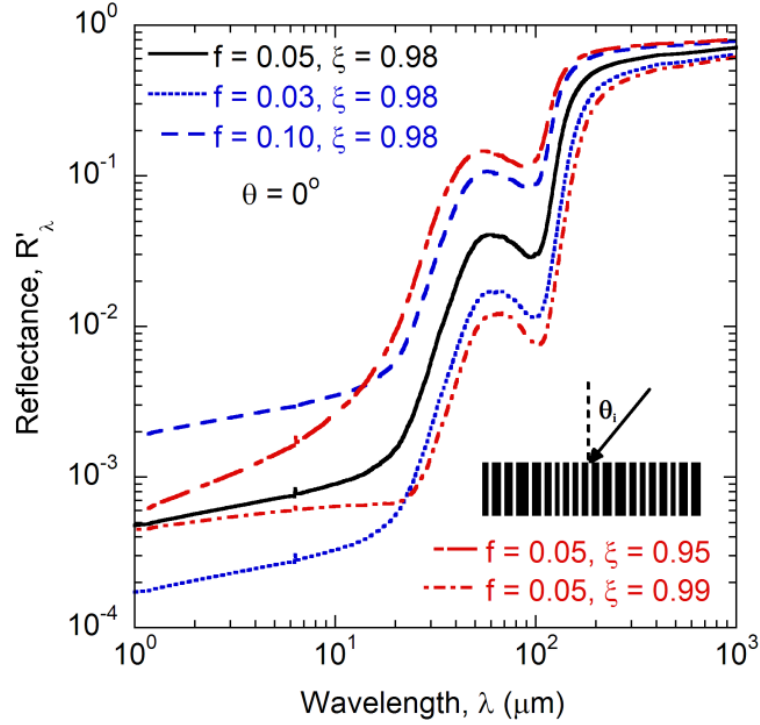
Figure 3.3 Normal incidence reflectance spectra of a semi-infinite VACNT array with varying filling ratios and alignment factors. The inset illustrates the incidence angle upon the VACNT array.

absorptance may be due to the reduction of the interband and free-electron absorption, along with surface roughness effects that could enhance radiation absorption.

To study the angular and polarization dependence, the contour plots of reflectance for s- and p-polarization are shown in Figure 3.4. The contour traces identify the iso-reflectance lines. For s-polarization, the reflectance increases with the angle of incidence for all wavelengths, as shown in Fig. 3.4(a). Furthermore, the reflectance increases with wavelength similar to the case for normal incidence. At the grazing angle, $\theta_i = 90^o$, the reflectance for both polarizations approaches unity as expected. However, for p-polarizations, the reflectance may reach a minimum at an oblique angle. As shown in Fig. 3.4(b), there is a global minimum at $\lambda = 4.6\ \mu m$ and $\theta_i = 20.2°$, where reflectance sharply

drops by several orders of magnitude. This phenomenon is further explored in the following section.

3.2.2 Special Angular Properties

The incidence angle at which the reflectance becomes zero for p-polarization is defined as the Brewster angle θ_B, at which all the incident energy is transmitted into the
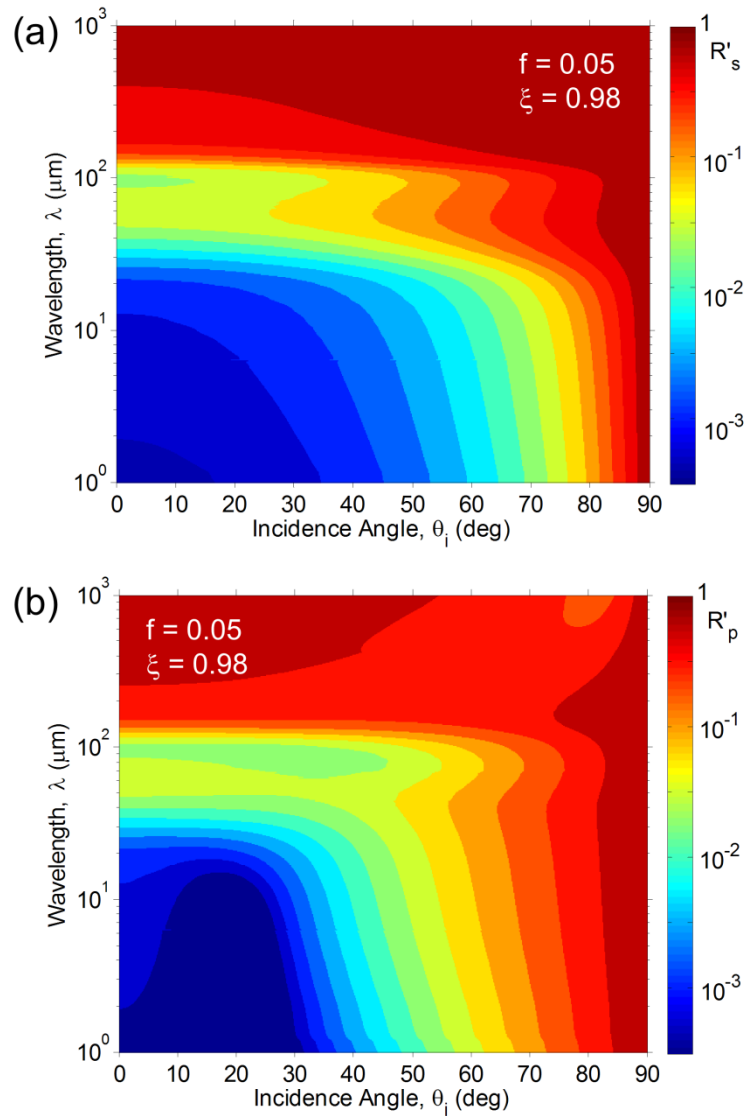
Figure 3.4 Color contours of the specular reflectance versus wavelength and incidence angle for: (a) s-polarization and (b) p-polarization. The VACNT array is semi-infinite.

medium [3]. Perfect transmission holds for a lossless dielectric medium only. For real materials, the angle at which R'_p is minimized is called the Brewster angle, which may not exist for a high loss medium. Materials with well-defined Brewster angles are frequently used as angular polarizers. The wavelength-dependent Brewster angles of VACNT coatings are shown in Figure 3.5(a). The abscissa and ordinate are interchanged so that one can refer the location of the Brewster angle with the minimum of R'_p in Fig. 3.5(b). Note the Brewster angle is not defined for $28\ \mu m < \lambda < 39\ \mu m$ and for $110\ \mu m < \lambda < 142\ \mu m$. These wavelength bounds correspond almost exactly to the hyperbolic wavelength regions illustrated in Fig. 3.1(a).
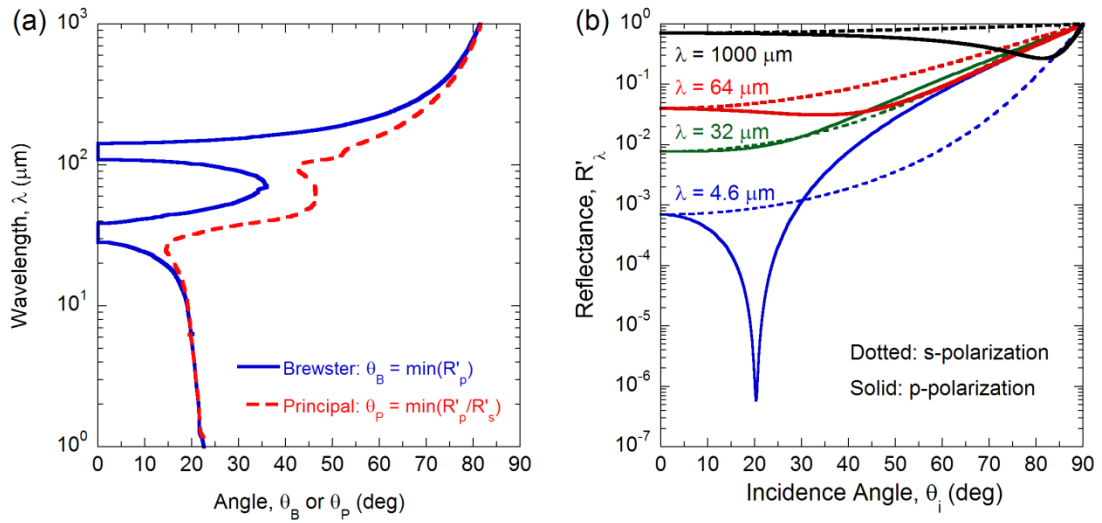
Figure 3.5 (a) Correlation of the Brewster angle θ_B and the principal angle θ_P with the wavelength. The abscissa and ordinate are interchanged in order to compare the traces with Figure 3.4(b). (b) The reflectance as a function of the incidence angle for both polarizations at four distinct wavelengths.

The principal angle θ_P is defined as the minimum of the ratio of the p-polarized to the s-polarized reflectance [158]. The principal angle is also shown in Fig. 3.5(a) and can be defined for all wavelengths. At wavelengths $\lambda < 10\ \mu m$ where loss is small, the

Brewster angle and principal angle are close to each other. For an isotropic dielectric medium with $n > 1$, the Brewster angle is always greater than 45°. This does not hold in general for an anisotropic medium [51]. The angular behavior is further explored by calculating the angular-dependent reflectance for each polarization at different wavelengths, as shown in Fig. 3.5(b). At $\lambda = 4.6$ μm, the p-polarization reflectance drops sharply at the Brewster angle ($\theta_B = 20.2°$), by several orders magnitude. At this wavelength, the Brewster angle and principal angle are coincident. In the case of $\lambda = 32$ μm, the Brewster angle is undefined and R'_p increases monotonically with θ_i. For $\lambda = 64$ μm, R'_p exhibits a shallow dip around 34°, and there is a large mismatch between θ_B and θ_P. At $\lambda = 1000$ μm, where $\theta_B \approx \theta_P$, there is a distinct dip in R'_p at 81.3°. Therefore, the mismatch between the Brewster angle and principal angle in Fig. 3.5(a) indicates the wavelength region where the Brewster angle becomes poorly defined.

To understand why no Brewster angle exists in the hyperbolic wavelength regimes, the refraction angles in the VACNT medium is explored. The wavevector refraction angle (θ_k) and the Poynting vector refraction angle (θ_S) are defined respectively as follows [80,159],

$$\tan(\theta_k) = \left.\frac{\mathrm{Re}(k_x)}{\mathrm{Re}(k_z)}\right|_{z=0^+} \tag{3.1}$$

$$\tan(\theta_S) = \left.\frac{S_x}{S_z}\right|_{z=0^+} \tag{3.2}$$

When the optical axis of the uniaxial anisotropic medium is in the z direction (i.e., $\beta = 0°$), the Poynting vector components can be simplified to $S_x = \mathrm{Re}(k_x / \varepsilon_E)$ and

$S_{\tilde{z}} = \mathrm{Re}(k_{\tilde{z}} / \varepsilon_O)$. In this case, when the magnitude of ε_E is very large, the Poynting

vector is close to normal or parallel to the CNTs. The refraction angles versus the angle

of incidence are shown in Fig. 3.6 at three wavelengths chosen from three different

regions. At $\lambda = 1$ μm with elliptic dispersion, both refraction angles are positive for all

incidence angles. For $\lambda = 20$ μm in Region 1 and 100 μm in Region 2 hyperbolic bands,

θ_k is positive, but the Poynting vector or energy refraction angle θ_S becomes negative.

No Brewster angle can occur for single-negative permittivity materials with negative

refraction of Poynting vectors [147]. The negative refraction reflects the characteristics of

a hyperbolic material. Furthermore, the magnitude of θ_S is very small, suggesting that

the energy refraction tends to align with the optical axis or along the carbon nanotubes.
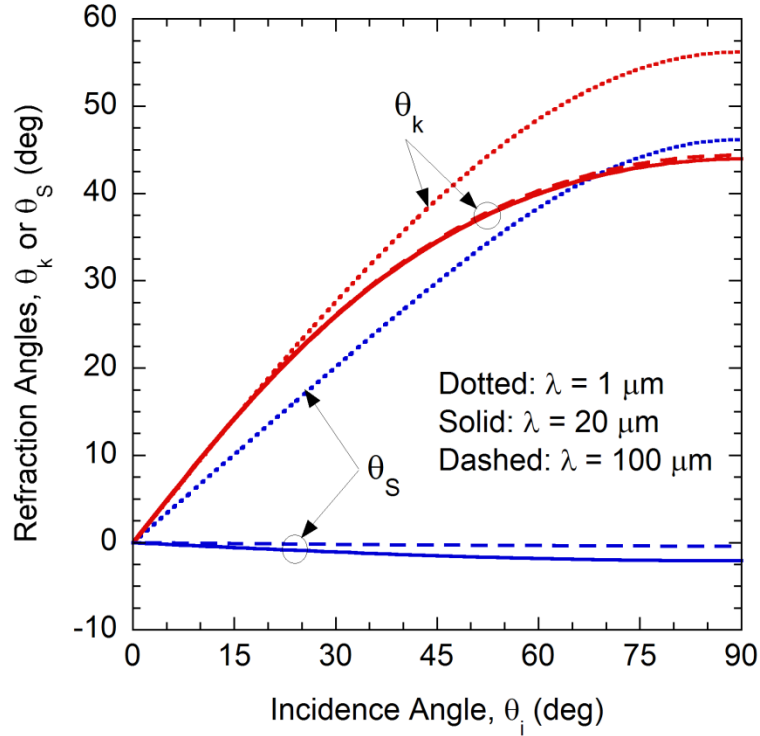
Figure 3.6   Refraction angles at the vacuum-VACNT interface for the wavevector (θ_k) and Poynting vector (θ_S).

3.2.3 Penetration Depth

It is important to examine the penetration depth in order to determine how thick the VACNT film is needed for it to be opaque so that the substrate effect is negligible. The radiation penetration depth is defined as where the power of the electromagnetic wave entering the medium will decay by $e^{-1} \approx 37\%$ from the interface. The spectral penetration depth can be expressed as [3],

$$\delta_\lambda = \frac{1}{2\,\mathrm{Im}(k_z)} \tag{3.3}$$

where k_z is the z-component wavevector for either s- or p-polarizations. The predicted penetration depths for s- and p-polarizations are shown in Figure 3.7(a) and Fig. 3.7(b), respectively. At normal incidence, the penetration depth becomes $\delta_\lambda = \lambda/(4\pi\kappa_O)$ regardless of the polarization status, where κ_O is plotted in Fig. 3.2(c). In the near-infrared, penetration depth increases up to $\delta_\lambda = 21$ μm around $\lambda = 15$ μm. Because of the interband transition, penetration depth decreases to about $\delta_\lambda = 10$ μm around $\lambda = 50$ μm. The penetration depth then increases to reach a peak at wavelength slightly longer than 100 μm, which is beyond the interband transition and before the Drude model takes effect in the far-infrared. Here, the penetration depth reaches up to $\delta_\lambda = 23.6$ μm. There is another minimum in δ_λ at wavelengths between 200 μm and 300 μm. As the wavelength further increases, δ_λ increases with the square root of wavelength, as predicted by the Drude free electron model [3].

The angular dependence of the penetration depth is different for s- and p-polarizations. In the near-infrared, the penetration depth decreases with increasing

incidence angle in a similar way for both polarizations since the ordinary and extraordinary dielectric functions are of the same order of magnitude close to unity. In the intermediate region, because the magnitude of ε_O is smaller than that of ε_E, the penetration depth for p-polarization becomes independent of θ_i at a relatively shorter wavelength of about 50 μm. At very long wavelengths beyond 500 μm, the dielectric function is magnitudes larger than k_x and therefore, the penetration depth is independent of the angle of incidence. Based on the penetration depth, CNTs with a thickness greater than 100 μm can generally be considered opaque.
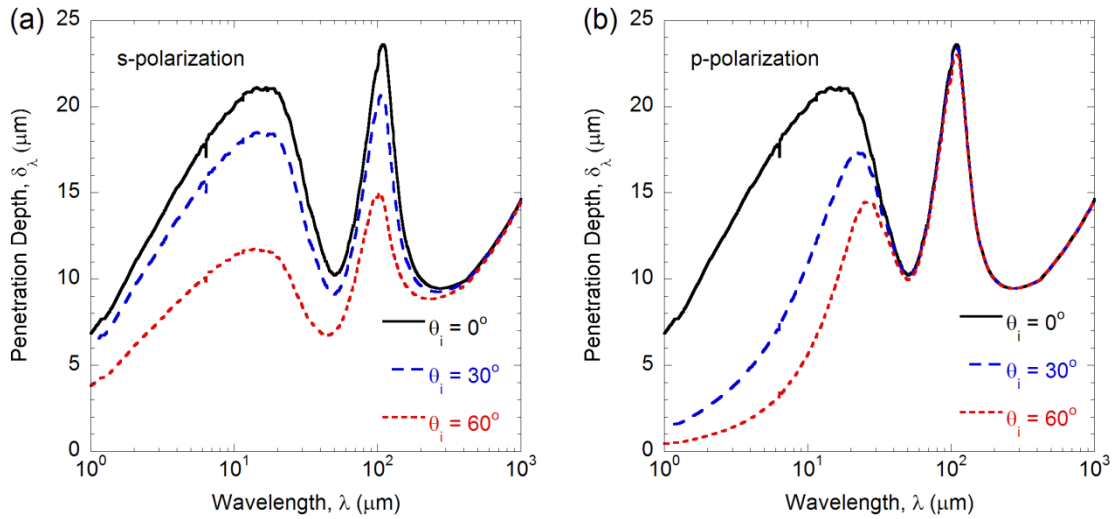
Figure 3.7 Radiation penetration depths for (a) s-polarization and (b) p-polarization at incidence angles $\theta_i = 0°$, $30°$, and $60°$.

The penetration depth versus incidence angle at the two wavelengths selected from different hyperbolic bands is shown in Figure 3.8. The penetration depth is greater at $\lambda = 100$ μm than at $\lambda = 20$ μm for all incidence angles. Furthermore, the penetration depth at $\lambda = 100$ μm depends little on the incidence angle. This is because the magnitude

of ε_E is so large that $\varepsilon_E^{-1}\sin^2\theta_i \ll 1$ for any θ_i. Fig. 3.8 also suggests that improving

alignment can increase the penetration by several times. Reducing the filling ratio alone

from $f = 0.10$ to 0.03 also improves penetration depth (not shown), but it is not as

effective as changing the alignment factor from $\xi = 0.95$ to 0.99. Although the

penetration depth in Region 2 ($\lambda = 100\ \mu m$) may be desired, the previous subsection

demonstrated some setbacks at the far-infrared wavelengths, namely higher reflectance at

the interface between air and the VACNT array. The penetration depth informs us of the

thickness needed for reducing internal reflections in VACNT coatings. However, thinner

film coatings are often desired to reduce material consumption and growth time. The

effect of thickness and substrate on the absorptance of CNT films is discussed in the next

subsection.
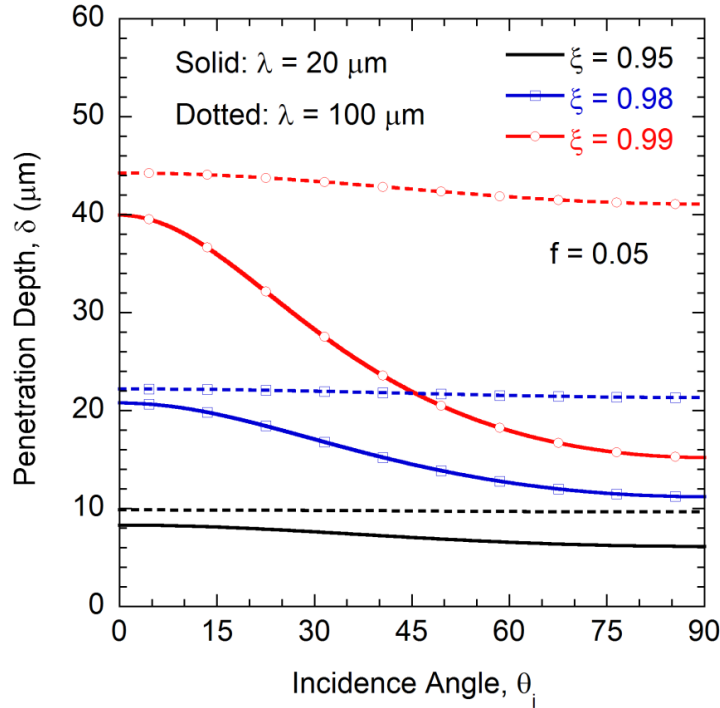
Figure 3.8 Radiation penetration depth in VACNT with varying alignment factors for p-polarization. The wavelengths selected ($\lambda = 20\ \mu m$ and $100\ \mu m$) are in hyperbolic Region 1 and Region 2 of Figure 3.1(a), respectively.

3.2.4 Absorptance of CNT Arrays

The directional-spectral emittance is integrated over the solid angle, Ω, is $\left(d\Omega = \cos\theta_i \sin\theta_i d\theta_i d\phi_i \right)$ to obtain the hemispherical emittance $\epsilon_{\mathrm{hem},\lambda}$ [3]:

$$\epsilon_{\mathrm{hem},\lambda} = \frac{1}{\pi} \int_0^{2\pi} \int_0^{\pi/2} \epsilon_\lambda' \cos\theta_i \sin\theta_i d\theta_i d\phi_i \qquad (3.4)$$

According to Kirchhoff's law, the directional-spectral absorptance is equal to the directional-spectral emittance ϵ_λ', if the temperature of the material is uniform at least within several penetration depths. This states that $A_\lambda' = \epsilon_\lambda' = 1 - R_\lambda'$ for a semi-infinite medium. If the intensity of the incident radiation is independent of the direction (diffuse incidence), then the hemispherical absorptance equals the hemispherical emittance: $A_{\mathrm{hem},\lambda} = \epsilon_{\mathrm{hem},\lambda}$. The hemispherical absorptance spectra are shown in Figure 3.9, for both s- and p-polarizations, as well as their average, for the default f and ξ values. In the near- and mid-infrared region, the hemispherically integrated absorptance is higher (exceeding 0.98 at $\lambda < 15$ μm) for s-polarized incident waves. At wavelengths longer than 40 μm, the hemispherical absorptance for p-polarization is higher than that for s-polarization. In general, the hemispherical absorptance is smaller than the normal absorptance due to angular dependence, although surface roughness can give rise to increased hemispherical absorptance [32].

The absorptance spectra of VACNT of different thickness on Si substrate are shown in Fig. 3.10 for both polarizations at different angles of incidence and with varying CNT film thickness. In the calculation, the optical constants of lightly doped Si is taken from Ref. [160] and extended to the far-infrared by assuming a constant refractive index of 3.42 and negligible loss. At normal incidence, the results for both polarizations are the
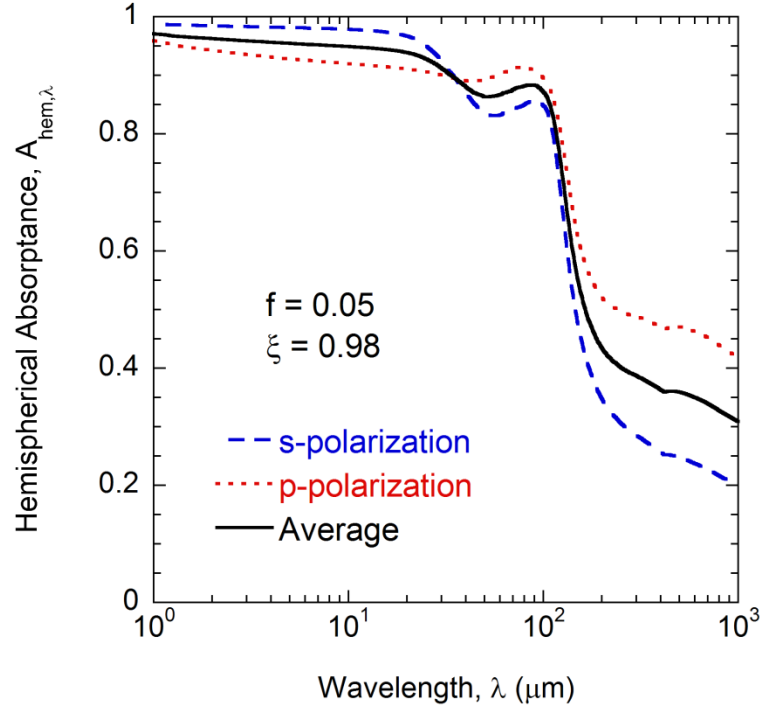
Figure 3.9 Hemispherical absorptance spectra for s- and p-polarization, and the average of the two.

same. For the 10 μm-thick VACNT thin film, as shown in Figures 3.10(a) and (b), the absorptance is significantly reduced. For normal incidence, the maximum absorptance is $A'_\lambda = 0.8$ at $\lambda = 1$ μm and decreases with wavelength until $\lambda = 20$ μm. Interference effects can be clearly observed in the near- and mid-infrared region. Interband transition causes an absorptance peak at wavelengths between 50 μm and 100 μm. At $\lambda = 100$ μm, corresponding to the maximum penetration depth peaks, the CNT absorption is minimum at $A'_\lambda = 0.1$. At short wavelengths, increasing the angle of incidence gives rise to a higher absorptance due to the decreasing penetration depth as shown in Fig. 3.7. However, for p-polarization, the absorptance is higher at $\theta_i = 30°$ than $60°$ due to the Brewster angle at which the reflection coefficient at the air-VACNT interface is minimized is around 20°. The outcome is complicated due to the interplay of

interference, internal absorption, and surface reflection. Interestingly, at longer wavelengths ($\lambda > 100$ μm), the absorptance improves toward oblique incidence for p-polarization, but reduces for s-polarization. This can be explained by interface reflection being higher for s-polarization than that for p-polarization as illustrated in Fig. 3.4. Furthermore, the Brewster angle is relatively large and the reflection coefficients decrease with increasing θ_i for p-polarization. This trend is the same for all three CNT thicknesses because it is related to the interface effect rather than internal absorption.

Increasing the thickness of the VACNT film improves absorptance (especially in the near- and mid-infrared) and reduces interference effects. This can be seen by comparing the trends from figures for each polarization in Fig. 3.10 from top to bottom. The interference effect almost diminishes for $d = 50$ μm, as shown from Figs. 3.10(e) and (f) and the absorptance is closer to that of semi-infinite medium except for regions with large penetration depths. Calculations were also made for $d = 100$ μm with slight differences from those for $d = 50$ μm, which suggest that for most wavelength regions, a CNT thickness of at least $d = 50$ μm can be approximated as semi-infinite.
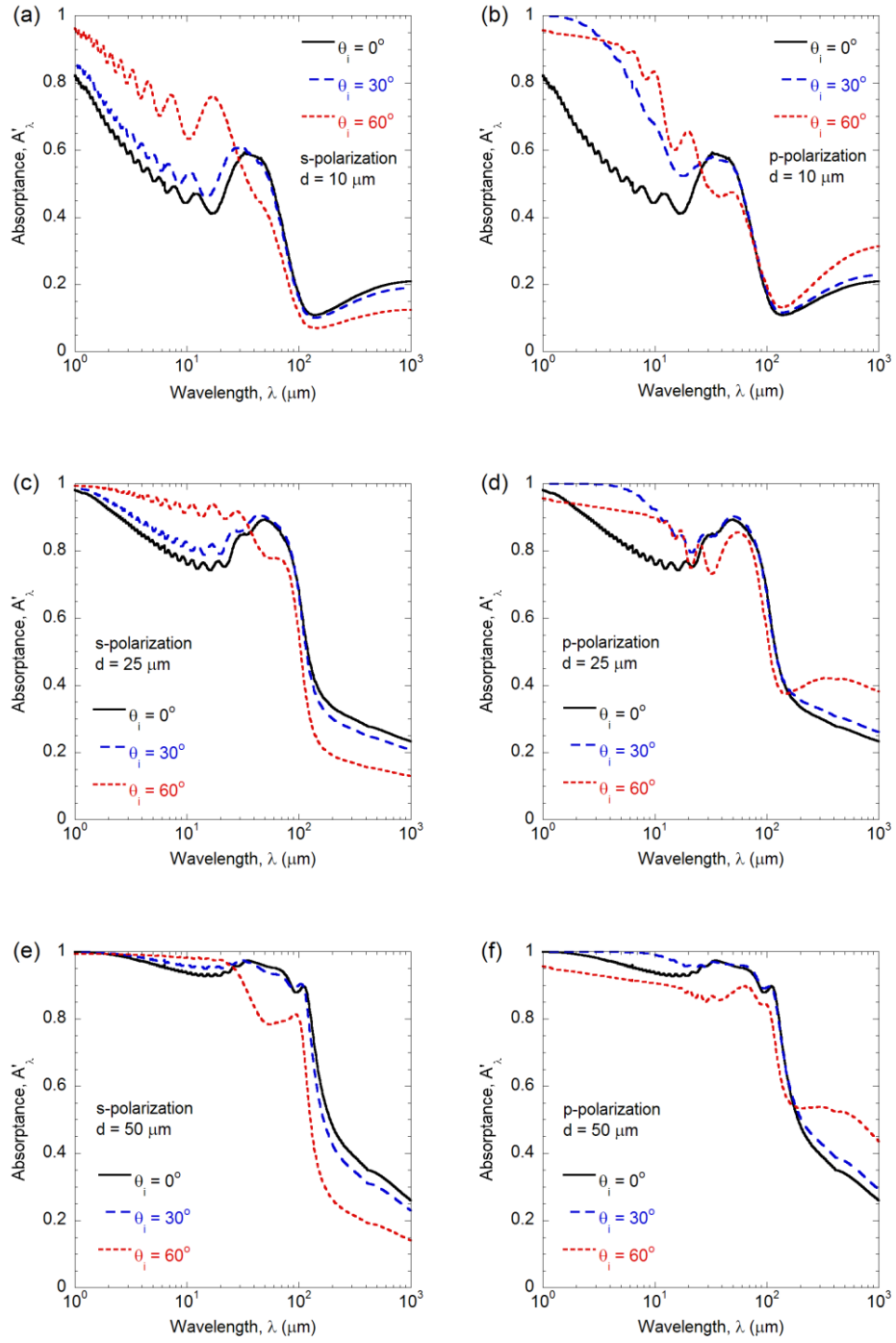
Figure 3.10 Absorptance of VACNT film of different thicknesses at incidence angles of $\theta_i = 0°$, 30°, and 60°: (a) s-polarization with $d = 10\ \mu$m, and (b) p-polarization with $d = 10\ \mu$m. (c) s-polarization with $d = 25\ \mu$m, and (d) p-polarization with $d = 25\ \mu$m. (e) s-polarization with $d = 50\ \mu$m, and (f) p-polarization with $d = 50\ \mu$m.

3.3 Tilted Carbon Nanotube Arrays

In the remaining Chapter, the CNT array is tilted at various tilting angles (β) and compared to the previously only vertically aligned case ($\beta = 0°$). The radiative properties are focused in the hyperbolic wavelength regimes, in order to show unconventional dispersion and refraction of waves.

3.3.1 Reflectance and Transmittance

The reflectance is calculated at $\lambda = 20$ μm and 100 μm using the Fresnel reflection coefficient at the interface [3,93]. The results are plotted in Figure 3.11 as functions of incidence angle for both polarizations. Since the CNT array is treated as a homogeneous medium with a smooth interface, surface scattering and volume scattering are not considered here. As mentioned earlier, the reflectance for TE waves is independent of the tilting angle. For the VACNT array, the incidence angle for minimum reflectance is described by the Brewster angle for TM waves which increases with the effective refractive index. It is interesting to note that at oblique incidence, the reflectance is minimized at incidence angles close to the tilting angle, especially for large β, at both wavelengths. In tilted CNT arrays, reflectance is higher at normal incidence for both wavelengths. At $\lambda = 20$ μm, the reflectance is reduced by several order magnitudes when the incidence angle coincides with the tilting angle ($\theta_i = \beta$). Due to loss, the reflectance at $\lambda = 100$ μm is generally higher than that at $\lambda = 20$ μm. Despite the relatively greater penetration depth at $\lambda = 100$ μm, as discussed in the preceding section, surface reflection loss may be more significant at longer wavelengths.

51
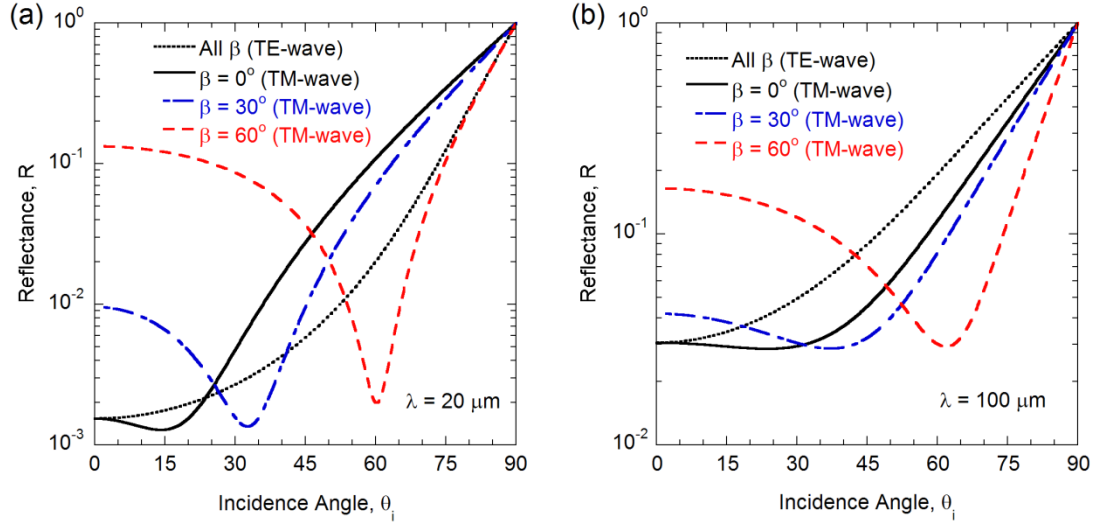
Figure 3.11 Reflectance of VACNT and TACNT arrays with and without tilting for (a) $\lambda = 20\ \mu$m and (b) $\lambda = 100\ \mu$m. Note that for TE waves the reflectance is independent of the tilting angle β.

Figure 3.12 shows the transmittance (T) through a $d_2 = 10\ \mu$m-thick VACNT or TACNT array as a function of the incidence angle. As shown in Fig. 3.12(a) for $\lambda > 20\ \mu$m, the transmission is symmetric and reaches a peak at normal incidence for TE waves regardless of tilting or for TM wave when $\beta = 0°$ (VACNT). For TACNT thin films, the transmittance is favored when the incidence angle is around the tilting angle. For example, in the CNT thin film with $\beta = 60°$, the transmittance at negative incidence angles is nearly zero. For $\lambda = 100\ \mu$m, the transmittance is generally higher and insensitive to incidence angle for $-60° \le \theta_i \le 60°$ and $0° \le \beta \le 30°$, as shown in Fig. 3.12(b). For VACNT, the transmittance plateaus in a broad incidence angle range $|\theta_i| < 60°$. Moreover, in TACNT thin films, the transmittance remains high even with negative incidence angles until β exceeds 60°.

52
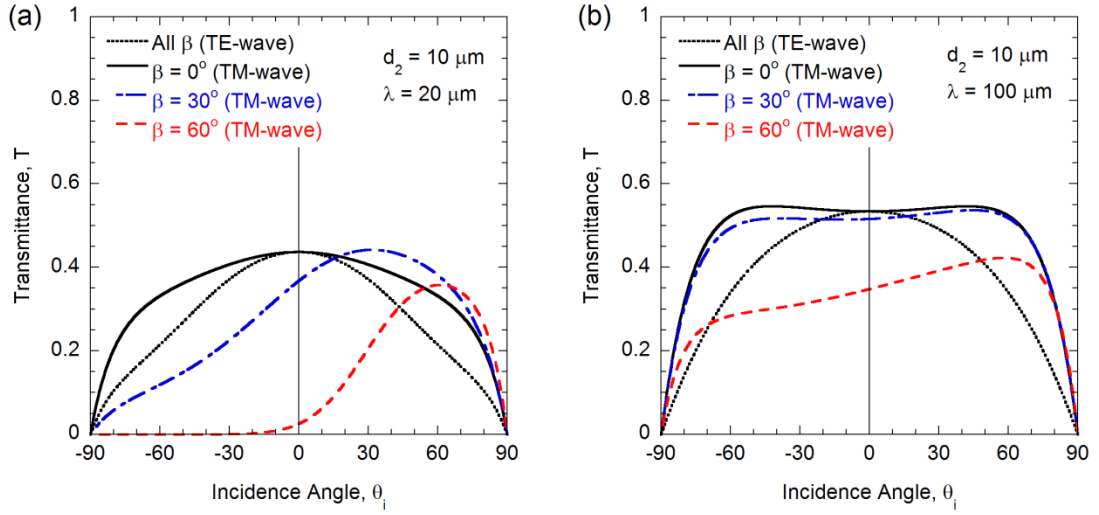
Figure 3.12   Transmittance through VACNT and TACNT thin films of thickness $d_2 = 10$ μm with various tilting angles at (a) $\lambda = 20$ μm and (b) $\lambda = 100$ μm.

The penetration depth is plotted in terms of the wavelength as shown in Figures 3.13(a) and (b) with $\beta = 30°$ and $60°$, respectively. The penetration depth for tilted CNT arrays is calculated using Eq. (3.3) by setting $k_z = k_z^+$ according to Eq. (2.19). The spectral behavior of the penetration depth is associated with the trend of the extinction coefficient due to the free carriers and far-infrared interband transition in graphite. The penetration depth is the highest at all wavelengths when $\theta_i = \beta$. This trend supports the low-loss transmission characteristic, but now along the coordinate-transformed optical axis. In addition, the magnitudes of the penetration depth differ between the two tilting angles. In more heavily tilted CNT, the average penetration depth is reduced almost by half. This is explained by the longer length of heavily tilted CNT filaments at a given depth from the surface. The minimal reflectance and maximal penetration depth when the incidence angle is coincident with the tilting angle demonstrate high transmission in

53

TACNT arrays along the optical axis. In the following, the all-angle self-collimation is demonstrated for CNT arrays with or without tilting.
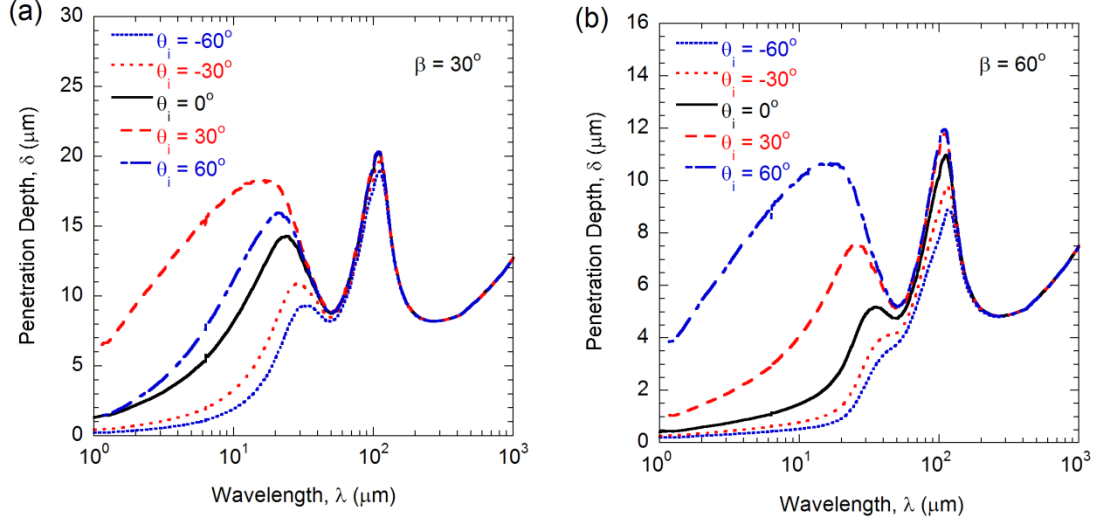
Figure 3.13 Penetration depths of TACNT arrays at various incidence angles for (a) $\beta = 30°$ and (b) $\beta = 60°$.

3.3.2 Hyperbolic Dispersion and Energy Streamlines

Figure 3.14 shows the isofrequency contour plots in the k_x-k_z space at $\lambda = 20 \ \mu$m for various tilting angles. Note that the wavevectors are divided by k_0. Taking Fig. 3.14(a) for VACNT as an example, the unit circle is the isofrequency curve for wavevector $\mathbf{k}_i$ of the incident wave divided by k_0. The incident Poynting vector $(\mathbf{S}_i)$ is parallel to the wavevector and perpendicular to the isofrequency curve. For the hyperbolic dispersion described by Eq. (2.11), the solutions of the real part of k_z are the upper and lower hyperbolic branches. Due to loss, the solution also results in a positive imaginary part of k_z, as indicated by the dotted curve. The resultant Poynting vector $(\mathbf{S}_{\text{CNT}})$ is perpendicular to the isofrequency curve for $\text{Re}(k_z / k_0)$ [80,142]. The

54

wavevector in the CNT, $\mathbf{k}_{\text{CNT}}$, begins from the origin and ends at the hyperbolic dispersion curve with the condition that $k_x = k_0 \sin \theta_i$. Furthermore, the requirement for the z-component of $\mathbf{S}_{\text{CNT}}$ to be positive necessitates that the upper branch of the isofrequency curve corresponds to waves incident from vacuum to the CNT. As indicated in Fig. 3.14(a), the Poynting vector points slightly leftward, suggesting negative energy refraction. Since the isofrequency contour is rather flat, the Poynting vector is nearly parallel to the z-axis or the nanotubes. This is in agreement with the energy refraction angles seen in Fig. 3.6.

The remaining isofrequency contours shown in Figs. 3.14(b-d) demonstrate the refraction and self-collimation for tilted CNT arrays at $\beta = 30°$, 60°, and 70°, respectively. Since the optical axis forms an angle β with respect to the surface normal, the dispersion relation is taken from Eq. (2.25). In Fig. 3.14(b), the $\text{Re}(k_z / k_0)$ line is slanted along the tilting angle, resulting in all Poynting vectors pointing toward approximately θ_S = 30°. For $\beta = 60°$, as shown in Fig. 3.14(c), the self-collimation mechanism remains the same as the Poynting vectors point toward the tilting angle. However, toward large negative k_x, the $\text{Re}(k_z / k_0)$ curve is slightly bent. The situation is more prominent in the case for $\beta = 70°$ as shown in Fig. 3.14(d), where the dispersion curve undulates toward negative k_x. Self-collimation breaks down when radiation is incident from the opposite side (i.e., $\theta_i < 0°$) for CNT arrays with large tilting angles. The vertical dotted lines in Figs. 3.14(b-d) are for $k_x / k_0 = \sin \beta$ or $\theta_i = \beta$. It can be seen that $\text{Im}(k_z)$ is near its minimum or loss is minimized at $\theta_i \approx \beta$ as mentioned previously.
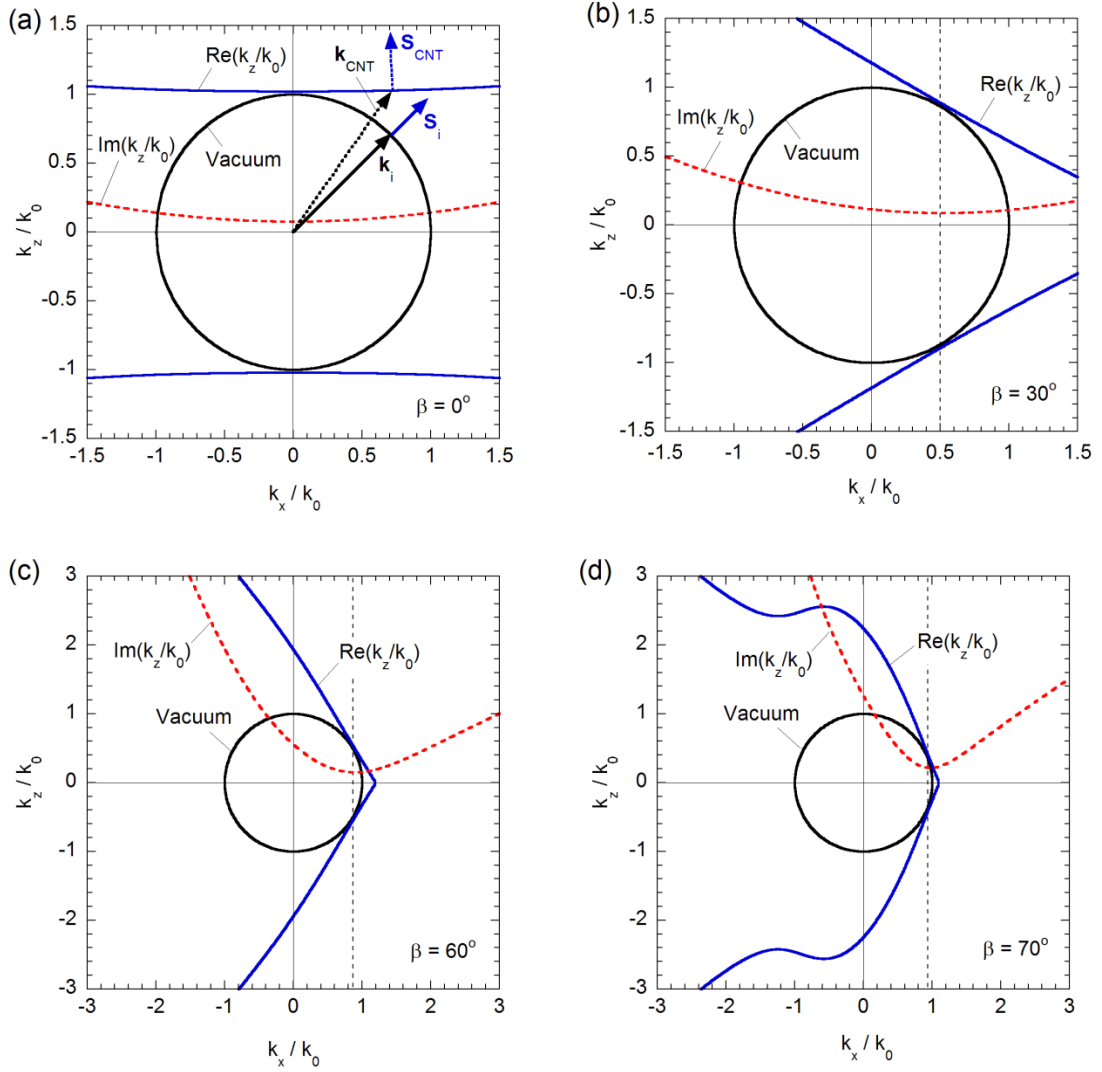
Figure 3.14 Normalized hyperbolic dispersion iso-frequency diagrams at $\lambda = 20$ μm for (a) VACNT, and TACNT arrays with tilting angles at (b) $\beta = 30°$, (c) $\beta = 60°$, and (d) $\beta = 70°$.

For isofrequency contours at $\lambda = 100$ μm (not shown), $Im(k_z/k_0)$ lines are greater in magnitude. Interestingly, for heavily tilted CNT ($\beta = 70°$) at $\lambda = 100$ μm, the undulation of the $Re(k_z/k_0)$ line at negative k_x is not as evident. This signifies that self-collimation is more inclusive at $\lambda = 100$ μm, but the waves propagating in CNT may suffer from more surface and internal losses. Even though the absolute penetration depth

56

is slightly greater, when normalized to the wavelength, δ / λ generally decreases toward longer wavelengths.

The refraction angles for TACNT are shown in Figure 3.15 for $\lambda = 20$ μm along with that for VACNT for comparison. The wavevector refraction angle has the same sign as the incidence angle, as shown in Fig. 3.15(a). The energy refraction angles shown in Fig. 3.15(b) can help better interpret the observations made above for Fig. 3.14. It should be noted that the energy refraction angle is determined from Eq. (3.2), where the Poynting vector components for TACNTs are given by

$$S_x = \mathrm{Re}\left(\frac{k_x \varepsilon_{xx} + k_z \varepsilon_{xz}}{\varepsilon_O \varepsilon_E} \right) \tag{3.5a}$$

$$S_z = \mathrm{Re}\left(\frac{k_x \varepsilon_{xz} + k_z \varepsilon_{zz}}{\varepsilon_O \varepsilon_E} \right) \tag{3.5b}$$
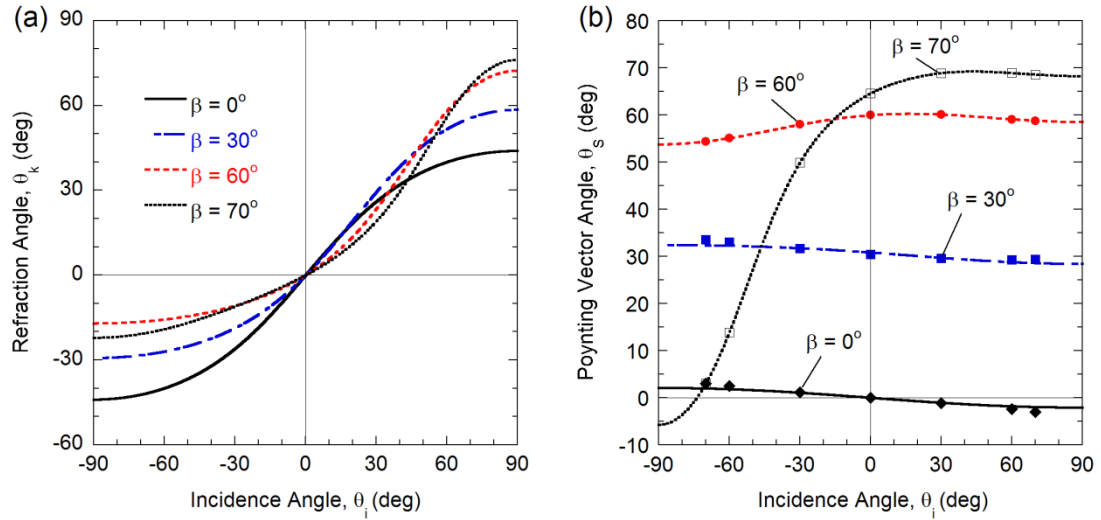
Figure 3.15 (a) Wavevector refraction angle (θ_k) for tilted CNT array at $\lambda = 20$ μm and (b) energy refraction angle (θ_S) calculated from Eq. (3.2). For comparison, the Poynting vector refraction angles obtained from the transfer matrix method for CNT thin films of $d_2 = 10$ μm are shown as marks.

Clearly, θ_S largely follows the CNT tilting angle for any incidence when $\beta < 60°$. With heavily tilted CNTs, especially when $\beta = 70°$ and for negative θ_i, θ_S deviates significantly from the tilting angle. In the case with $\lambda = 100\ \mu$m, θ_S is almost constant for all incidence angles (although not shown here), indicating near-perfect self-collimation. In Fig. 3.15(b), the data points indicate the Poynting vector refraction angle calculated using transfer matrix formulation for a thin film of $d_2 = 10\ \mu$m. The agreement suggests that surface refraction dominates the Poynting vector direction in the CNT film, although interference effects can modify it slightly.

Energy streamlines are obtained for a thin CNT film with $d_2 = 10\ \mu$m for various incidence angles and with different tilting angles, as shown in Fig. 3.16. The energy streamlines are traces of the Poynting vector trajectories for plane waves with $\lambda = 20\ \mu$m incident from vacuum onto the film. All the streamlines are assumed to originate at $x = 0$ and $z = -0.5d_2$. Due to the low reflection at the interfaces between vacuum and CNT film, the streamlines are nearly straight in each region. As shown in Fig. 9(a) for VACNT, the streamlines are symmetric with respect to $x = 0$. The upper curves are for $\theta_i > 0°$ and the lower curves are for $\theta_i < 0°$. As seen in Fig. 3.16(a), the energy streamlines show slight negative bending, but largely travel along the optical axis of the CNT array. In the exiting medium, $z > d_2$, the streamlines or rays continue to spread away from the "source." Essentially, from $z = 0$ to $z = d_2$, the beam is collimated and the shape of the incoming rays from the incident interface to the outgoing interface is conserved. In Figs. 3.16(b) and (c), with CNT tilting angles of $\beta = 30°$ and $\beta = 60°$, respectively, the self-collimation characteristic through the thin film is also conserved. The rays inside the

58

CNT always travel along its optical axis. However, at $\beta = 70°$, as shown in Fig. 3.16(d), self-collimation breaks down at negative incident angles, as evident from the bottom three streamlines.
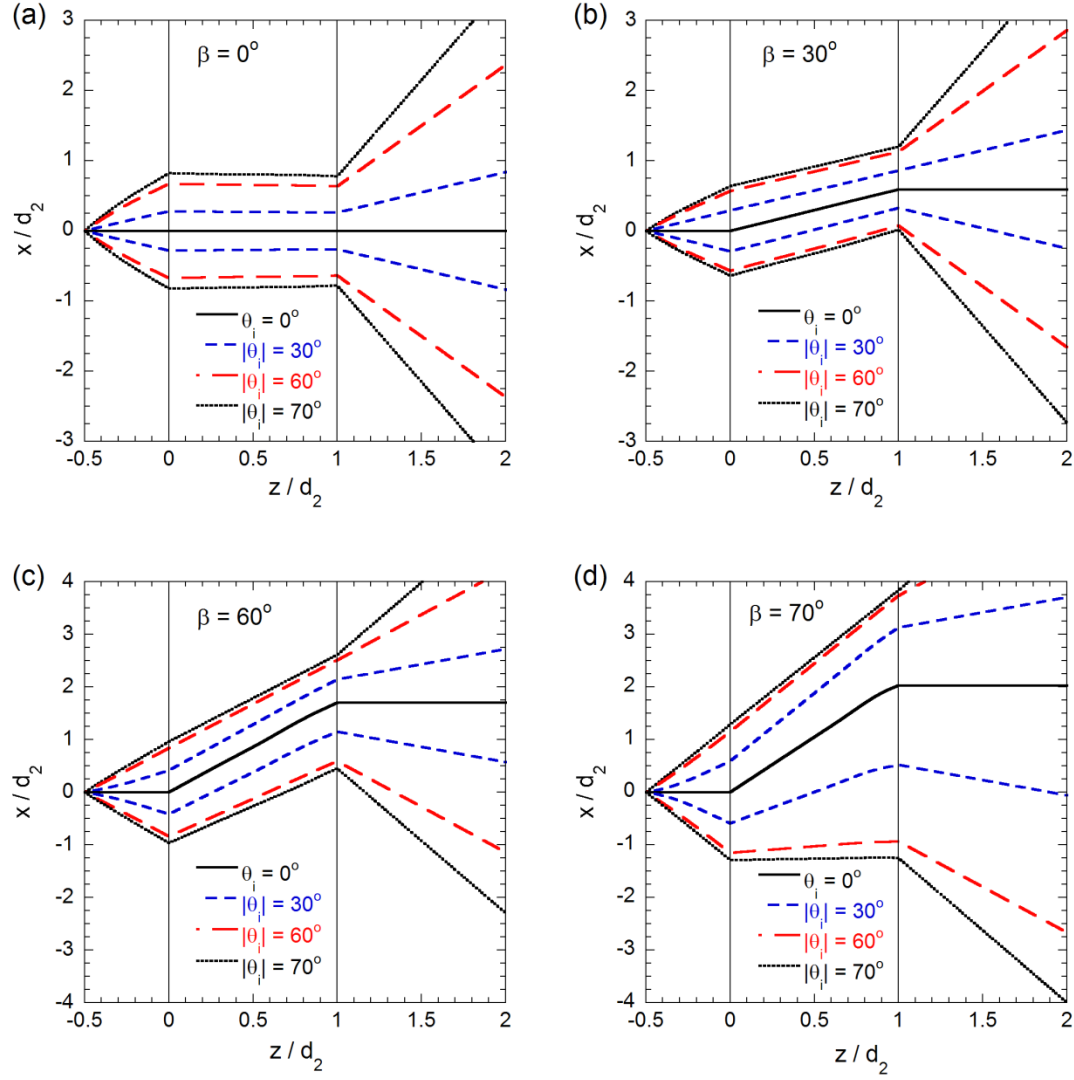
Figure 3.16 Energy streamlines for various incidence angles at $\lambda = 20\ \mu$m for CNT thin films of $d = 10\ \mu$m with different tilting angles: (a) $\beta = 0°$ (VACNT), (b) $\beta = 30°$, (c) $\beta = 60°$, and (d) $\beta = 70°$. Streamlines above $\theta_i = 0$ are for positive θ_i, and below $\theta_i = 0$ are for negative θ_i.

3.4 Conclusion

The radiative properties of multi-walled VACNT coatings are investigated by assuming that the nanotubes exhibit similar dielectric properties as that of coordinate-transformed graphite. Due to the refractive index matching in the near- to mid-infrared, surface reflection is low and the material becomes a good absorber. Two broad hyperbolic dispersion bands in the far-infrared region are also predicted based on the effective dielectric tensor. Due to the interband transition at $\lambda \approx 100~\mu$m and free electron effect in the far-infrared, the reflectance is high, resulting in a rather low absorption at $\lambda > 100~\mu$m. Generally, low packing density and high degree of alignment can reduce surface reflection. Also, the Brewster angle is best defined only in the near- and far-infrared, as matching with the principal angle is qualified. For thin CNT films, absorptance in the near- and mid-infrared is deteriorated due to high penetration depth and reflection at the CNT-substrate interface.

With VACNT having hyperbolic dispersion, the energy refraction angle is negative and the Poynting vector tends to align with the optical axis of the CNT array, whether vertically aligned or tilted. Loss-enhanced transmission and collimation in CNT arrays are demonstrated in the far-infrared from two hyperbolic regions. Improving the alignment factor can further promote this mechanism. For tilted CNT arrays, surface reflectance is reduced and the penetration depth is increased when the incidence angle is nearly coincident with the tilting angle, especially at $\lambda = 20~\mu$m. The refraction and self-collimation of light through the tilted CNT array is strong for most tilting angles. For heavily tilted CNT, however, self-collimation may break down when radiation is incident at negative angles.

CHAPTER 4

NEGATIVE REFRACTION IN MULTILAYERS

The unique radiative properties of multilayers are discussed in this Chapter, namely the negative angle of refraction of waves from visible to infrared wavelengths. Typically, multilayers contain alternating layers of metal and dielectric to achieve the hyperbolic dispersion needed for negative index. In Section 4.1, graphene is introduced and the properties are portrayed to propose graphene-dielectric multilayers. The far-field radiative properties of graphene-dielectric multilayers are shown in the following section. By tuning the biasing of graphene, such multilayered thin film can achieve switchable positive and negative angle refraction. To contrast the capabilities of graphene-dielectric multilayers are metal- or semiconductor-dielectric multilayers, as studied in Section 4.3. Here, the energy streamlines and radiative properties are compared for three cases to elucidate some parameters for appropriate use of effective medium theory (EMT). The next section queries the far-field radiative properties of multilayers with graded layer thicknesses. Since EMT does not have a metric to account for non-periodic multilayers, some new constraints and assumptions are made. The last section concludes this Chapter on multilayers.

4.1 Properties of Graphene and Multilayers

The dielectric function of graphene determined from Eq. (2.7) is shown in Figure 4.1. Three representative chemical potential (μ) values are established for study in the remainder of this Chapter. The salient feature of graphene is its tunable negative real component of permittivity in the far-infrared, as shown in Fig. 4.1(a). The interband

transition for the lowest chemical potential (0.1 eV) is centered around $\omega = 2\mu$, which corresponds to $\lambda = 6.2\ \mu\text{m}$. For higher chemical potentials, the Drude conductivity (intraband) dominates from the mid-infrared. Also notable is the imaginary component of the permittivity shown in Fig. 4.1(b). Beside the increasing loss due to the Drude-like absorption, increasing chemical potential reduces loss in the mid-infrared regime.
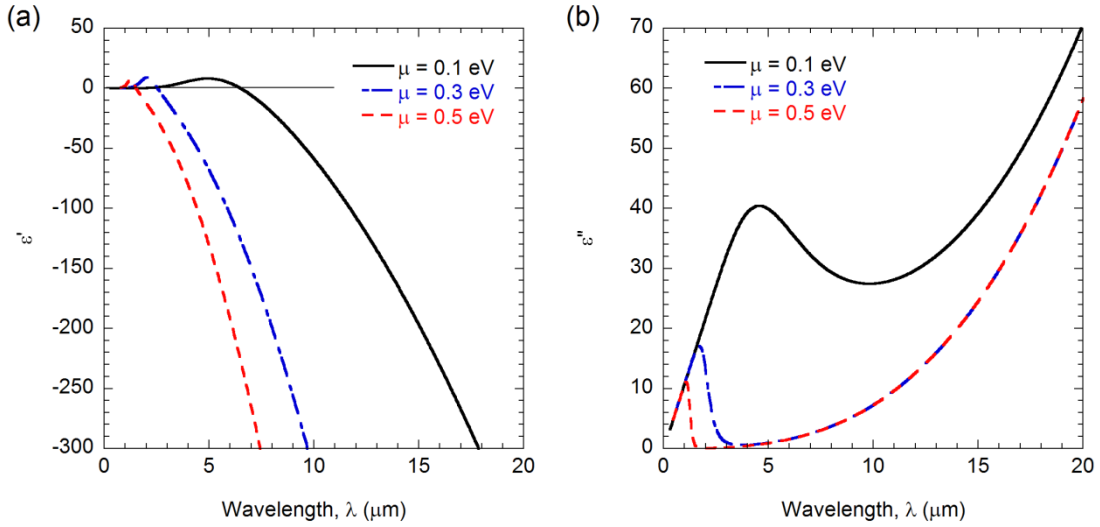
Figure 4.1 (a) Real and (b) imaginary components of the relative sheet permittivity of graphene at chemical potential levels of $\mu = 0.1\ \text{eV}$, $0.3\ \text{eV}$, and $0.5\ \text{eV}$.

Visual representation of the graphene-dielectric multilayer is tied to Fig. 2.3, where d corresponds to dielectric layer and m to graphene in this case. Since graphene is much thinner than feasible layers of dielectrics, the period size (Λ) is nearly the same as the dielectric spacer thickness. Also, the filling fraction is nearly zero. Due to the large magnitude of graphene relative to typical positive index dielectrics, the EMT equations from Eq. (2.10) for traditional multilayers are modified to,

$$\varepsilon_O = f\varepsilon_g + (1-f)\varepsilon_{d,O} \tag{4.1a}$$

$$\varepsilon_E = \varepsilon_{d,E} \tag{4.1b}$$

62

The ordinary direction permittivity (ε_O) of the graphene-dielectric multilayers calculated using Eq. (4.1) is shown in Figure 4.2 for two different dielectric spacer thicknesses. The static, lossless, and isotropic permittivity for the dielectric spacer is $\varepsilon_d = 6.0$. The dielectric spacer thickness is set between $d_d = 10$ nm and 50 nm.
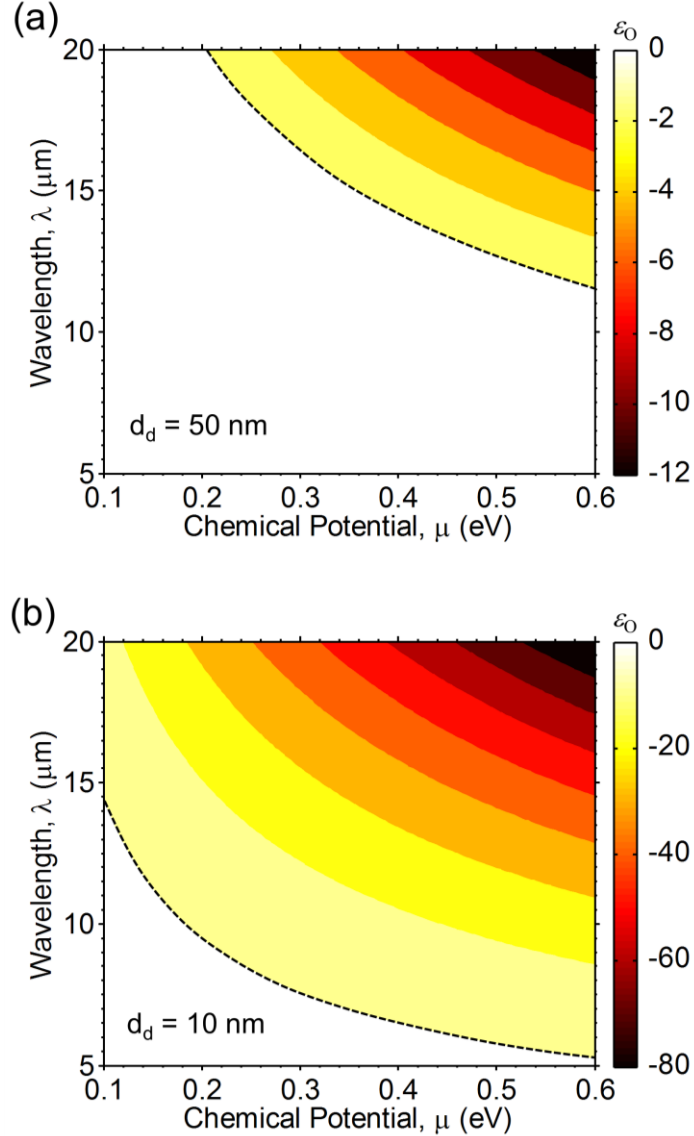
Figure 4.2   Contour plots of the graphene-dielectric multilayers' relative permittivity determined by EMT. The dielectric spacer dimensions of (a) $d_d = 50$ nm and (b) 10 nm are shown. The dashed line marks where $\varepsilon_O = 0$. Positive ε_O are not shaded in the lower-left region and rise monotonically toward $\varepsilon_d = 6.0$.

Fig. 4.2(a) shows with 50 nm-thick dielectric spacers, ε_O is negative when $\lambda > 11\,\mu$m. As the chemical potential of graphene decreases, the cutoff wavelength for negative ε_O becomes higher, as indicated by the dashed line. This trend is shifted toward the lower-left when the dielectric spacer thickness is reduced to 10 nm, as seen in Fig. 4.2(b). Since the filling ratio is increased by five-fold, the effect from ε_g becomes stronger and negative ε_O exists at wavelengths down to $\lambda = 5\,\mu$m. The magnitude of ε_O is also increased approximately five-fold for the settings corresponding to the upper-right of the contoured plot. Any higher chemical potential in graphene may be limited by voltage biasing [52,61,63].

4.2 Tunable Refraction in Graphene-Dielectric Multilayers

In this section, we present an alternative perspective of the graphene-dielectric multilayers to better accomplish the sought-after optical properties of hyperbolic metamaterials. By introducing the side-incidence perspective, positive and negative refraction can be actively controlled. The traditional perspective of the graphene-dielectric multilayers (top-incidence) is illustrated by the conical beam, and the proposed alternative perspective (side-incidence) is shown by the rhombic beam in Figure 4.3(a). The unique advantage of the side-incidence perspective is the tunability between positive and negative refraction, enabled by graphene. Since all structures have characteristic dimensions that are magnitudes smaller than the wavelengths of interest, the photonic crystal medium appears homogeneous and anisotropic. Exact multilayer electromagnetic wave theory is used to validate the effective medium assumption for the top-incidence case only. The associated nomenclatures of both orientations are denoted in Fig. 4.3(b).
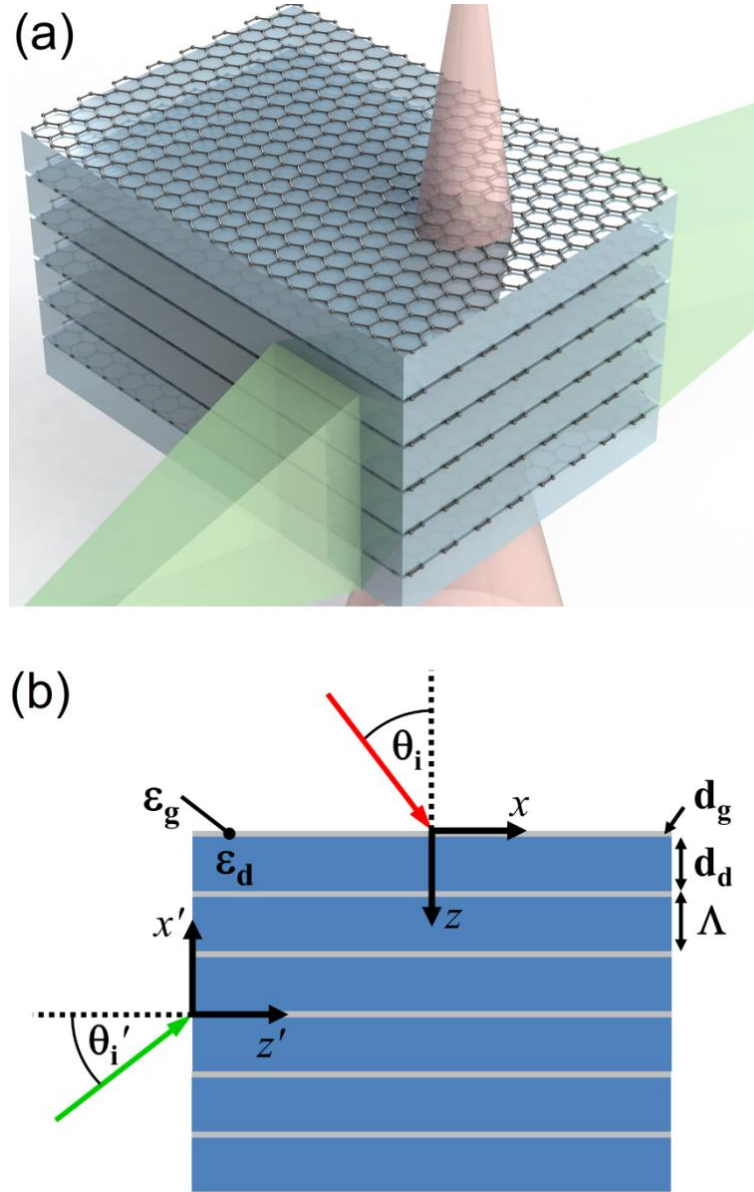
Figure 4.3 Illustration of graphene-dielectric multilayers showing (a) the interactions with light beams in perpendicular directions (top-incidence versus side-incidence perspectives), and (b) the nomenclature of associated dimensions and permittivities of the graphene sheets and dielectric spacers. Coordinates and nomenclature corresponding to side-incidence are denoted by the prime.

To illustrate the possible negative index in the multilayers from the top-incidence perspective, the energy streamlines made by tracing the Poynting vectors are shown in Figure 4.4(a). The number of periods (N) is 40, and the dielectric spacer thickness is 50

nm, which gives the total slab thickness of $d = 2.01\ \mu\text{m}$. The streamlines determined by

TMM (lines) and EMT (points) agree reasonably well under the prescribed parameters.

For shorter wavelengths or thicker dielectric spacers, EMT breaks down, according to

$\left|k_z d_\text{d}\right| << \pi$ or $2d_\text{d} << \lambda$ [62,142,161]. Despite having negative ε_O at the prescribed

wavelength and chemical potential, no negative angle light bending is observed at any

incidence angle (θ_i). The refraction angle can be approximated as,

$k_z'^2 \approx k_0^2 \varepsilon_\text{O}'' - k_x^2 \varepsilon_\text{O}'' / \varepsilon_\text{E}$, so for a positive imaginary term (ε_O'') follows an ellipse-like

dispersion. As it turns out, by evaluating the anisotropic dielectric function in Eq. (4.1)

for Eq. (2.11), the hyperbolic dispersion is of Type II. The blocking of propagating waves

is demonstrated in Fig. 4.4(b), where shrinking the period size and adding the number of

layers increases the influence of the negative-permittivity graphene. This results in the

loss of transmission through the multilayers containing many graphene sheets.
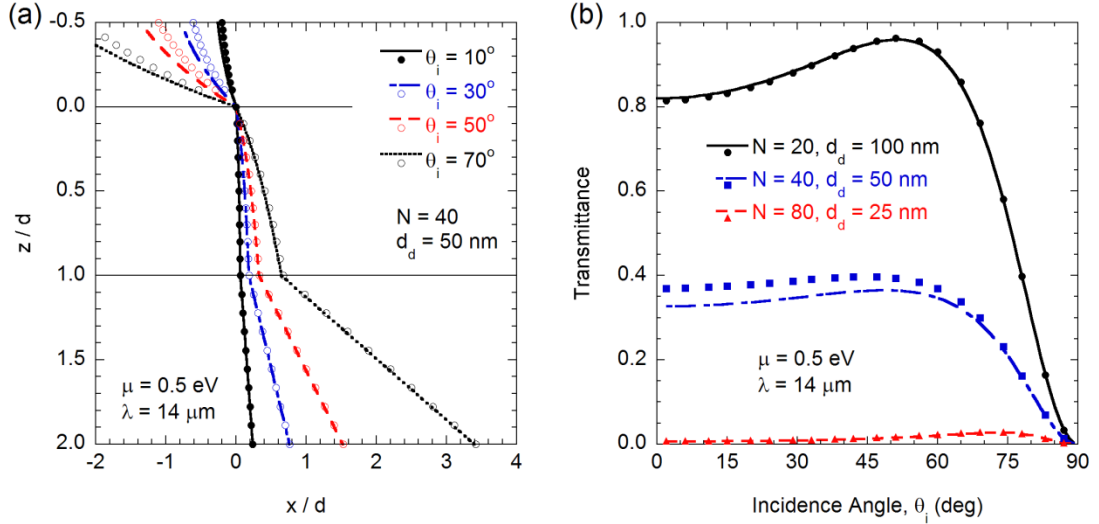
Figure 4.4 The radiative properties determined by transfer matrix method (TMM, lines) versus EMT (points) of the top-incidence multilayers. (a) The energy streamlines in multilayer thin film with slab thickness of $d = 2.01\ \mu\text{m}$. (b) Transmittance spectra of the multilayer thin film with different number of layer periods and dielectric spacer sizes.

The side-incidence perspective in effect switches k_z for $k_{x'}$, and k_x for $k_{z'}$ in Eq. (2.11). This change in the dispersion relation supports negative angle refraction, while the metamaterial is still defined as Type II hyperbolic. Under this circumstance, all incident waves on the multilayers result in Poynting vectors directed in the negative x' direction [82,142]. The energy streamlines of the side-incidence multilayers are illustrated in Figure 4.5 for various cases. The slab thickness d in the direction of z' is set to exactly $2.0 \ \mu m$, and N is sufficiently large to accommodate millimeters-wide beam sizes in the x' direction. In this framework, the EMT formulation of a uniaxial slab is suitable since the wavelength versus period sizing inequality is satisfied. The interaction with TM waves in the y'-z' plane of incidence (magnetic field is in the x' direction) is isotropic and high loss, according to $k_{x'}^2 + k_{z'}^2 = \varepsilon_O k_0^2$, and therefore not considered.

Figures 4.5(a), (c), and (e) show the shift in dispersion type as the chemical potential is increased from $\mu = 0.3 \ \text{eV}$, $0.413 \ \text{eV}$, to $0.5 \ \text{eV}$, respectively. In these cases, the dielectric spacer thickness ($d_d = 50 \ \text{nm}$) and wavelength ($\lambda = 14 \ \mu m$) are held constant. For $\mu = 0.3 \ \text{eV}$ corresponding to positive ε_O, ordinary positive refraction is seen. At the dashed line indicated in Fig. 4.2(a), where the real part of ε_O is zero ($\varepsilon_O' = 0$), setting $\mu = 0.413 \ \text{eV}$ makes the multilayers behave as a self-collimator. While this mode may promise fiber optic-like properties, it is extremely narrowband and suffers from high loss, which will be elaborated later. At $\mu = 0.5 \ \text{eV}$, where $\varepsilon_O = -1.28 + 0.13i$, the energy streamlines begin to divert in the negative x' direction inside the medium. Some interference effects or undulations in the streamlines are observed, which may present some difficulty for applications in focusing and imaging.
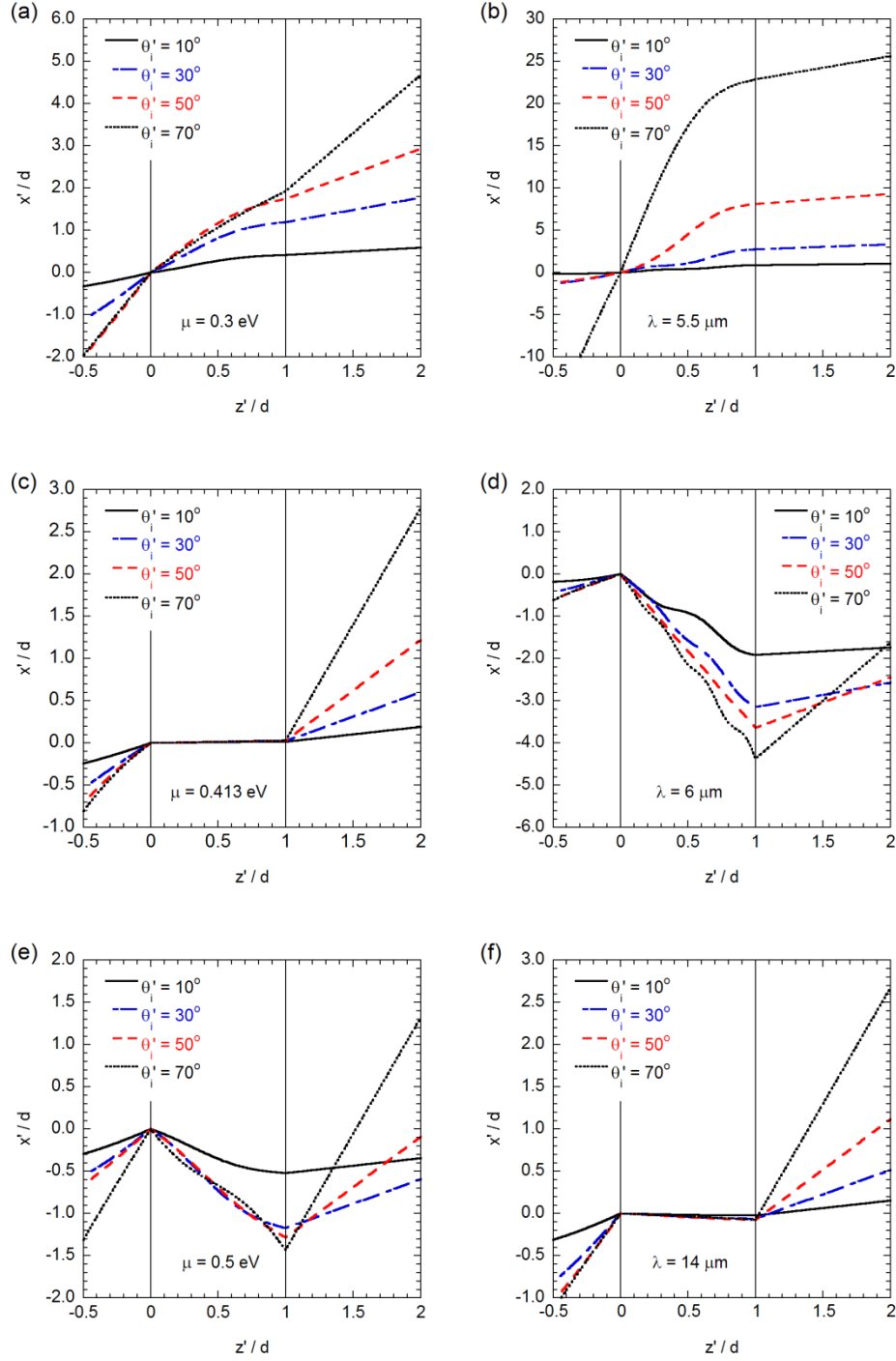
Figure 4.5 Energy streamlines in graphene-dielectric multilayers from side-incidence perspective. Corresponding to $d_d = 50$ nm and $\lambda = 14\ \mu$m: (a), (c), and (e) exhibit positive index, epsilon-near-zero, and negative index dispersions, respectively, as the graphene chemical potential is increased. For $d_d = 10$ nm and $\mu = 0.5$ eV: (b), (d), and (f) demonstrate large lateral shifts, negative index, and self-collimation, respectively, for increasing wavelength. The slab thickness (d) is set to 2.0 μm.

The dielectric spacer size of $d_\mathrm{d} = 10$ nm is used to illustrate the effect of largely

negative ε_O as the wavelength is increased. Figures 4.5(b), (d), and (f) show streamlines

at $\lambda = 5.5\ \mu\mathrm{m}$, $6\ \mu\mathrm{m}$, and $14\ \mu\mathrm{m}$, respectively, while holding $\mu = 0.5$ eV. At

$\lambda = 5.5\ \mu\mathrm{m}$, the positive refraction is similar to that shown in Fig. 4.5(a), but with greater

lateral shift. This is due to the small and positive real component in ε_O, thus amplifying

the changes in the z'-component on the x'-component. In the case when $\lambda = 6\ \mu\mathrm{m}$, the

streamlines present themselves similarly to those in Fig. 4.5(e) since ε_O is also negative.

When taking the wavelength to $\lambda = 14\ \mu\mathrm{m}$, where $\varepsilon_\mathrm{O} = -29.3 + 0.65i$, the large

magnitude in ε_O makes $k_{x'}$ nearly insensitive to $k_{z'}$. This results in a self-collimation

effect in the multilayer medium that is also broadband in longer mid-infrared

wavelengths [157]. Unlike the collimation seen in Fig. 4.5(c), radiative transmission is

sustained, as will be elaborated next.

The transmittance profiles with incidence angle for each case examined in Fig. 4

are shown in Figure 4.6. The thin film is highly transmitting in both positive and negative

refraction modes, as seen in Fig. 4.5(a). However, transmittance is almost totally lost at

oblique angles when $\mu = 0.413$ eV. This epsilon-near-zero (ENZ) mode suffers from

short penetration depths, approximated to be $\delta \approx \sqrt{\varepsilon_\mathrm{O}''} \big/ \left(2k_{x'} \sqrt{\varepsilon_\mathrm{E}} \right)$. Contrary to intuition,

the penetration depth could be larger at ENZ by using a lossy dielectric that increases ε_O''

[157]. In Fig. 4.6(b), the loss in transmittance accompanied by large lateral shift for

incidence angles greater than approximately 60° is due to the near-ENZ mode when

$\lambda = 5.5\ \mu\mathrm{m}$. Here, the anisotropic medium critical angle is defined by $\theta_\mathrm{c}' = \sin^{-1}\left(\sqrt{\varepsilon_\mathrm{O}} \right)$,

which gives $\theta'_c = 60.3°$ [3,157]. The other two wavelengths far from ENZ demonstrate relatively good transmittance at oblique angles, with some interference patterns due to internal film reflections. Having a dielectric spacer defined by a real material dielectric function could allow highly penetrating radiation even toward the far-infrared wavelength regime.
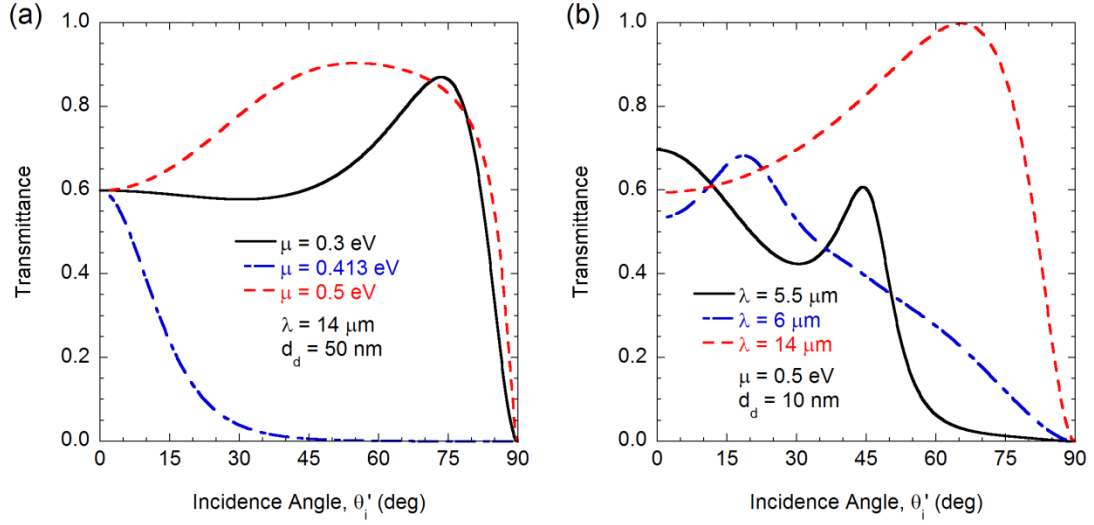
Figure 4.6 Transmittance spectra of 2.0 μm-thick side-incidence graphene multilayer thin films corresponding to changing (a) graphene chemical potential and (b) wavelength.

The dielectric spacer defined in this study is similar to hexagonal boron nitride (hBN), a typical encapsulating material for voltage-gated graphene devices [72,121,129,162]. hBN has good large-area lattice matching to graphene without compromising the electron mobility of the latter, and can be fabricated in thin layers of a few nanometers [72,163]. The real dielectric function of hBN is anisotropic, and can be statically approximated to $\varepsilon_O = 6.85$ and $\varepsilon_E = 5.06$, which turns out average to $\varepsilon_d = 6.0$ [164]. In addition, the dielectric constant of hBN contains phonon absorption bands that could reduce transmission. The two narrowband phonon resonances are centered at

$\lambda = 7 \, \mu\text{m}$ and $13 \, \mu\text{m}$ [164]. The wavelengths should be far from these phonon absorption bands. In order to fabricate the graphene-dielectric multilayers used in the side-incidence manner, further development of growth techniques that ensures multiple uniform and large area interface contacts between hBN and graphene is needed.

4.3 Energy Streamlines in Semiconductor Multilayers

The advantage of graphene over deposited metal layers is its infinitesimally thin coverage between dielectrics while still offering high conductances. To understand the difficulties in traditional metal-dielectric multilayers, the energy streamlines (ESL) and radiative properties are studied. The validity of EMT is understood by comparing these properties to those found by TMM. Three metal- or semiconductor-dielectric multilayers are presented, with their dielectric function and Drude model parameters listed in Table 4.1. Ref. [83] is a hyperbolic multilayer containing silver and rutile (TiO$_2$), which was reported to demonstrate negative refraction in the UV to visible wavelengths. The fabricated structure consisted of three MDMDM units, with each layer having approximately $d_{d,m} = 30 \, \text{nm}$ in thickness. Equivalently, $N = 8$ according to the multilayer geometry shown in Fig. 2.3. Ref. [165] contains semiconductor-dielectric layers, which the former material is achieved by doping zinc oxide with aluminum (AZO-ZnO). The fabricated thin film was reported to have 16 alternating layers ($N = 8$), each 60 nm thick. The doping concentration of the AZO layers is $4.3 \times 10^{20} \, \text{cm}^{-3}$. The semiconductor substitute for metal offers tunability by means of doping, and has less loss while offering negative permittivity. Furthermore, fabrication of doped semiconductors is more integrated, and does not require very thin layer deposition. Ref. [159] offers another semiconductor-dielectric multilayers, which consist of aluminum or gallium-doped

71

indium arsenide ($Al_{0.48}In_{0.52}As$-$In_{0.53}Ga_{0.47}As$). The doping concentration for most cases was set to 7.5×10^{18} cm^{-3}. Here, the layers are 80 nm thick, and all alternating layers added to 8.1 μm ($N \approx 50$).

Table 4.1 Dielectric function and Drude model parameters of hyperbolic multilayers.

	ε_d	ε_∞	ω_p	γ
Ref. [83]	$\perp$: 6.3–9.1 $\parallel$: 7.8–11.5	1.0	1.39×10^{16} rad/s	2.73×10^{13} rad/s
Ref. [165]	4.0	4.0	1.04×10^{15} rad/s	1.85×10^{14} rad/s
Ref. [159]	10.23	12.15	2.14×10^{14} rad/s	1.0×10^{13} rad/s

The wavelength regions at which the multilayers transition from Type I to Type II hyperbolic dispersion is distinct. Figure 4.7 plots the ordinary and extraordinary components of the dielectric function of the three multilayers. The dielectric functions determined by EMT all have filling ratios of $f = 0.5$. The Ag-TiO_2 multilayers, shown in Fig. 4.7(a) makes the transition at $\lambda = 0.44$ μm. The Type I hyperbolic regime is highlighted in blue, and Type II in yellow. The dielectric function of AZO-ZnO multilayers is shown in Fig. 4.7(b). The transition between Type I and II is smeared near $\lambda = 2.5$ μm, so that a narrowband region is double positive permittivity. Unlike the previous case, the hyperbolic regions hold relatively small ε_E'. The dielectric function of the indium arsenide multilayers is shown in Fig. 4.7(c). Both semiconductor multilayers have hyperbolic dispersion in the near- and mid-infrared wavelengths.
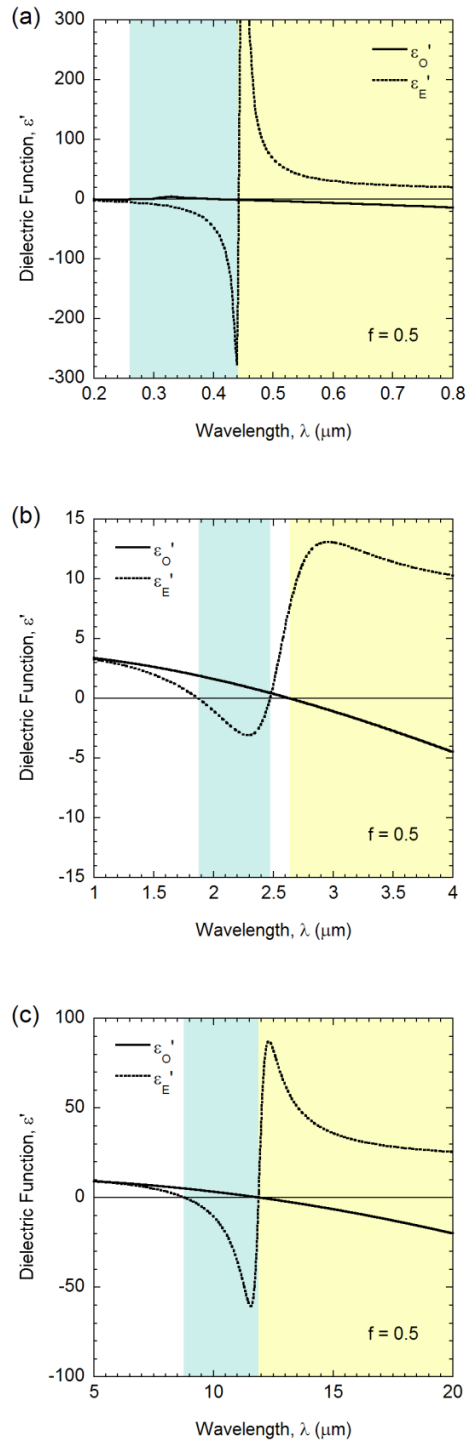
Figure 4.7 Dielectric functions of the metal- or semiconductor-dielectric multilayers: (a) Silver-Rutile (Ag-TiO$_2$), (b) Aluminum-Zinc Oxide (AZO-ZnO), and (c) Aluminum or Gallium-Indium Arsenide (AlInAs-InGaAs). The blue shaded region corresponds to $\varepsilon'_O > 0$ and $\varepsilon'_E < 0$, and yellow to $\varepsilon'_O < 0$ and $\varepsilon'_E > 0$.

The energy streamlines and transmittance of the aforementioned multilayers are shown in Figure 4.8. The TM wave ESLs all have incidence angles at $\theta_i = 40°$, which correspond to the simulated beam field maps of Ref. [165]. The standard case is given alongside a case where the thickness of the layers is either increased or decreased. In Fig. 4.8(a), the standard case for Ag-TiO$_2$ multilayers is $d_{d,m} = 30$ nm. The wavelength used concerning Type I hyperbolic dispersion is $\lambda = 400$ nm, which is more than an order magnitude spatially larger than the thickness of constituent layers. However, the jagged ESL determined by TMM is remarkably different from that by EMT (dotted). Upon closer look, the dielectric layers swing the ESL toward the positive x direction, and the metal layers toward negative x. Closer to the exiting medium surface ($z/d = 1^-$), the ESL becomes wavy within each layer. This signifies evanescent wave coupling in the thin dielectric media between the near-field coupled plasmonic metal surfaces. The layer thickness is then reduced to 12 nm, which gives ESL fitting better to that determined by EMT. The transmittance profile in terms of the incidence angle, as shown in Fig. 4.8(b), also show significant differences between EMT and both cases calculated using TMM. The absorptance in the EMT homogenous medium accounts for most of the loss in transmittance. In the TMM cases, reflectance becomes significant, as implied by the slope of the ESL in medium 1.

The ESL and transmittance of AZO-ZnO multilayers are shown in Figs. 4.8(c) and (d), respectively. Despite having thicker layers and evident jaggedness, the ESLs hold very well to that estimated by EMT. In the case when $d_{d,m} = 120$ nm, only 4 periods are contained the thin film. The zig-zag ESLs do not significantly deviate in the lateral direction. Moreover, the transmittance profile is nearly unchanged between EMT

and TMM of any layer thickness. Figs. 4.8(e) and (f) are for the indium arsenide multilayers, which show that for very thick layers ($d_{\mathrm{d,m}} = 500$ nm, $N = 8$), large lateral deviations occur in the ESL and transmittance is reduced.

The anomaly is in the AZO-ZnO multilayers, which having few periods and very thick layers, do not have ESLs that deviate heavily from the homogeneous (EMT) case. To better understand the deviations, some definitions and assumptions need to be established or revisited. In general, the size of either metal or dielectric layer must be smaller than the characteristic wavelength. For all these cases, the layer thickness is at least 10 times smaller than the wavelength. Certainly, the greater the ratio, the better the agreement. The exact formulation for the thickness limit of EMT is given by the Bloch wave theory [86,144,166]. The existence of propagating Bloch waves is given by the inequality,

$$k_z d_{\mathrm{d,m}} << \pi \tag{4.2}$$

where k_z and d are defined in each homogeneous medium. For example, this condition applied to EMT, where k_z employs the permittivity of the multilayered medium, is 0.4.

This is a magnitude smaller than π. However, in the dielectric layer, $k_z = \sqrt{k_0^2 \varepsilon_{\mathrm{d}} - k_x^2}$ and results in a larger real component. The condition in Eq. (4.2) is 1.4 for 30 nm-thick layers, and 0.6 for 12 nm-thick layers. The reason why 120 nm-thick layers in AZO-ZnO remains true to EMT is because the condition is small ($k_z d_{\mathrm{d,m}} = 0.7$). The 500 nm-thick layers shown in Fig. 4.8(e) comes to $k_z d_{\mathrm{d,m}} = 1.04$. Therefore, what this may suggest is for the inequality to be modified to $k_z d_{\mathrm{d,m}} < 1$ to have reasonable agreement between ESLs determined by EMT and TMM.
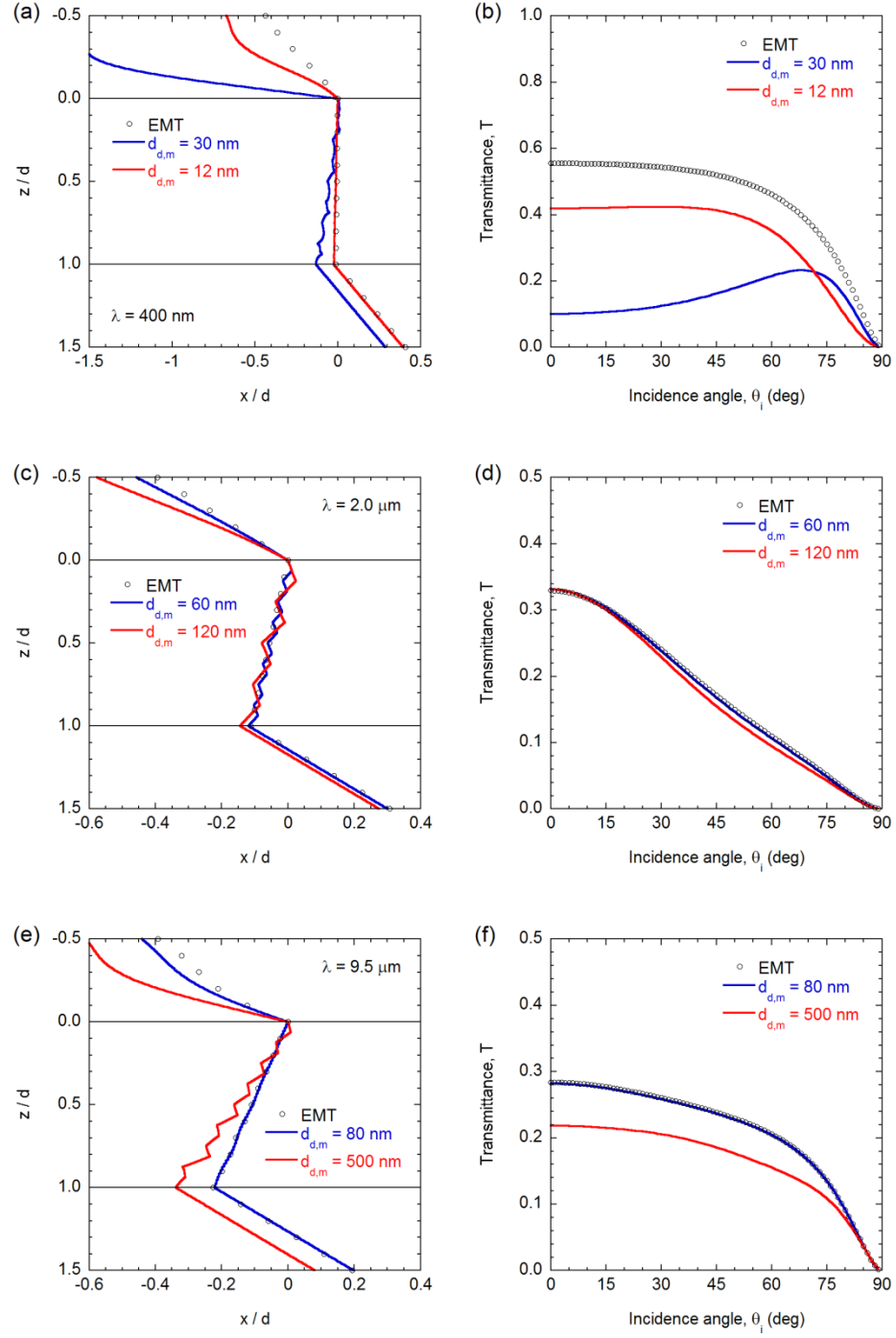
Figure 4.8 Energy streamlines at incidence angle of $\theta_1 = 40°$, and angular transmittance profiles: (a) The energy streamlines and (b) transmittance of Al-TiO$_2$ multilayer thin film of $d = 480$ nm thickness; (c) and (d) of AZO-ZnO multilayer thin film of $d = 960$ nm thickness, respectively; (e) and (f) of AlInAs-InGaAs multilayer thin film of $d = 8$ μm thickness, respectively.

The left column of Figure 4.9 illustrates Bloch waves in the multilayered media. The squared electric field magnitudes are normalized to that of the incidence field. For the Ag-TiO$_2$ multilayers, shown in Fig. 4.9(a), the waves formulated by EMT are continuous and periodic. The true Bloch waves are determined by TMM, which show frequency envelopes due to two wave translation operators. The dual-mode sinusoid is clear for the case $d_{d,m} = 12$ nm, but not in the other one. No clear frequencies are observed when the layer thickness becomes very large. Fig. 4.9(c) offers a counter indication, in which despite having thick layers, the periodic wave shape is conserved throughout the thin film. The discontinuities in the Bloch waves are due to the lossless dielectrics used in modeling the multilayers. This is also observed in Fig. 4.9(e), in which for the thick layers, the periodicity is not as clean. Toward the bottom of the thin film, the Bloch waves begin to break down, leading to mismatching with the waves determined by EMT. The breakdown of Bloch waves implies that the imaginary component of each constituent layers' permittivities should be reduced in negative index materials.

The illustrate at which layer or period the breakdown of Bloch waves occurs, the penetration depths are studied, as shown in Figs. 4.9(b), (d), and (f). Generally, the penetration depth should over estimate that by EMT, because the dielectric layers at least in the first few periods are nearly lossless. For Ag-TiO$_2$ multilayers, the penetration depth profile for 30 nm-thick layers demonstrates a step-like reduction with incidence angle. Unlike those shown in Fig. 4.9(d), the steps are smoothened because the dielectric is modeled as having a small loss. In both semiconductor-dielectric multilayers, the penetration depths at very oblique angles match that of EMT. This signifies that despite being more reflecting at the surface, the ESLs match well at these angles. Therefore, the

77
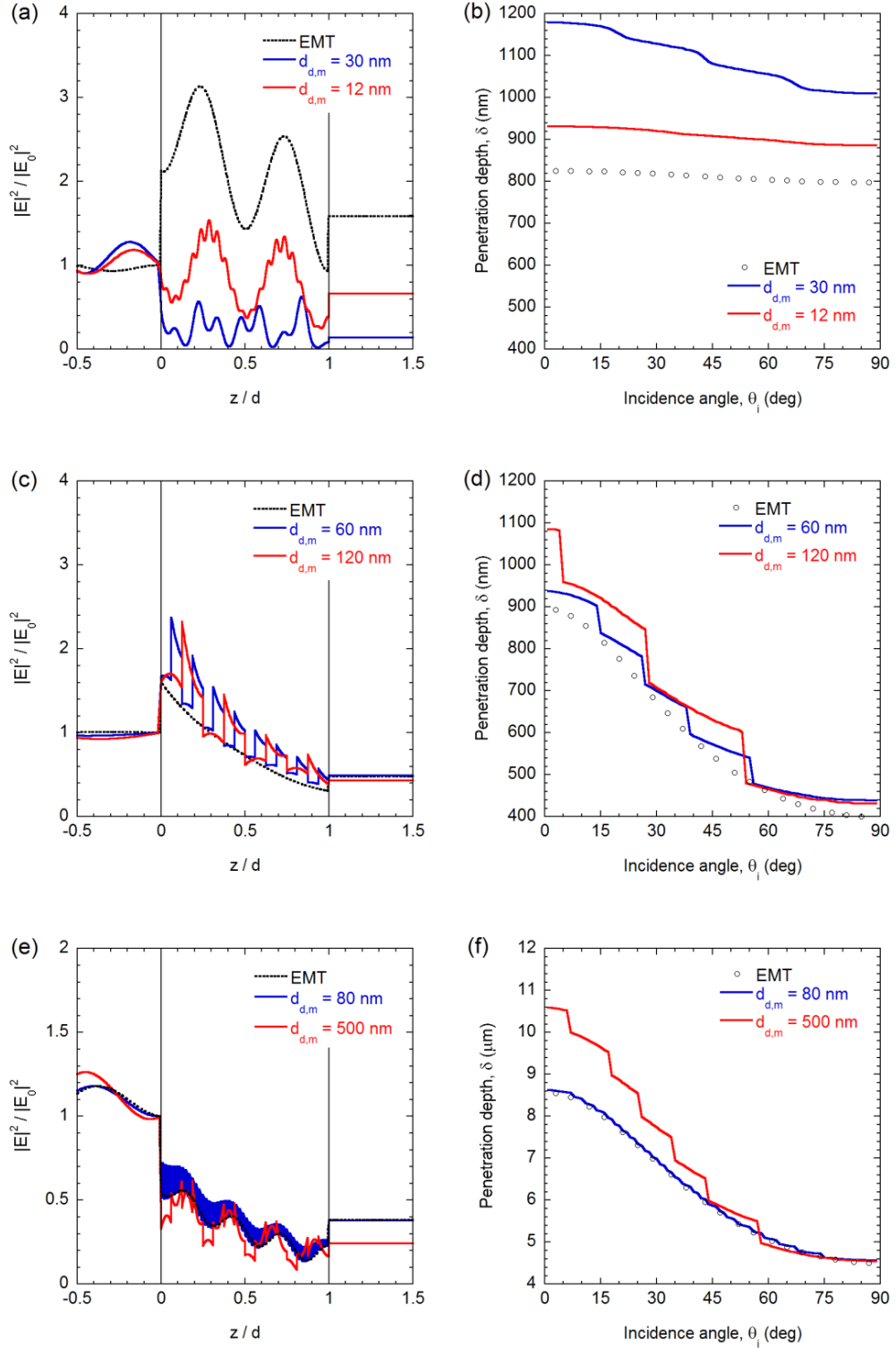
Figure 4.9 Squared electric field magnitudes normalized to incidence surface for (a) Al-TiO$_2$, (c) AZO-ZnO, and (e) AlInAs-InGaAs. The penetration depths varying with the incidence angle for (b) Al-TiO$_2$, (d) AZO-ZnO, and (f) AlInAs-InGaAs. The wavelengths and thin film thicknesses correspond to those in Fig. 4.8.

validity of EMT in constructing ESLs relies on not only the reducing the real component of the dielectric permittivity, but also smaller loss in metal, semiconductor, and dielectric layers as well.

4.4 Effect of Non-Periodic Multilayers

A shortcoming of the 1D multilayer EMT equation presented in Eq. (2.10) is its singular dependency on the filling ratio. For example, it does not account for sizes of individual periods. Therefore, one can craft non-periodic or gradient multilayers that still demonstrate the same filling ratio. Figure. 4.10 illustrates two cases: Within each period, the metal to dielectric ratio is unity. The next period is enlarged, as shown in Fig. 4.10(a),
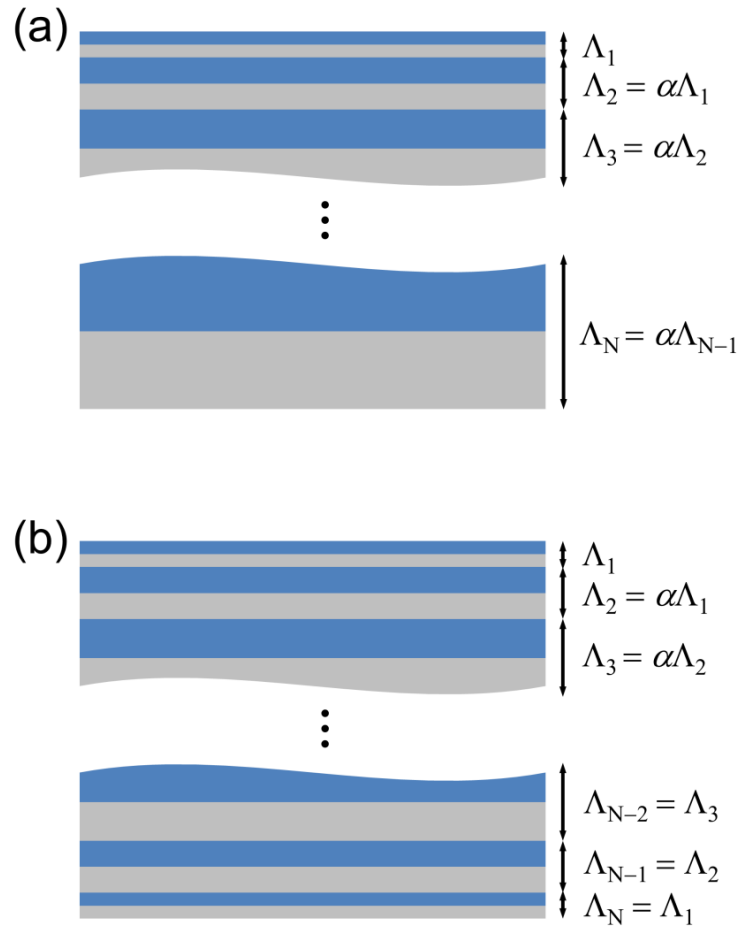
Figure 4.10 Schematic and nomenclature of: (a) One-way gradient multilayers, and (b) Symmetrically-graded multilayers. The period numbers correspond to that from Fig. 2.3.

by a factor of α. This gradient factor is constant throughout the one-way graded multilayer. Fig. 4.10(b) is a symmetrically-graded multilayer, in which the middle period is either the largest or smallest, depending on how α is defined.

In the one-way graded multilayers, the ESLs abide to that estimated by EMT fairly well, as shown in Figure 4.11(a). The material definitions are based on those in Ref. [165]. The thickest layer for either configuration is 115 nm, which is over 17 times smaller than the characteristic wavelength ($\lambda = 2\ \mu$m). However, Fig. 4.11(b) tells of a different story, by understanding the differences between reflectance and transmittance of EMT versus graded multilayers. When the gradient factor is unity, one expects to see near-zero reflectance and transmittance differences. This is not the case since the difference in reflectance is smallest toward large gradient factors. Therefore, EMT presumes near-infinitesimally thin layers, especially at the thin film incidence surface.
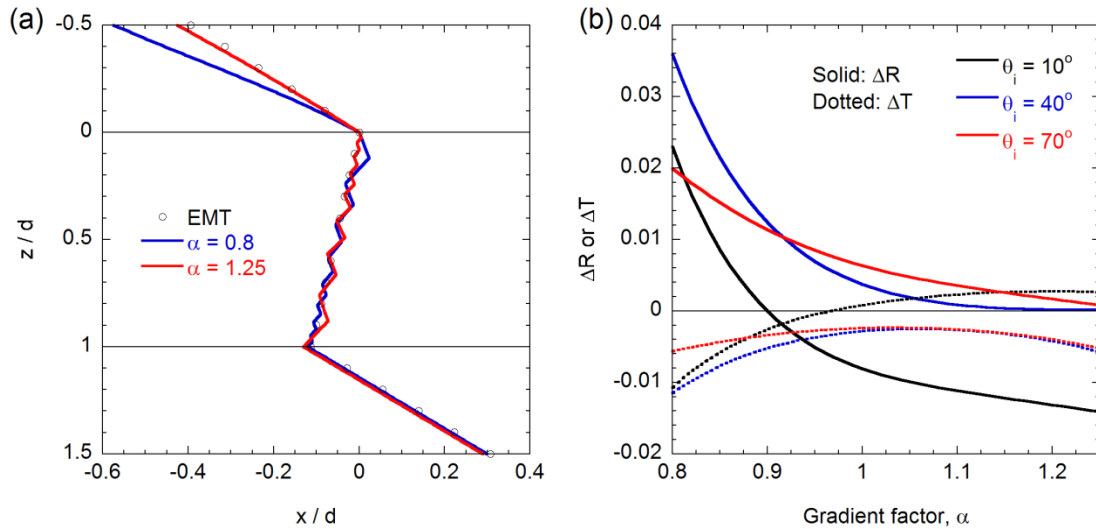
Figure 4.11 (a) Energy streamlines at incidence angle $\theta_i = 40°$, and (b) the differences in reflectance or transmittance of one-way gradient multilayers for varying gradient factors.

For the case when $\theta_i = 10°$, the gradient factor that results in least difference in reflectance is near $\alpha = 0.9$ and then becomes anti-reflecting. This is most likely due to the thick top dielectric layer and the lack of internal reflection at shallow incidence angles. If the top layer is metal or semiconductor, the reduction of reflectance is not observed for increasing gradient factor (not shown).

Figure 4.12 shows the case where the gradient periods are symmetric across the center of the thin film. The ESLs in Fig. 4.12(a) makes the changing layer thicknesses evident, where the thickest layers deviate the most from the ESL estimated by EMT. Overall, the agreement with EMT is very good as the ESLs are collinear in the outgoing medium. From Fig. 4.12(b), the difference in reflectance and transmittance is nearly the same as those seen in one-way gradient multilayers. At low incidence angles, the film is anti-reflecting for high gradient factors, and also becomes increasingly transmitting. This is likely due to the increased coupling and conservation of Bloch waves toward the back
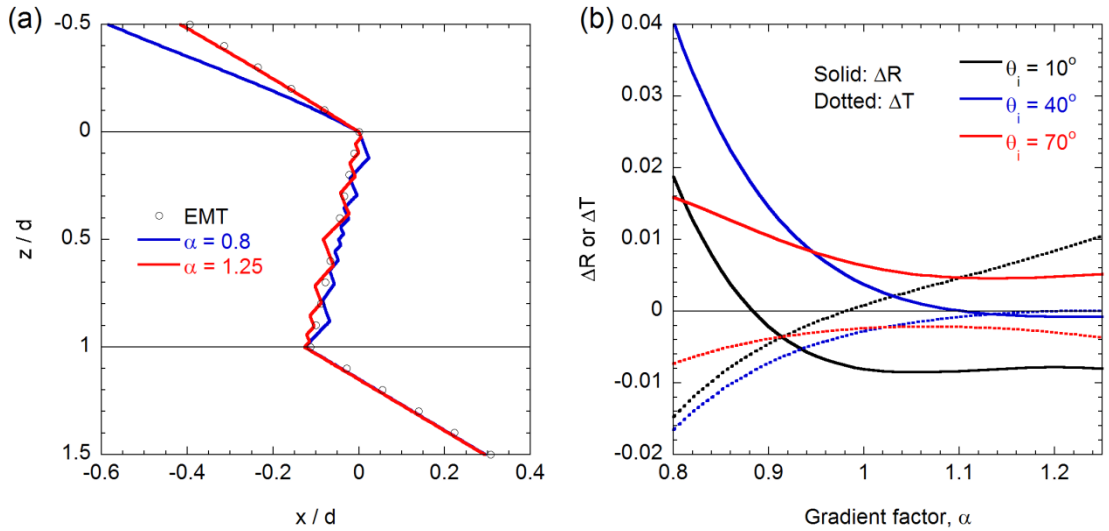
Figure 4.12 (a) Energy streamlines at $\theta_i = 40°$, and (b) the differences in reflectance or transmittance of symmetrically-graded multilayers.

of the thin film. While the differences in radiative properties between graded multilayers and EMT are small and cannot be easily detected by common spectrometers, the graded multilayers indicate the preference of very thin constituent layers especially close to the surface of the thin film.

4.5 Conclusion

In summary, the graphene-dielectric multilayers demonstrate negative angle refraction not in the traditional top-incidence orientation. Depending on the chemical potential or voltage biasing of the parallel graphene sheets, the effective anisotropic permittivity of the medium may be negative. Energy streamlines traced from side-incidence shows both positive and negative refraction in infrared wavelengths. Generally, the graphene-dielectric multilayers can serve negative refraction with increased chemical potential and in longer mid-infrared wavelengths. With improved technology to grow the graphene-dielectric multilayer films in the desired orientation, this work has promise in transparent subwavelength infrared imaging and filtering devices.

The three metal-semiconductor multilayer case studies offer understanding of the effect of material or layer properties on estimating the optics and radiative properties in negative index metamaterials. The traditional metal-dielectric (Ag-TiO$_2$) multilayers for visible wavelength refraction do not result in good agreement between EMT and the layered medium method. The dielectric and metal constituents are fairly lossy, leading to decay of Bloch waves especially within thick layers of few periods. While semiconductor-dielectric multilayers may offer practical advantages, not all cases can precisely use EMT to estimate radiative properties. Both the dielectric and semiconductor

should have minimized permittivity positive or negative magnitudes, respectively. In the examination of Bloch waves and the penetration depth, reduced imaginary component of both types of layers is recommended. Further refinement of semiconductor and dielectric permittivity tuning can lead to better future consumable optical devices.

The gradient multilayers offer an interesting exercise to design anti-reflecting thin films that also demonstrate negative refractive index. In general, the layers near the incidence surface and/or outgoing surface are made to be thin as possible. As well, EMT holds for gradient multilayer having subwavelength thicknesses. Although the differences in radiative properties from EMT are small, the fabrication techniques of such geometrically oriented multilayers certainly deserve further development.

CHAPTER 5

NEAR-FIELD ENERGY TRANSPORT BETWEEN METAMATERIALS

In this Chapter, the hyperbolic metamaterials investigated previously for far-field radiative properties are brought closer together to form a sub-micron vacuum gap between an emitter and receiver substrates. Due to coupling of evanescent waves at these distances, the near-field heat flux is improved several magnitudes over blackbodies in the far field [107,149,167]. The first section explores the near-field heat transfer between VACNT arrays and graphite. The transmission coefficient normalized wavevector and frequency contour is established to evoke meaning into near-field transport. The relationship of the vacuum gap distance and the heat flux enhancement over blackbody is shown to compare non-hyperbolic material versus hyperbolic metamaterial tunneling. Section 6.2 introduces graphene-covered VACNT arrays, where the graphene sheets promote surface plasmon polariton (SPP) resonance modes that are adjustable to chemical potential. The mechanisms are similarly explained here as well, alongside the photon penetration depth and near-field Poynting vectors into the substrates. The final section presents the near-field heat transfer between the graphene-dielectric multilayers presented in Chapter 4. A conclusion is provided to compare the capabilities of the various carbon-based hyperbolic metamaterials for near-field heat flux enhancement.

5.1 Heat Flux Enhancement between Carbon Nanotubes

The schematic of near-field heat transfer between two substrates of VACNT with different temperatures is shown in Figure 6.1. The VACNT array or film is treated as a homogeneous semi-infinite medium. This assumption is reasonable because the

fabricated VACNT arrays could be as long as several millimeters and have high absorption coefficients [137]. In the remaining sections, each emitter and receiver substrate is assumed to be at equilibrium temperature of T_1 = 300 K and T_2 = 0 K, respectively. Furthermore, the optical constants of the two media are assumed to be the same based on the room-temperature values.
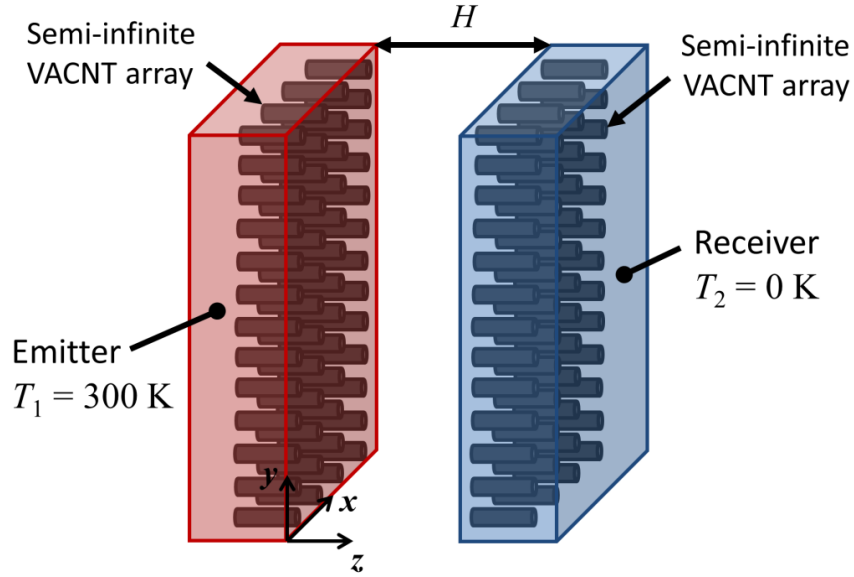
Figure 5.1 Schematic of near-field radiative heat transfer between VACNT emitter and receiver separated by a vacuum gap distance of H. The VACNT substrates are treated as semi-infinite homogeneous media at thermal equilibrium.

In graphite, two Type II hyperbolic regions are delineated: One at angular frequencies below 2.1×10^{13} rad/s (due to free electrons) and the other ranging from 3.0×10^{13} rad/s to 1.8×10^{14} rad/s (associated with the interband transition). The dielectric functions of VACNT are determined using Eqs. (2.8) and (2.9), where the filling ratio and alignment factor remain at $f = 0.05$ and $\xi = 0.98$, respectively. The two Type I hyperbolic bands corresponding to Fig. 3.1 given in angular frequency are given as:

1.4×10^{13} rad/s to 2.1×10^{13} rad/s (low frequency band), and 3.0×10^{13} rad/s to 1.3×10^{14} rad/s (high frequency band).

To predict the thermal transport of photons across the vacuum gap, the normalized wavevector (k_x / k_0) and angular frequency contours for the TM wave transmission coefficient ($\mathcal{T}_p$) are drawn. Figure 6.2 shows them for VACNT and graphite substrates separated by a $H = 10$ μm vacuum gap. Note that only TM waves need to be considered since the contribution of TE waves is negligible at deep submicron gap distances. The transmission contour does not have shape discontinuities across regions with different dispersions. This is due to the imaginary parts of the permittivities being nonzero. The boundaries are very sharp and clear if loss were intentionally removed, although the results are not shown here. A large transmission coefficient at large normalized wavevector in the evanescent regime ($k_x / k_0 > 1$) means more photon tunneling modes or channels for near-field transport.

Fig. 6.2(a) clearly suggests that hyperbolic modes in VACNT are broadband. Therefore, these hyperbolic modes significantly contribute to the large heat flux between VACNT arrays. The brightly colored low frequency region with high transmission coefficients is due to the symmetric coupling of SPPs at the two interfaces between the vacuum gap and the anisotropic VACNT films on both sides. The coupled SPP dispersion between two uniaxial materials separated by a vacuum gap can be obtained by zeroing the denominator of $\mathcal{T}_p$. After some manipulation, the coupled SPP dispersion (symmetric branch) is given as [168],

$$\gamma = \frac{k_z}{\varepsilon_O} \coth\left(\frac{i\gamma H}{2}\right) \tag{5.1}$$

The symmetrically coupled SPPs dispersion governed by Eq. (5.1) is shown in Fig. 5.2(a) as the white dashed curve. Above 1.4×10^{13} rad/s, ε'_O becomes positive and thus the asymmetrically coupled SPP mode does not exist.
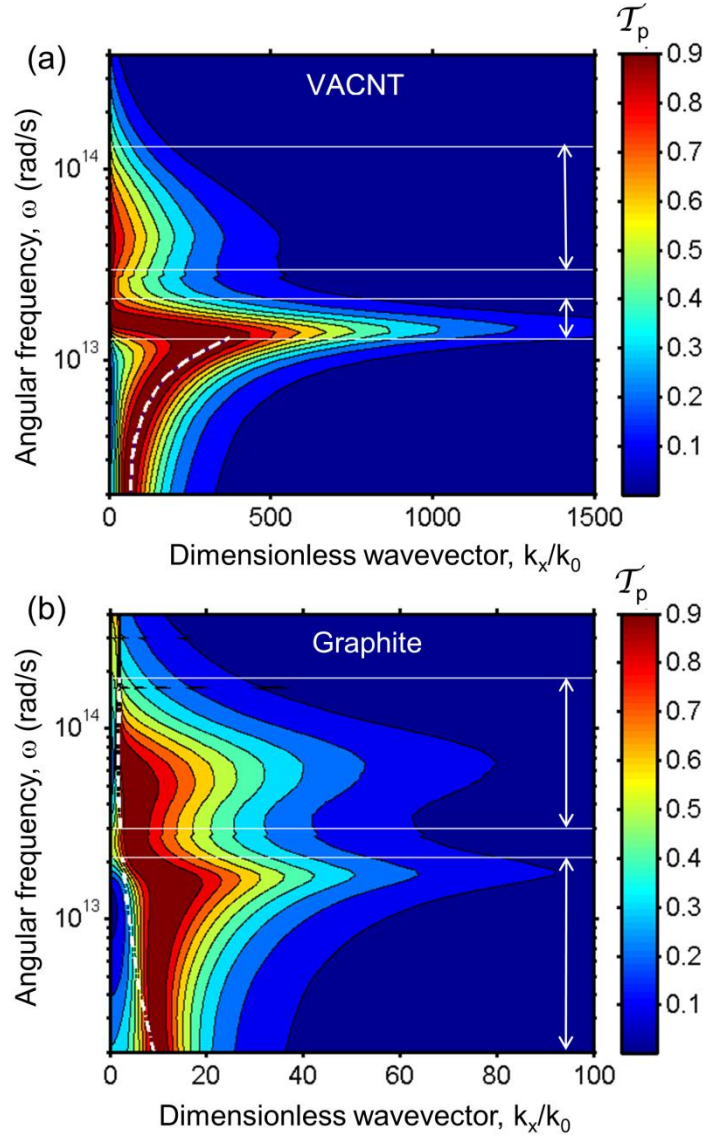
Figure 5.2 Contour of the near-field transmission coefficients in lateral wavevector and frequency space for p-polarization at $H = 10$ nm: (a) VACNT for which the dotted line depicts the symmetrically coupled SPP branch, and (b) graphite for which the dash-dotted lines indicate the critical wavevectors separating evanescent waves (left) and propagating waves (right). Arrows between the horizontal lines indicate the hyperbolic bands according to the shaded regions in Figure 3.1 corresponding to either VACNT or graphite (not shown).

For graphite as shown Fig. 5.2(b), the two Type II hyperbolic bands also result in high transmission coefficients for large wavevector values. Note from Section 2.2 that electromagnetic waves are always propagating in Type I hyperbolic band, while for Type II metamaterials propagating waves are supported only when k_x is greater than the critical wavevector, given by $k_{cr} = k_0\sqrt{\varepsilon_\parallel}$. The critical wavevectors are depicted in Fig. 5.2(b) as the dash-dotted lines in both hyperbolic bands. Note that the argument made here is based on low-loss materials for which the imaginary part of the corresponding dielectric function is much smaller than the real part. The distinction between propagating and evanescent waves is obscure in high-loss materials. Nevertheless, it can be seen from Fig. 5.2(b) that the transmission coefficients are very small when $k_x < k_{cr}$, thus the regions on the left of the dash-dotted lines contribute little to the heat flux. Once $k_x > k_{cr}$, $\text{Im}(r^p)$ becomes nontrivial and the transmission coefficient can be very large [161]. For both types of materials, the hyperbolic modes can be viewed as a special type of frustrated total internal reflection modes [169]. Because VACNT is able to support an SPP resonance band and achieve relatively low loss in its permittivity, enhanced near-field transmission is possible.

The spectral heat fluxes between VACNT and graphite plates separated at $H = 10$ nm are plotted in Figure 5.3 along with that between two blackbodies in the far field. The low- and high-frequency Type I hyperbolic peaks for VACNT are located at 1.52×10^{13} rad/s and 4.97×10^{13} rad/s, respectively. An interesting phenomenon is that the spectral heat flux at frequencies lower than 2.1×10^{13} rad/s (shaded region) only contributes 0.64% for blackbodies, while for VACNT the low-frequency contribution would be as high as 14.3% due to hyperbolic modes along with the coupled SPPs. These values are obtained

88

from the cumulative or integrated heat flux distribution (not shown here). It can also be

seen from Fig. 5.3 that the peaks in the spectral heat flux due to the hyperbolic modes are

at lower frequencies than that for far-field blackbodies (BB). In this respect, VACNT

arrays are a good candidate for near-field thermal radiation at cryogenic temperatures,

since Planck's oscillator would give a heavier weight toward lower frequencies with

decreasing temperature.
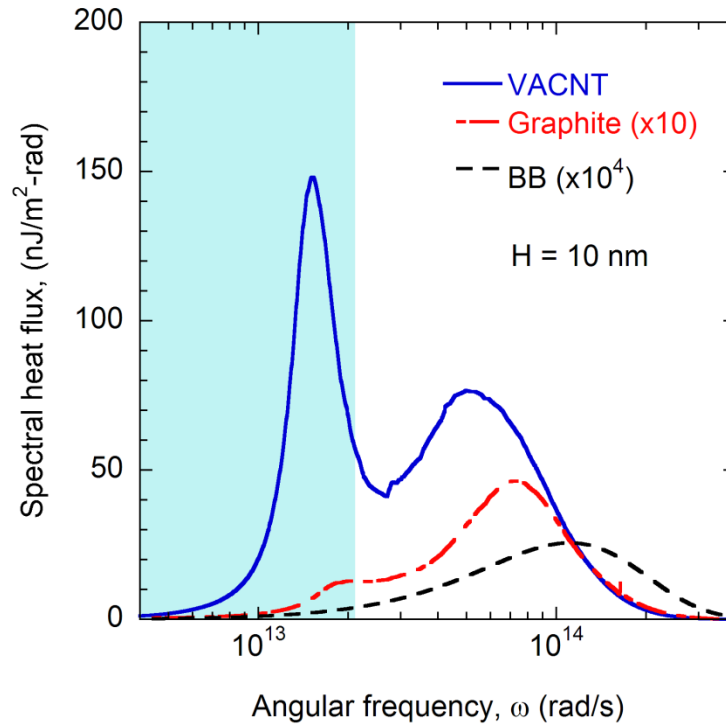
Figure 5.3 Comparison of the spectral heat fluxes (in nW/m^2 per rad/s) for VACNT and
graphite (scaled up by 10) at $H = 10$ nm, and that for blackbodies (scaled up by 10^4) in
the far field. The shaded region represents the contributions to near-field radiative
transfer for VACNT by the symmetrically coupled SPP and low-frequency hyperbolic
modes.

Figure 5.4 plots the radiative heat flux divided by that between blackbodies

(Q_{BB}) as a function of gap distance for both VACNT and graphite. For the purpose of

comparison, the heat flux for silicon carbide (SiC) is shown since it is widely used in

thermal radiation analysis and experiments due to its capability of supporting surface

phonon polaritons in the mid-infrared region. In terms of heat transfer enhancement,

VACNT can outperform SiC for any gap distance ranging from deep submicron to the far

field. When $H = 10$ nm, Q_{VACNT} / Q_{SiC} is as high as 9.7, confirming that VACNT arrays

are very promising for near-field localized thermal management and thermal imaging. In

the far field, Q_{VACNT} / Q_{BB} is 0.90, which agrees with the absorptance results discussed

in Chapter 3.
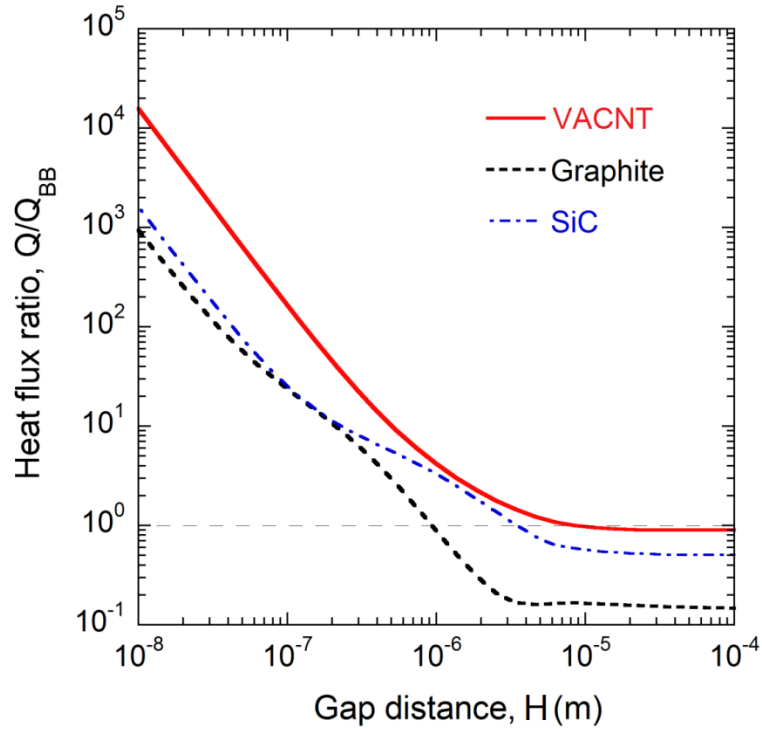
Figure 5.4 Near-field radiative heat flux (divided by the blackbody heat flux in the far
field) for H ranging from 10 nm to 100 μm.

Although graphite does not support SPPs or negative refraction, due to its Type II

hyperbolic dispersion in the infrared region, it can also enhance near-field radiative

transfer to a level close to that of SiC. While it has been reported that the emissivity of

graphite could exceed 0.8, the studied samples usually have rough surfaces with texture structures [170]. For highly polished smooth surfaces, the large absolute values of $\varepsilon_\perp$ make graphite a low-emissivity material in the mid-infrared [113].

The filling ratio of VACNT arrays can also affect heat flux, and increasing the filling ratio f beyond 0.05 would cause additional loss that impairs the heat transfer. On the other hand, decreasing f can further increase the heat flux up to a maximum when $f = 0.013$ for $H = 10$ nm. Smaller filling ratio not only reduces heat flux, but also EMT may break down since the CNT unit cell spacing exceeds that of the vacuum gap size [161]. The enhanced heat transfer can also be assessed by evaluating the heat transfer coefficient, which is essentially the heat flux per unit temperature difference, near room temperature. The heat transfer coefficient for VACNT near room temperature with $H = 10$ nm is calculated to be 5.3×10^4 W/m^2-K, which is nearly six times that for SiC.

5.2 Mode Hybridization using Graphene

The schematic for calculating near-field radiative transfer is depicted in Figure 5.5, which consists of two semi-infinite VACNT arrays separated by a vacuum gap. In the cases of interest, each VACNT array is covered by a single-layer graphene sheet. Unlike continuous structures such as pillared graphene where phonon scattering dominates near the graphene-CNT junctions, the graphene sheet is assumed to not bond or interact with the CNT substrate, which could degrade their unique electronic properties [122,171,172]. In order to maximize radiative heat flux, graphene doping levels or chemical potentials are set equal on both the emitter and receiver [128].
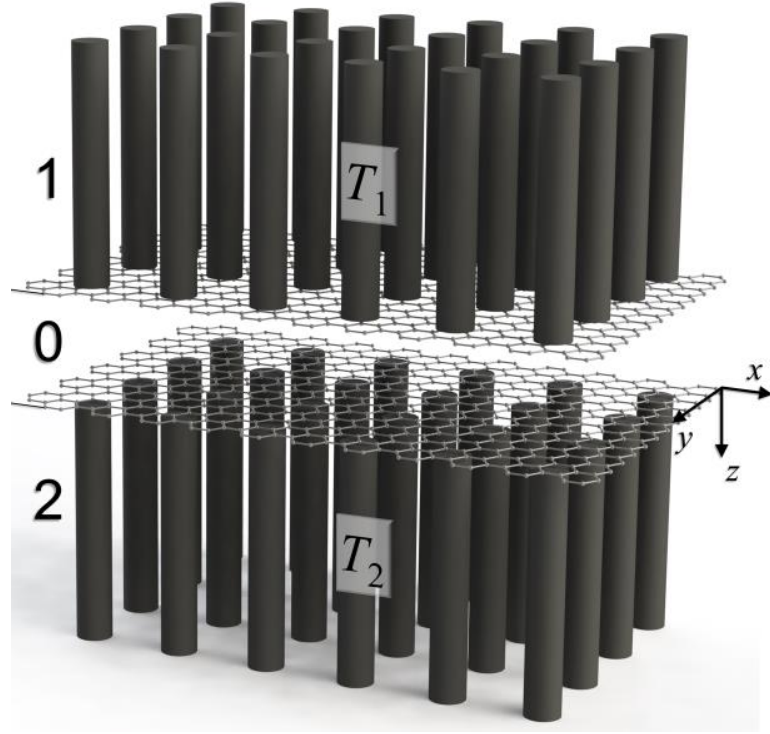
Figure 5.5   3D illustration of semi-infinite VACNT media covered with single-layer graphene sheets. The nomenclature follows that of Figure 2.6.

Based on the spectral graphene conductivity models presented in Chapter 4, the Fresnel reflection coefficients can be retailored to include graphene as sheet currents at the emitter (01) and receiver (02) interfaces. The re-derived coefficients are given by,

$$r^{\mathrm{S}} = \frac{\gamma - k_z^{\mathrm{S}} - \sigma \omega \mu_0}{\gamma + k_z^{\mathrm{S}} + \sigma \omega \mu_0} \qquad (5.2\mathrm{a})$$

$$r^{\mathrm{p}} = \frac{\varepsilon_{\mathrm{O}} \gamma - k_z^{\mathrm{p}} + \sigma k_z^{\mathrm{p}} \gamma / \omega \varepsilon_0}{\varepsilon_{\mathrm{O}} \gamma + k_z^{\mathrm{p}} + \sigma k_z^{\mathrm{p}} \gamma / \omega \varepsilon_0} \qquad (5.2\mathrm{b})$$

where $\gamma = \sqrt{k_0^2 - k_x^2}$. For cases with no graphene covering the VACNT arrays, one can simply set $\sigma = 0$, which gives the original Fresnel coefficients for interfaces. The conductivity of graphene is plotted in Figure B.2 in Appendix B in terms of the angular frequency, in order to predict the trends in Eq. (5.2). Another way of determining the

Fresnel coefficients is to assume graphene as an ultrathin layer, and use the TMM discussed in the calculations pertaining to the previous Chapter. The two methods yield essentially the same results.

The reestablished Fresnel coefficients given in Eq. (5.2) conform to the terms in the transmission coefficient, from Eq. (2.30). Figure 5.6 shows the transmission coefficient across a broad frequency and lateral wavevector range. The upper-bound frequency is determined by the optical phonon frequency $\omega_{op} \approx 3 \times 10^{14}$ rad/s. Above such frequency, optical phonon emission alongside electron-hole pair coupling is significant [64]. Here, the relaxation time is overcome by electron-phonon scattering and high plasmon losses, resulting in as large as an order magnitude reduction. The lower bound frequency is set to 3×10^{12} rad/s. This broad frequency range includes most of the thermal radiation emitted at 300 K.

The contour plot figures in the left column correspond to the transmission coefficient between two graphene sheets separated by a vacuum gap (H = 100 nm), but without substrates, called vacuum-suspended graphene. The right-side column figures describe the near-field device including the VACNT substrates from Fig. 5.5. The three rows are associated with different chemical potentials, μ = 0.1 eV, 0.3 eV, and 0.6 eV, respectively. The purpose of illustrating the transmission coefficient of vacuum-suspended graphene is to determine the SPP dispersion between graphene sheets. The coupled SPP dispersion relation of graphene is given by [173,174],

$$\frac{2\omega\varepsilon_0}{\gamma\sigma} = \pm \exp(i\gamma H) - 1 \tag{5.3}$$
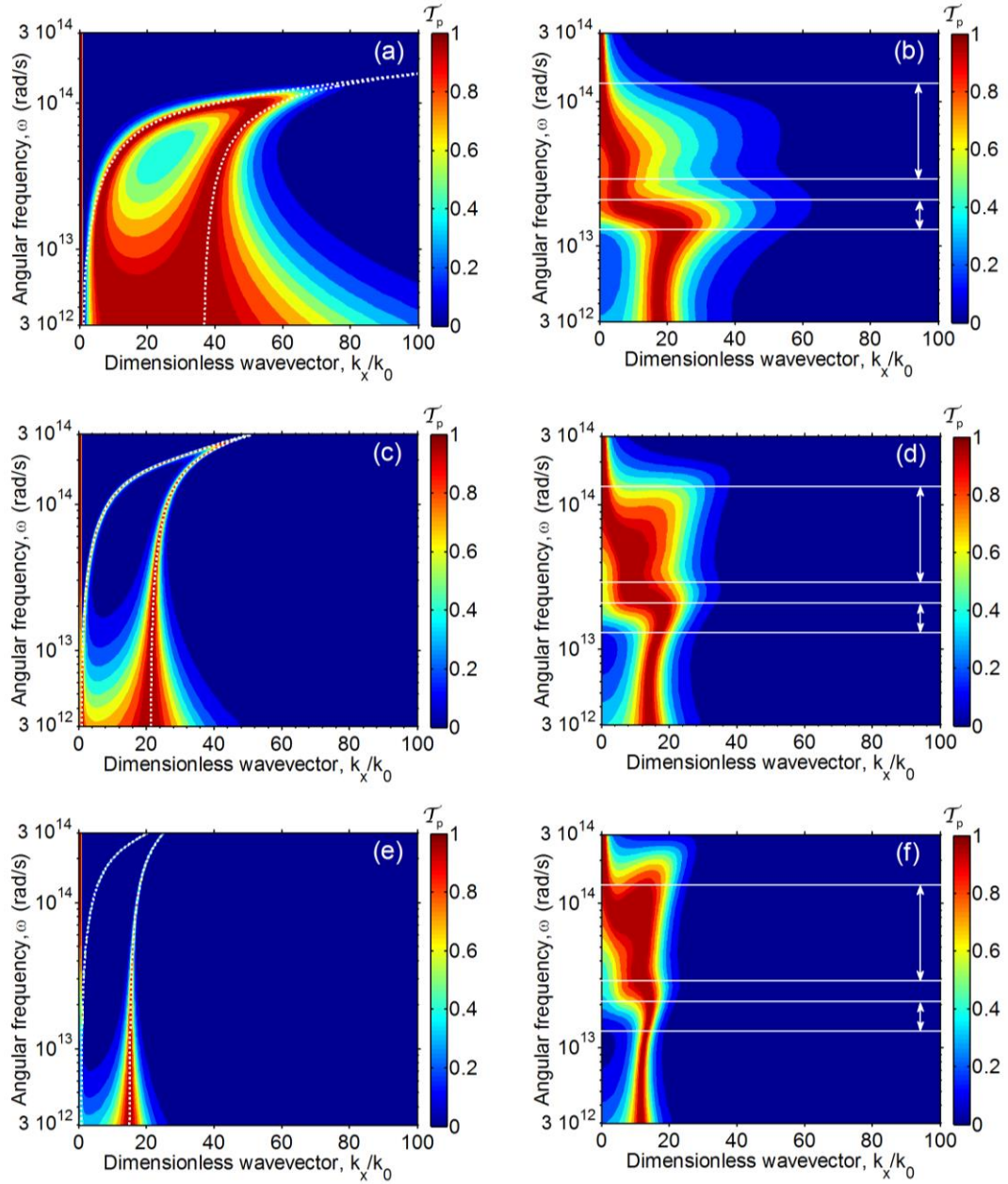
Figure 5.6 Near-field transmission coefficient contours of vacuum-suspended graphene for chemical potentials of (a) $\mu = 0.1\,\text{eV}$, (c) 0.3 eV, and (e) 0.6 eV. The hybridization of graphene plasmon resonance and hyperbolic modes is observed in the graphene-covered VACNT configuration at (b) $\mu = 0.1\,\text{eV}$, (d) 0.3 eV, and (f) 0.6 eV. The hyperbolic dispersion frequency regions of VACNT are denoted by the white arrows between the horizontal lines. The near-field gap distance used for this figure and every successive figure is $H = 100$ nm.

In Figs. 5.6(a), (c), and (e), the SPP dispersion curves or bands are drawn in dotted white lines. The symmetric band, as shown by the left-hand line, has a $\omega \propto \sqrt{k_x}$ relationship and originates close to the light line [175]. The anti-symmetric mode is represented by the right-hand line, and its resonant lateral wavevector increases inversely with the separation distance H. The two SPP mode lines merge toward high frequencies [176].

Some notable observations on the transmission contours: For greater chemical potential, near-unity transmission in the low frequency range covers a narrow band of lateral wavevectors. This low frequency band reflects the narrowing of vacuum-suspended graphene anti-symmetric SPP dispersion. On the other hand, in the high frequency region, the band of near-unity transmission is broadened, and in the case when $\mu = 0.6$ eV, high transmission is extended to include frequencies beyond the hyperbolic band. Therefore, with higher chemical potential, the low frequency region suffers decreasing number of hyperbolic modes in order to support broad near-unity transmission in the high frequency hyperbolic region. However, why do the SPP bands of weakly doped graphene exhibit less influence on the transmission contour of the hybridized structure, as such seen in Fig. 5.6(b)? In reference to Eq. (2.30), the denominator of the transmission coefficient is found to be many orders of magnitudes smaller when the chemical potential is increased [177,178]. While weakly doped graphene shows broader near-unity transmission in the vicinity of the SPP dispersion lines, the denominator of the transmission coefficient is far from zero. When the denominator is zero, which happens to be the SPP dispersion relation given in Eq. (5.3), perfect SPP resonance will occur.

Figure 5.7 gives the transmission coefficient at $\omega = 1.5 \times 10^{13}$ rad/s and $\omega = 1.0 \times 10^{14}$ rad/s to demonstrate the tradeoffs more clearly at both a low frequency

and high frequency. In Fig. 5.7(a), without graphene, the transmission coefficient is $\mathcal{T}_p \geq 0.3$ in the lateral wavevector range indicated. With graphene, the number of evanescent modes promoting high near-field transmission is reduced. Especially with high chemical potential, the peak of the lateral wavevector is shifted toward smaller values and narrowed.
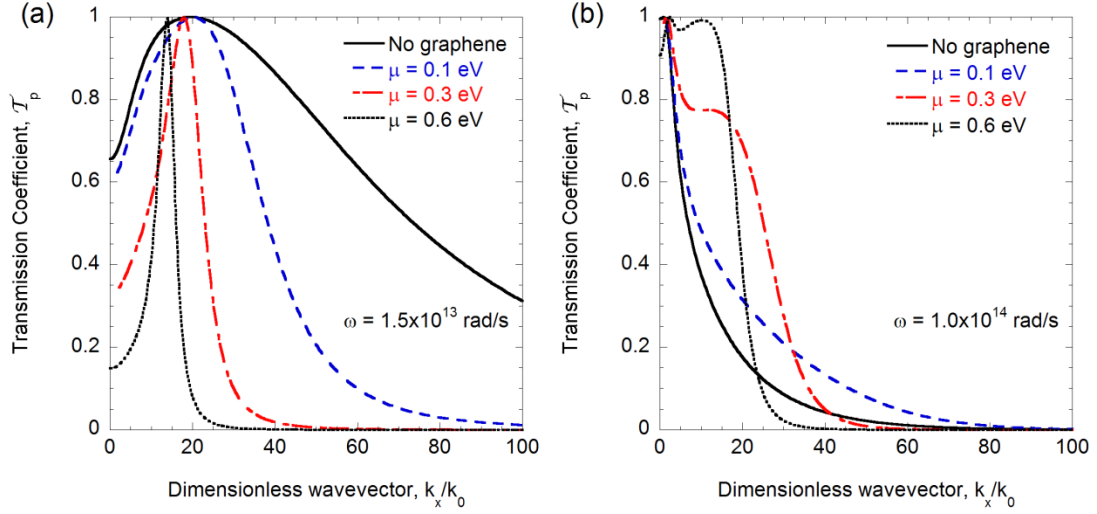
Figure 5.7 The transmission coefficient between VACNT for both uncovered and graphene-covered configurations, shown at frequencies (a) $\omega = 1.5 \times 10^{13}$ rad/s, and (b) $\omega = 1 \times 10^{14}$ rad/s.

The trend at $\omega = 1.0 \times 10^{14}$ rad/s is quite different, as evidenced in Fig. 5.7(b), since graphene is able to improve the range of near-unity transmission. A "shoulder" is observed in the evanescent modes close to $k_x / k_0 = 20$ for $\mu = 0.3$ eV, and evolves into dual peaks near unity for $\mu = 0.6$ eV. One may also notice the sharp drop in $\mathcal{T}_p$ for $k_x / k_0 > 20$. Although both frequencies satisfy hyperbolic dispersion in the VACNT substrate, highly doped graphene presents strong surface plasmons that can either disrupt or add to the hyperbolic modes depending on the frequency.

The spectral heat flux mentioned in Eq. (2.28) is shown in Figure 5.8, as the spectral heat flux in base units of W/m^2 per rad/s. Fig. 5.8(a) compares such spectra between uncovered VACNT and graphene-covered VACNT. Due to the large number of evanescent modes in the low frequency hyperbolic region, the spectral heat flux has a dominant peak near 1.5×10^{13} rad/s. In the presence of graphene, this peak is immensely curbed. By how much, the normalized cumulative heat flux from Fig. 5.8(b) reveals the contribution by the low frequency modes up to 2.1×10^{13} rad/s. The low frequency region heat flux contribution of uncovered VACNT was found to be 14%, but with graphene this drastically decreases down from 2.7% to 0.7%, from low to high doping.
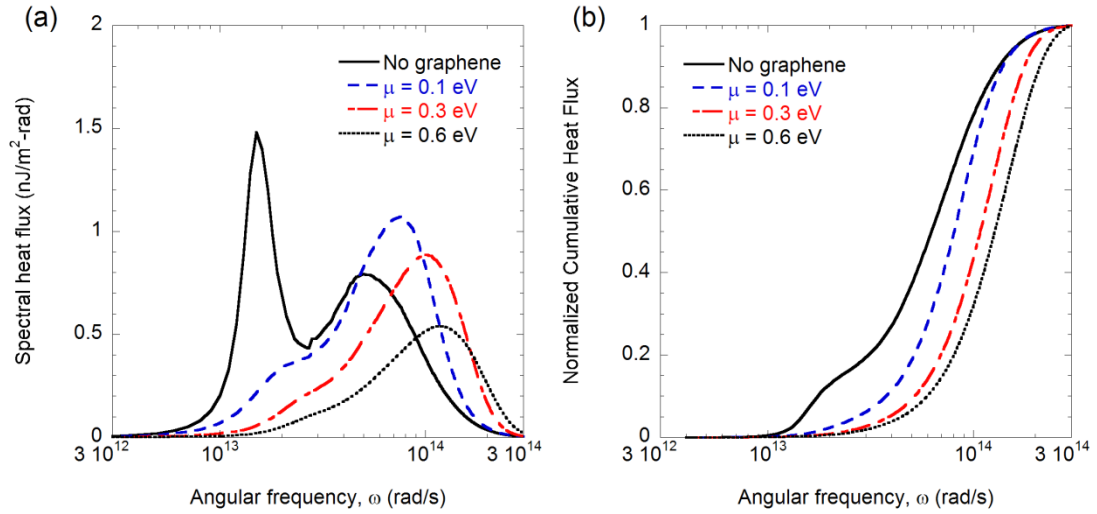
Figure 5.8 (a) Spectral heat flux (nW/m^2 per rad/s) for uncovered and graphene-covered VACNT, and (b) the normalized cumulative heat flux up to the optical phonon frequency, $\omega_{op} \approx 3 \times 10^{14}$ rad/s.

Meanwhile, the second peak due to the high frequency hyperbolic mode is improved with some doped graphene. At $\mu = 0.1$ eV, this peak not only increases in magnitude, but also shifts toward a higher frequency. With $\mu = 0.3$ eV and onwards, the

peak frequency shifts farther up, agreeing well with the interband transition shift discussed earlier. However, highly doped graphene comes at a cost, since the extent of lateral wavevectors that present non-negligible transmission ($\mathcal{T}_\mathrm{p} > 0.05$) is reduced. Even with the formation of a near-unity transmission butte that is shifted toward the high frequency, the resulting spectral heat flux is diminished. This effect occurs in doped graphene at $\mu = 0.6$ eV, where the high frequency peak becomes shorter than that for uncovered VACNT.

Figure 5.9 gives relationship of the heat flux enhancement over blackbody to the gap distance and the chemical potential. In Fig. 5.9(a), graphene slightly improves heat transfer starting at $H \approx 20$ nm, and decays with $Q \propto H^{-2}$. Below the nanometer-scale sizes, a $Q \propto H^{-1}$ relationship is observed for the graphene-covered VACNT, which matches well with a recent study [179]. Despite the counterproductive effect of graphene at these small gap distances, the validity of using EMT in near-field calculations breaks down. Considering any of the three graphene chemical potentials, the enhancement over uncovered VACNT is provided for gap distances between 91 nm and 2 μm. With the latter gap distance, the heat flux enhancement over black body is insignificant anyway. The graphene chemical potential that results in the greatest heat flux enhancement is dependent on the gap distance. In the inset of Fig. 5.9(a), at $H = 50$ nm, graphene at $\mu = 0.1$ eV is preferred over highly doped graphene. On the other end, at $H = 200$ nm, graphene doped at $\mu = 0.3$ eV and 0.6 eV are preferred. The understanding is that increasing the gap distance shifts the anti-symmetric SPP band toward higher lateral wavevectors. This graphene SPP band, especially at stronger chemical potential, will

coincide with the suppressed VACNT SPP band situated at similar lateral wavevectors. It

is assumed that this SPP substitution can continue to support a broad lateral wavevector

range of hyperbolic modes.
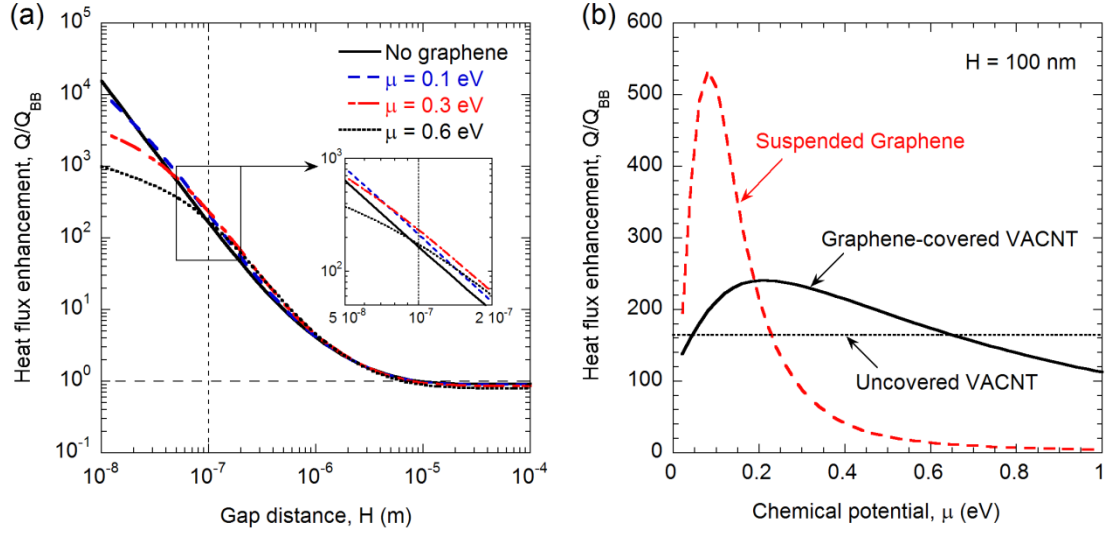
Figure 5.9 (a) Heat flux enhancement over that of black body of uncovered and graphene-covered VACNT for near-field gap distances between $H = 10$ nm and $H = 100$ μm. (b) Effect of graphene chemical potential on heat flux enhancement between graphene-covered VACNT, and between vacuum-suspended graphene. The horizontal dashed line represents the heat flux enhancement between uncovered VACNT.

Fig. 5.9(b) plots the heat flux enhancement with changing chemical potentials for

graphene-covered VACNT and suspended graphene. The solid line, representing the

former, gives the range of graphene chemical potential that results in enhancement over

uncovered VACNT (horizontal dashed line). At $\mu = 0.22$ eV, the heat flux over that of

far-field black body is maximized at 241 times, and over that of uncovered VACNT at

1.5 times. Too highly biased graphene ($\mu > 0.65$ eV) results in suppressed heat transfer

over uncovered VACNT, at least for the 100 nm gap distance. Just between two vacuum-

suspended graphene sheets, the heat flux enhancement is maximized at a low doping

level. Looking back at Fig. 5.6(a), the SPP dispersions yield high transmission

coefficients throughout the contour plot. At lower chemical potential, the SPP dispersion lines approach an asymptotic cutoff frequency, in which above it no tunneling can occur. For higher chemical potential, despite the stronger resonance conditions, near-unity transmission is highly localized at the SPP modes, especially at high frequencies. In the low frequency, the anti-symmetric SPP pass-band is limited to smaller lateral wavevectors. When graphene and VACNT are combined, the chemical potential that yields the highest heat flux enhancement is increased due to the presence of underlying hyperbolic modes from the VACNT substrate. Essentially, the hybrid structure is desirable when the graphene SPP modes couple to improve the weaker hyperbolic band in high frequencies, but also allow broad non-local transmission in the low hyperbolic band frequencies and below.

The near-field heat transport mechanism is further investigated by evaluating the electromagnetic fields in each medium. The derivative of the Poynting vector with respect to z essentially shows the amount of energy absorbed or emitted per unit depth per unit time. In the vacuum gap, the Poynting vector given by Eq. (2.32) should correspond to the near-field heat flux. But, how will SPP modes or hyperbolic modes contribute inside the emitter and receiver media? Further, the presence of graphene could improve photon penetration. The implications of greater penetration depth would suggest that thicker VACNT films are needed in order to satisfy the semi-infinite substrate assumption [88].

Figure 5.10 demonstrates the wavevector-averaged Poynting vector for both uncovered VACNT and graphene-covered VACNT at a vacuum gap distance of 100 nm. The spatially-dependent Poynting vector is first normalized to that in the vacuum gap,

such that $\langle S_z(z)\rangle / \langle S_{z,\text{vacuum}}\rangle = 1$ when $0 < z/H < 1$. The Poynting vector profiles are

evaluated at a range of evanescent wavevectors, from $k_x/k_0 = 1^+$ to $k_x/k_0 = 200$, and

then averaged. The lateral wavevector modes that correspond to near-unity transmission

coefficients (from Fig. 5.6) exert greater influence on the integrated Poynting vector.
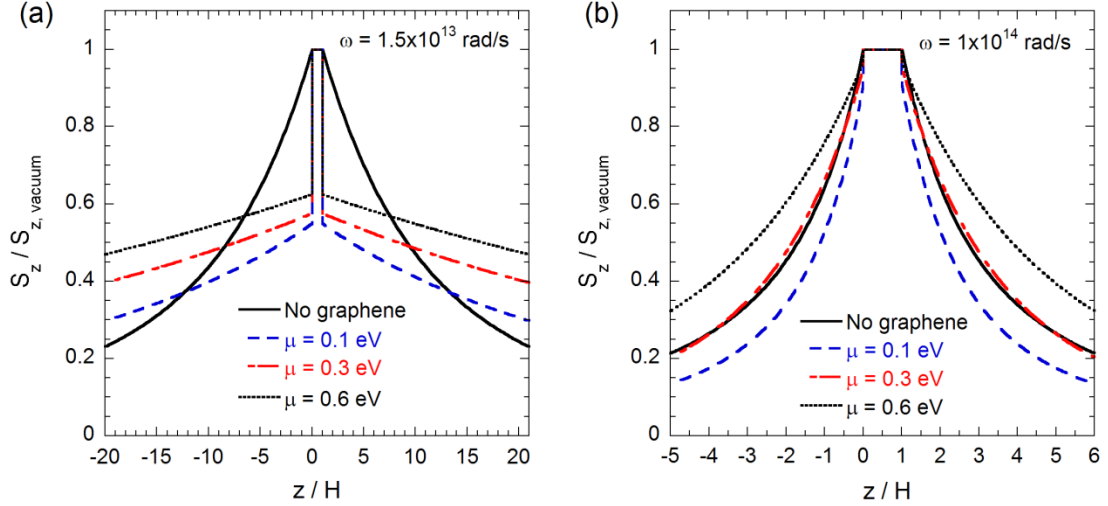
Figure 5.10   Lateral wavevector-averaged longitudinal (z-direction) Poynting vector normalized to that in the vacuum gap, for hyperbolic and graphene SPP-hybridized mode frequencies (a) $\omega = 1.5\times 10^{13}$ rad/s and (b) $\omega = 1\times 10^{14}$ rad/s.

Without the presence of graphene, no discontinuity in the Poynting vector is

observed. With graphene sheets, Poynting vector discontinuities are seen near $z/H = 0^-$

and $z/H = 1^+$, precisely, inside the thin graphene-defined layers. The amount of

absorption depends on both graphene chemical potential and frequency. At the low

frequency regime $(1.5\times 10^{13}$ rad/s$)$, in the narrowband hyperbolic dispersion that is

supported by the suppressed VACNT SPP band, the presence of graphene has profound

effects on energy absorption, as seen in Fig. 5.10(a). With increasing chemical potential,

graphene is less absorbing at the surface and promotes longer penetration depth. The penetration depth is determined using,

$$S_z(\delta - H) = \frac{S_z(H + \Delta_g)}{e}$$ (5.4)

The exponentially sloped decay begins at the interface between graphene and the semi-infinite VACNT substrate ($z = H + \Delta_g$). Without graphene, the penetration depth at 1.5×10^{13} rad/s is $\delta = 1.2 \ \mu m$. A summary of the penetration depths for each chemical potential level is given in Table 5.1. The gradual increase in the penetration depths with doping in the frequency band is due to the shift from VACNT SPP to graphene SPP, the latter situated at smaller lateral wavevectors. Accordingly, the steeper evanescent waves at small k_x allow maximization of the spectral penetration depth [180].

Table 5.1 Penetration depths (δ) of VACNT-graphene near-field device.

	$\omega = 1.5 \times 10^{13}$ rad/s	$\omega = 1.0 \times 10^{14}$ rad/s
No graphene	1.2 μm	0.27 μm
μ = 0.1 eV	3.5 μm	0.21 μm
μ = 0.3 eV	5.6 μm	0.30 μm
μ = 0.6 eV	7.2 μm	0.45 μm

At 1.0×10^{14} rad/s, the hyperbolic mode is weaker, resulting in smaller penetration depths. As well, the discontinuity in the Poynting vector due to the presence of graphene is reduced. The increased penetration depth with chemical potential is due to the dominant modes toward smaller lateral wavevectors, in agreement with the observed

shape-shift seen in Fig. 5.7(b). For even higher frequencies (i.e., 2×10^{14} rad/s), the lack of intrinsic VACNT hyperbolic dispersion results in small reductions in penetration depths due to graphene (not shown). The general increase in penetration depth due to the SPP of strongly doped graphene may impose limits on the design of VACNT substrates in near-field thermal applications. The rule of graphene over both the VACNT hyperbolic and suppressed SPP modes at frequencies below $\omega\approx3\times10^{13}$ rad/s hints the need for tens-of-microns thick VACNT substrates for far-infrared situations. On the other hand, the presence of graphene in the high frequency range has an exclusively beneficial effect. Since the VACNT hyperbolic is present albeit weak, the hybridization with graphene allows for improved radiative transfer without the need for extremely deep VACNT substrates. The fascinating properties of graphene uncovered in this recent discussion prove its favorable use in mid-infrared near-field radiative transfer between hyperbolic materials.

5.3 Near-Field Graphene-Dielectric Multilayers

The graphene-dielectric multilayers from Section 4.2 are brought now into the near field. Figure 5.11 shows the multilayered substrates oriented with the graphene sheets parallel to the interface. The same nomenclature is used as Fig. 5.1, and since the substrates are assumed to be semi-infinite, $N=\infty$.

The near-field transmission coefficient contours of multilayers separated by a $H=50$ nm vacuum gap are shown in Figure 5.12. Here, the dielectric spacer size is $d_\mathrm{d}=10$ nm, which corresponds to the dielectric function from Fig. 4.2(b). At $\mu=0.1$ eV, the transition wavelength between positive permittivity and hyperbolic dispersion is
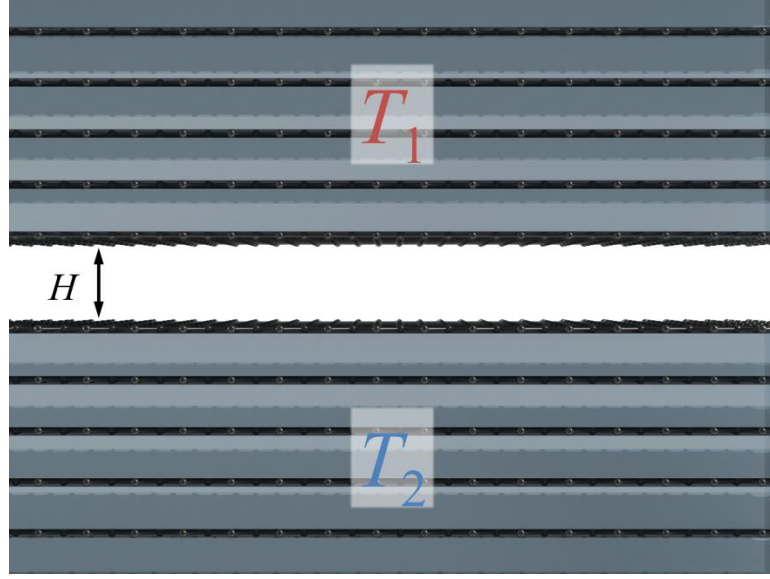
Figure 5.11 Illustration of graphene-dielectric multilayers separated by a vacuum gap.

14.4 μm. This corresponding wavelength is shown by the white horizontal line

$(\omega=1.3\times10^{14}$ rad/s) in Fig. 5.12(a). Above the line, no hyperbolic modes exist, and the

transmission coefficient is only permitting for propagating waves. Below, the hyperbolic

dispersion is Type II, in which left of the critical wavevector $(k_{cr}/k_0=\sqrt{6.0})$ no

transmission can occur. For higher chemical potential (0.4 eV), the breadth of the

hyperbolic region is much larger, up to $\omega=2.8\times10^{14}$ rad/s, shown in Fig. 5.12(b). High

transmission is near the transition frequency, in which the real component is near zero

and the imaginary component is relatively large. Similar to that of graphite, the

evanescent modes diminish toward lower frequencies since the imaginary component of

the Fresnel reflection coefficient becomes not as significant. No SPP resonance bands are

possible, so that penetrating evanescent modes decay relatively quickly toward the right

of the critical wavevector. In this sense, the graphene-dielectric multilayers become a

graphite-like near-field substrate, but enables tunability with graphene biasing.
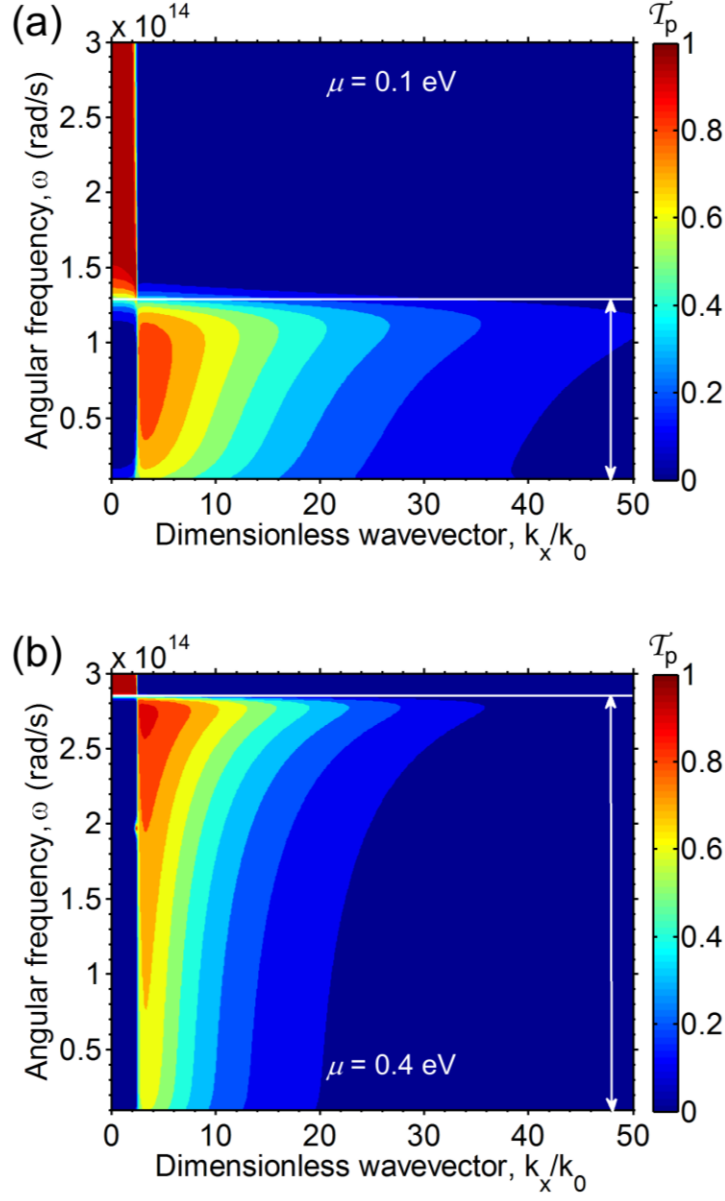
Figure 5.12   Near-field TM wave transmission coefficient for graphene-dielectric multilayers separated by a $H = 50$ nm vacuum gap. The chemical potential of the graphene sheets in multilayers are (a) $\mu = 0.1$ eV and (b) $\mu = 0.4$ eV. The white line and arrow delineates the hyperbolic region.

To compare the near-field heat flux between the multilayers and graphite, the heat flux enhancement over that of blackbody (Q/Q_{BB}) is plotted. Figure 5.13(a) demonstrates three chemical potential levels ($\mu = 0$ eV, 0.1 eV, and 0.4 eV) in a gap

distance range between 10 nm to 10 μm. Without biasing, the multilayers have a slight improvement over graphite in the near field. However, due to the composition of the dielectric, is more absorbing in far-field radiation (i.e., $H > 1 \mu$m). Increasing the chemical potential certainly improves the heat flux in the near field, but graphene at too high chemical potential may suffer in the far field. Increasing conductivity of graphene produces highly reflecting surfaces, as similarly shown in Fig. 4.4(b). Therefore, there is an optimal chemical potential for both near-field and far-field transport. The transition frequency between positive and hyperbolic permittivity determines whether the enhancement is favored toward the near field or far field.
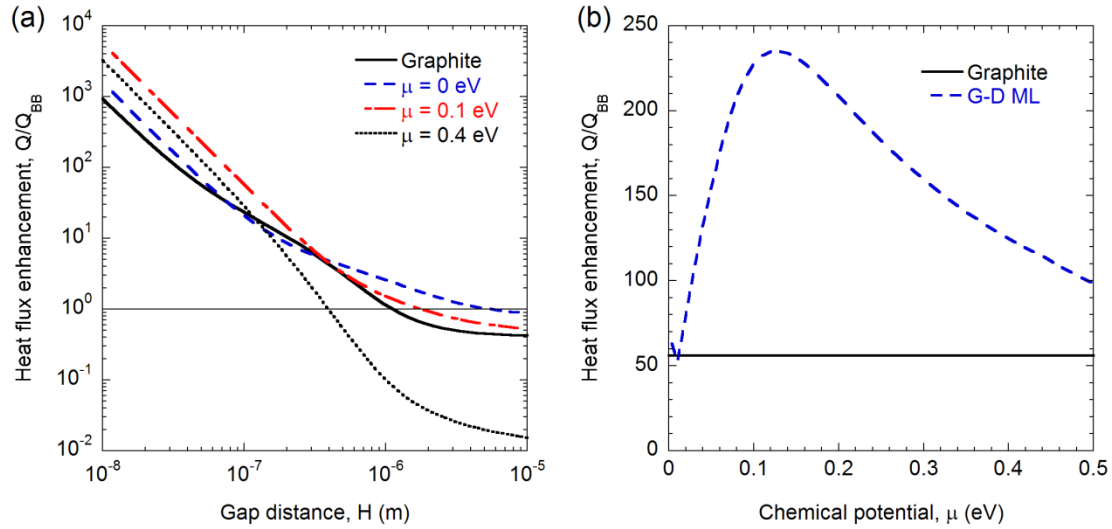
Figure 5.13   Heat flux enhancement of graphene-dielectric multilayers over that of blackbody: (a) Variation with gap distance compared to graphite, and (b) with chemical potential at fixed gap distance ($H = 50$ nm).

Fig. 5.13(b) demonstrates the heat flux enhancement with varying chemical potential and fixed gap distance at $H = 50$ nm. The best enhancement occurs at $\mu = 0.13$ eV, and approaches graphite toward no biasing. The dielectric spacers can also

be tuned. However, the vacuum gap is limited by the dielectric spacer thickness when EMT remains valid [150,161]. Furthermore, the frequency is limited to that of the optical phonon transition. Nevertheless, unlike that of the graphene-covered VACNT substrates, the heat flux enhancement between graphene-dielectric multilayers is significantly changed with chemical potential of the many graphene sheets.

5.4 Conclusion

Both VACNT and graphite substrates are shown to strongly enhance near-field thermal radiation mainly due to the existence of broadband hyperbolic modes. VACNT arrays are demonstrated to outperform graphite as well as other bulk materials, such as SiC, at any gap distances. It is found that low loss in permittivity can help enhance near-field heat transfer in HMMs with either Type I or Type II dispersion.

Due to the tunable semiconductor-like behavior of graphene, a pair of graphene sheets separated by a sub-micron vacuum gap allows evanescent wave tunneling in narrowband surface modes (SPP). Due to the intrinsic two hyperbolic bands and a low-frequency surface mode in VACNT, the hybridization with graphene SPP results in quite complex near-field transmission regimes. Graphene SPP does not improve the lower frequency hyperbolic mode, since the latter is supported by the symmetric SPP band of uncovered VACNT. This disruption is especially strong with increased chemical potential in graphene. On the other hand, in the higher frequency hyperbolic band that intrinsically contains fewer hyperbolic modes, strongly doped graphene allows increased number of near-unity transmission modes due to hybridization. Due to these two competing mechanisms, an optimal chemical potential value for the doped graphene sheets results in the greatest heat flux enhancement over uncovered VACNT. Depending

on the frequency of interest, the presence of graphene especially under high doping can drastically increase the penetration depth. The VACNT substrate thickness should be several tens to one hundred micrometers in order to be considered semi-infinite.

Graphene-dielectric multilayers can significantly improve near-field transport over similar Type II hyperbolic substrates such as graphite. Because graphene is tunable, the frequency transitions between positive and single-negative (hyperbolic) permittivity. Increasing chemical potential shifts this frequency higher, which increases broadband evanescent wave tunneling, but also reduces the photon transmission in the far field. The multitude of graphene sheets allow for significant changes to heat transport when biasing is varied. These works on near-field tunneling between hyperbolic substrates may be beneficial to more efficient local thermal management and near-field thermal imaging.

CHAPTER 6

CONCLUSIONS AND RECOMMENDATIONS

This dissertation has demonstrated the salient hallmarks of two types of graphite-based nanomaterials applied to surface coating or thin film thermal radiation modification. The defining characteristic, hyperbolic dispersion is predicted in broad infrared wavelength regions in both VACNT arrays and graphene-embedded multilayers. In far-field optics of infrared waves, hyperbolic dispersion of a certain type suggests unconventional angle of refraction and loss-assisted transmission. VACNT arrays behave like collimating fibers, and by controlling the large-scale tilted growth of CNT, allow transmission along the filament axis. Furthermore, voltage modulation of graphene-dielectric multilayers allows switching between positive and negative refraction. In the near field, hyperbolic substrates permit photon tunneling in steeply evanescent wavevectors. Due to this effect, the radiative heat flux between nanoscale-sized vacuum gaps is enhanced vastly, promoting contactless thermal conservation of radiating TPV components.

6.1 Conclusions of Major Works

VACNT arrays are effective absorbing radiative surface coatings in the near- to mid-infrared due to the refractive index matching. Beyond the interband transition at the wavelength near 100 μm, free electron contribution dominates and reflectance is high. Considering the fabrication conditions for VACNT arrays, low packing density and high degree of alignment can reduce surface reflection. For thin film CNT arrays, the radiative penetration depth is high enough to transmit rays with some internal reflection or

interference effect in the near- to mid-infrared wavelengths. Therefore, absorptance is significantly reduced in thin VACNT coatings. Therefore, the thickness of VACNT coatings is ideally greater than the characteristic incidence wavelength. Broadband hemispherical absorption in the near- to mid-infrared suggests suitable blackbody surface substitution.

In VACNT thin films, the transmission profiles are demonstrated in two far-infrared wavelength regions defined by Type I hyperbolic dispersion. The dielectric permittivity in those regions permits counter-intuitive loss-enhanced transmission, which results in high penetration depth and good transmittance through subwavelength thin films. The refraction angle in VACNT is near normal for all incidence angles, and is more streamlined when the alignment factor is improved. Tilting of the VACNT array (TACNT) in the plane of incidence confirms the hypothesis that refraction is along the shifted optical axis, confirmed by tracing the Poynting vectors. However, heavily tilted arrays may not be able to support this collimation effect for all incidence angles. Due to the reduced surface reflectance and increased penetration depth when the incidence radiation is co-linear with the angle of tilting, the thin film radiative transmittance is selective. In VACNT or TACNT thin films thinner than the characteristic wavelengths in the hyperbolic regime, the transmission is favorable toward the alignment of the optical axis, thereby applicable to beam collimators, couplers, and spatial filters or polarizers.

Graphene sheets have transitioning conductive to semi-conductive characteristics in the mid- to far-infrared wavelength regimes. Moreover, the transition threshold is tunable via voltage gating or adjustment of the chemical potential. Graphene embedded in periodic and uniform-sized dielectric layers such as hexagonal boron nitride

demonstrates tunable and unconventional optics in the infrared. Depending on the thickness of the dielectric layers and therefore the filling ratio, transmission through the multilayer 2 µm-thick thin film is modulated. Since the traditionally oriented graphene-dielectric multilayers are Type II hyperbolic due to the negative permittivity contribution in the direction along the graphene sheets, no negative angle of refraction is observed. When the multilayers are rotated such that the graphene sheets are perpendicular to the medium surface (side-incidence), the energy streamlines under favorable conditions illustrate negative angle of refraction with good transmittance. These conditions are increased chemical potential and incidence radiation in the far-infrared. The tunable conductivity in graphene allows variation between positive and negative angle of refraction, giving this work promise in infrared imaging and filtering applications.

The study of the semiconductor metamaterials offered understanding of the constraints in using EMT to model radiative properties. Generally, metal-dielectric multilayers suffer from high attenuation and may not be able to sustain coherent waves throughout the entire thin film. To remedy this, it is recommended to fabricate layers thin as possible. Furthermore, the investigation of the gradient multilayers suggests that thin layers near the incidence and outgoing surfaces are beneficial to anti-reflection. However, with limits on deposition methods, semiconductor multilayers can be tuned to have dielectric functions that demonstrate low loss while having negative refractive index. Such layers should contain small magnitudes in the permittivity for both doped and undoped semiconductor constituents.

As the vacuum gap between bodies of different temperature grows smaller, the heat flux between the body surfaces exceeds that of blackbodies. The implementation of

111

hyperbolic substrates such as graphite and VACNT has enhanced the heat flux over traditional bodies such as silicon carbide. Graphite substrates contain two broadband Type II hyperbolic regimes. The cutoff wavevector unique to Type II hyperbolic dispersion limits the contribution toward photon tunneling. Nevertheless, the near-unity transmission coefficient in evanescent wavevectors allows for enhanced near-field heat flux. Between VACNT substrates, the hyperbolic dispersion is aided by SPP coupling between surface waves in the double-negative permittivity regime. In effect, photon tunneling is permitted in very deep evanescent waves. The performance offered by VACNT exceeds that of graphite due to the smaller contribution of the imaginary component of the Fresnel reflection coefficient.

By covering VACNT substrates with graphene sheets, the narrowband SPP coupling modes are a significant mechanism for photon tunneling. The SPP modes hybridize with the hyperbolic modes found in VACNT, meaning that the near-field transmission coefficient contours exhibit smearing of both contributions. This hybridization does not necessarily mean improved photon tunneling. In the low frequency regimes, the SPP mode present in uncovered VACNT becomes suppressed. Therefore, the spectral heat flux is improved in just the high frequencies, especially for graphene with high chemical potentials. The chemical potential modulation of graphene allows for improved or retarded heat flux enhancement compared to uncovered VACNT. The enhancement in vacuum gaps greater than 100 nm is only marginally improved over that of uncovered VACNT. The absorption due to graphene is explained using the near-field Poynting vector, which also gives the photon penetration depth. The penetration depth serves as criterion for semi-infinite VACNT substrate thickness. Graphene-covered

VACNT may be considered as heat flux gating devices or frequency-selective radiative thermal rectifiers.

By bringing in multiple layers of graphene between layers of dielectrics, the near-field enhancement due to hyperbolic modes can be tuned via graphene biasing. Oriented with the graphene sheets in parallel to the surfaces, the Type II hyperbolic mode is similar to those found in graphite. However, the boundary of hyperbolic modes can be tuned by changing the chemical potential of graphene. The heat flux enhancement over that of blackbody indeed trumps graphite in most gap distances in the near field. However, too highly doped graphene may present poor surface properties in the far field. An anomalous peak-like optimal enhancement of near-field heat transport in relation to the graphene chemical potential is identified.

6.2 Recommendations for Future Research

Possible works extending this dissertation can include: Modeling of radiative properties of single-walled carbon nanotube arrays using the known models of graphene conductivity. The effects of deformation, misalignment, and chirality in and between CNT can be studied using first principle simulations. Interesting graphene-based geometries can be probed, such as folded graphene, carbon nanoboxes, and exfoliated surface nanopetals. Graphene multilayers with various dielectric host materials both isotropic and anisotropic can be explored. The validity of EMT may be probed by comparing the energy streamlines and radiative properties of traditional metal-dielectric layers to those obtained by TMM. Radiative properties can be obtained using finite-difference time domain software. For microelectronic packaging analysis, the results obtained in this dissertation can be combined with thermal conduction models.

Experimental verification is needed to understand response of fabricated carbon-nanomaterials. VACNT can be grown with varying coating thickness, to observe the interference effect and loss of absorption. Measurements can be performed on a Fourier transform infrared spectrometer, which determines the reflectance and transmittance from near- to mid-infrared in adjustable incidence angles. Growth of TACNT can be attempted, by constructing an angled substrate panel in a plasma-enhanced CVD process. Graphene-embedded dielectric structures have already been realized, but not in large quantities described by the multilayers. To enable wide crystals for side-incidence optics, graphene and hexagonal boron nitride may be grown together from a surface. The near-field thermal radiation measurements can be performed using a heat flux meter within a cryogenic chamber. Despite some challenges of near-field nanoscale devices, it is worth nothing that there has been significant progress on experimental investigation of near-field radiation in the recent years. Further study of near-field thermo-electric effects are worth pursuing for the advancement of scanning probe microscopy, solar energy collection, thermal circuits, and many other applications.

APPENDIX A

KRAMERS-KRONIG VALIDATIONS

The wavelength for which graphite is defined is between 0.23 μm and 1200 μm. Equivalently, this is between 43,500 cm^{-1} and 8.33 cm^{-1}. Ideally, the frequency is defined for both higher and lower bounds.
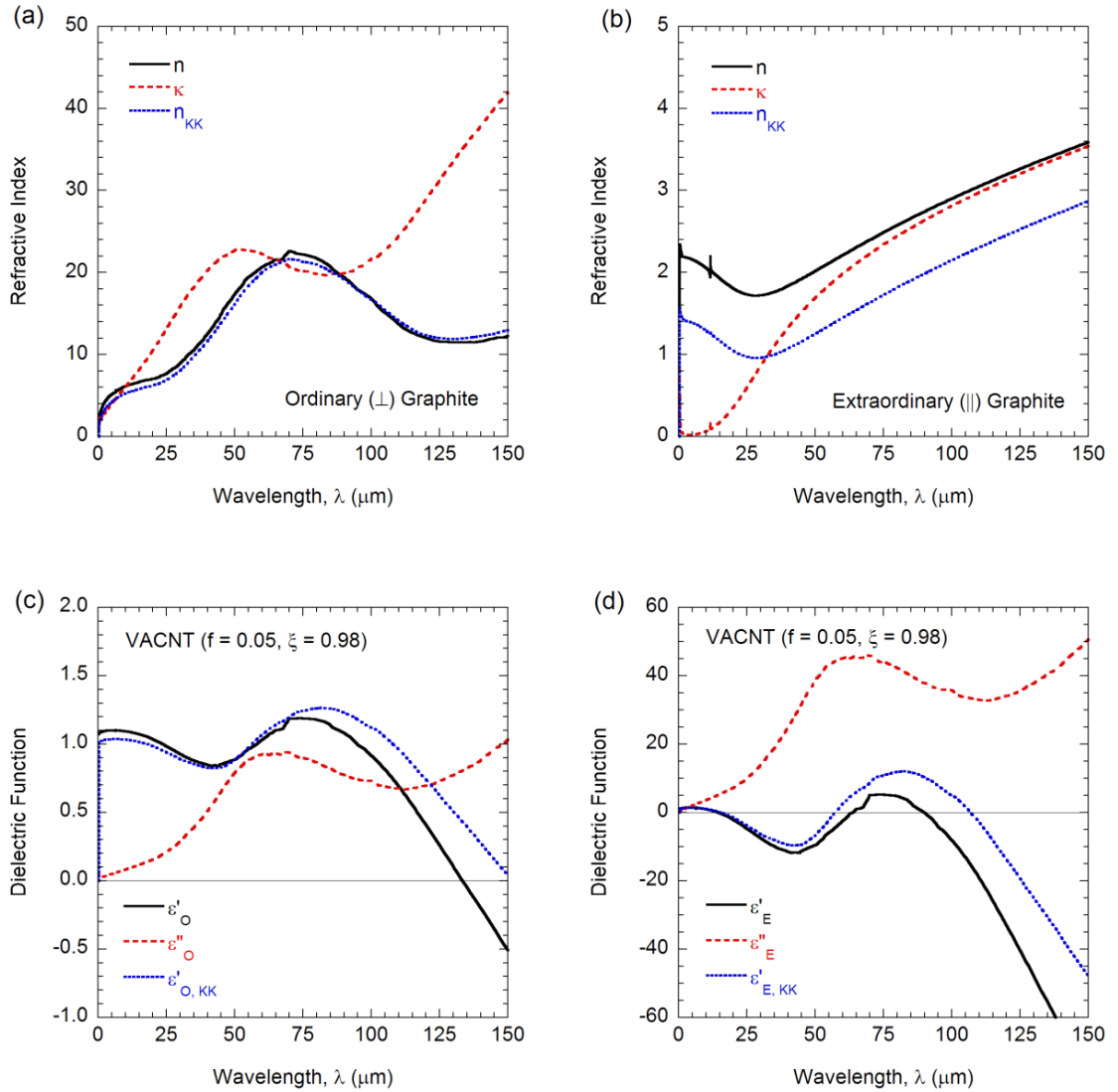
Figure A.1 K-K transformation of graphite refractive indices in (a) ordinary and (b) extraordinary directions. The transformation plots of VACNT dielectric function at default filling ratio and alignment in (c) ordinary and (d) extraordinary directions.

The refractive index for graphite matches well for the ordinary direction. However, for the extraordinary direction, there is some disagreement or offset. The difficulty of measuring the extraordinary (parallel to optical axis/perpendicular to the surface) component reflectance is described in Nemanich, Lucovsky and Solin (1977) *Solid State Communications*. Comparing the real component of the VACNT dielectric function and that determined from the K-K relation demonstrates the validity of the EMT formulations. The K-K calculations match well within a centered wavelength range. The deviations at both long and short wavelengths may be due to the limited defined wavelengths for graphite.

APPENDIX B

GRAPHENE CONDUCTIVITY MODELS

The conductivity of graphene was measured by Z.Q. Li and colleagues (Ref. [61]) by reflection, transmission and ellipsometric measurements of a graphene-silicon multilayer structure. The temperature was held in cryogenic conduction (45 K). The gate capacitance through the silicon is $C_g = 115$ aF μm^{-2}, which relates the voltage gating (V) to the carrier concentration,

$$N = C_g V / q \tag{B.1}$$

The chemical potential (Fermi level) can be related to the carrier concentration by the following relationship,

$$\mu = \hbar v_F \sqrt{\pi N} \tag{B.2}$$

where the Fermi velocity is $v_F = 1.1 \times 10^6$ m/s. Figure B.1 plots the real and imaginary parts of the graphene conductivity against the wavenumber (ν). Some differences between measured and modeled conductivity is due to the purity and electron mobility that varies from sample to sample [124,181]. The shape due to the interband transition suggests good matching between the conductivity models to measured data. To find the interband transition, where the imaginary component of the conductivity is minimum and the real component is in the vicinity of 0.5 (through a Heaviside-like function), the frequency is $\omega_{inter} = 2\mu$. Figure B.2 plots only the modeled conductivity in terms of the angular frequency, in which the interband transition is only observed for graphene with chemical potential of 0.1 eV.
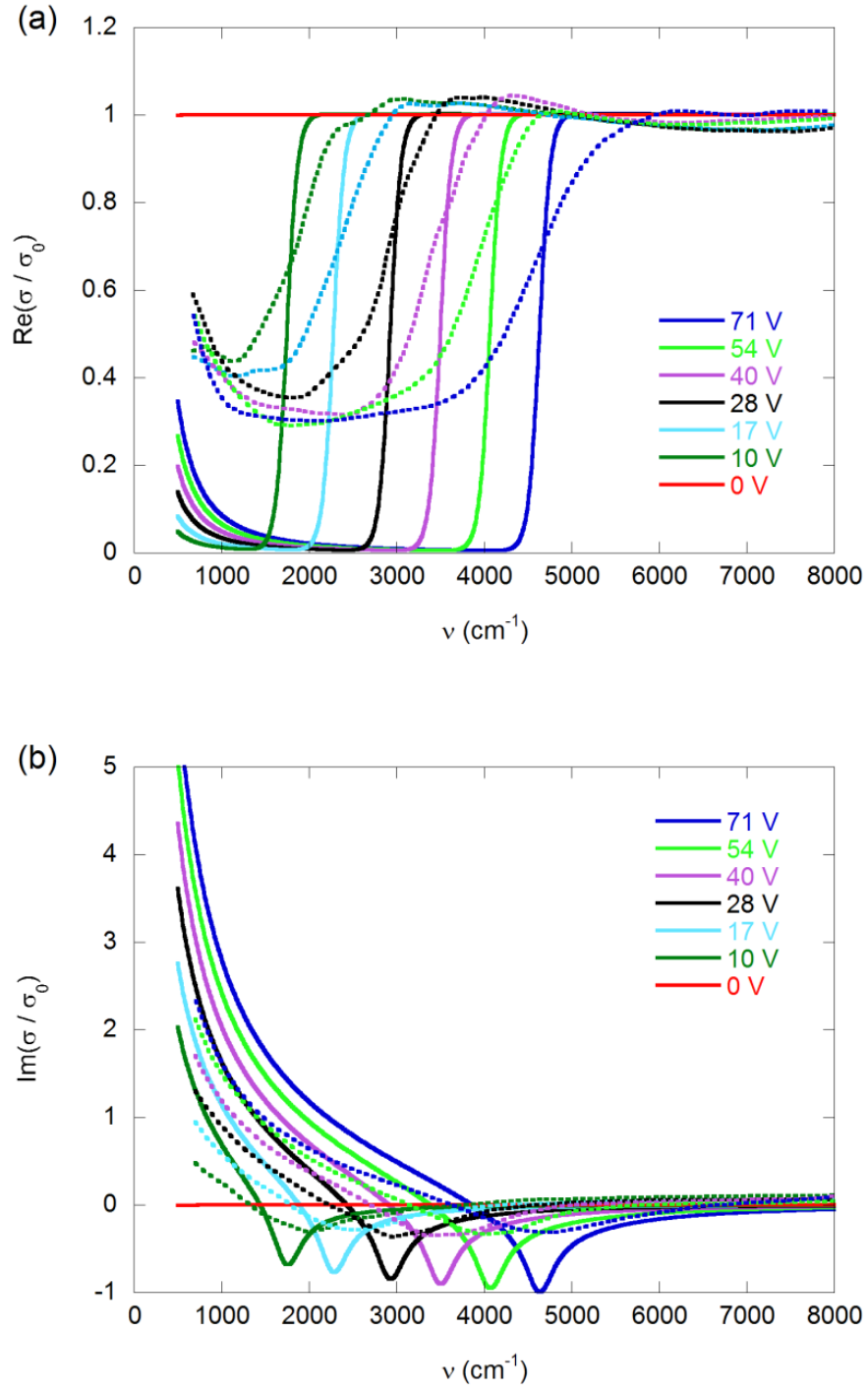
Figure B.1 Modeled (solid) versus measured (dotted) conductivity of graphene, taken from Ref. [61]. The real part is shown in (a) and the imaginary in (b).
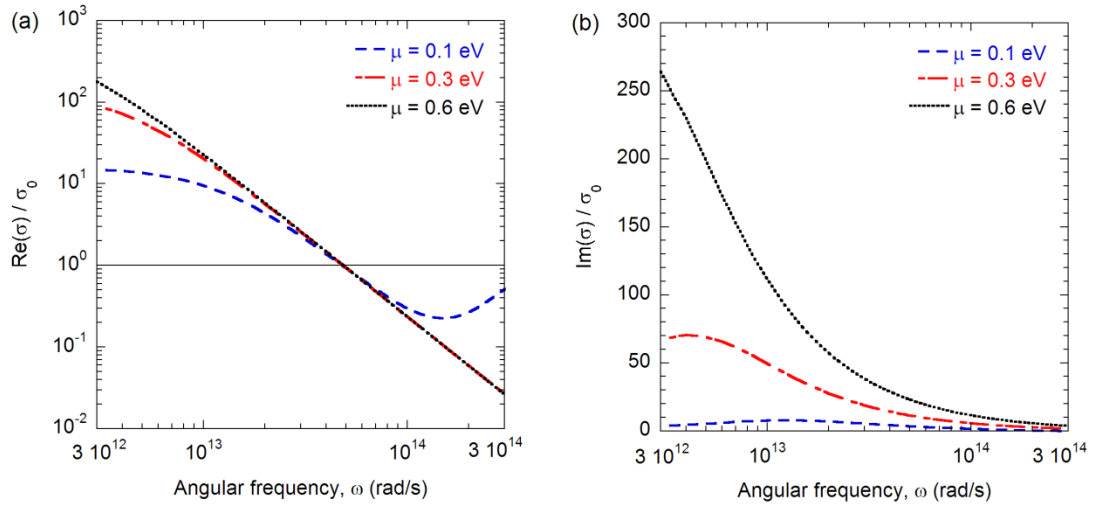
Figure B.2 Modeled graphene conductivity in terms of the angular frequency.

REFERENCES

[1]   Barber DJ, Freestone IC. An Investigation of the Colour of the Lycurgus Cup by Analytical Transmission Electron Microscopy. Archaeometry. 1990;32:33-45.

[2]   Mie G. Beiträge Zur Optik Trüber Medien, Speziell Kolloidaler Metallösungen. Annalen der Physik. 1908;330:377-445.

[3]   Zhang ZM. Nano/Microscale Heat Transfer. New York: McGraw-Hill; 2007.

[4]   Michalet X, Pinaud FF, Bentolila LA, Tsay JM, Doose S, Li JJ, et al. Quantum Dots for Live Cells, in Vivo Imaging, and Diagnostics. Science. 2005;307:538-44.

[5]   Gao X, Cui Y, Levenson RM, Chung LWK, Nie S. In Vivo Cancer Targeting and Imaging with Semiconductor Quantum Dots. Nat. Biotech. 2004;22:969-76.

[6]   Law M, Greene LE, Johnson JC, Saykally R, Yang P. Nanowire Dye-Sensitized Solar Cells. Nat. Mater. 2005;4:455-9.

[7]   Garnett E, Yang P. Light Trapping in Silicon Nanowire Solar Cells. Nano Lett. 2010;10:1082-7.

[8]   Mor GK, Shankar K, Paulose M, Varghese OK, Grimes CA. Use of Highly-Ordered Tio2 Nanotube Arrays in Dye-Sensitized Solar Cells. Nano Lett 2006;6:215-8.

[9]   Fleming J, Lin S, El-Kady I, Biswas R, Ho K. All-Metallic Three-Dimensional Photonic Crystals with a Large Infrared Bandgap. Nature. 2002;417:52-5.

[10]   Seager CH, Sinclair MB, Fleming JG. Accurate Measurements of Thermal Radiation from a Tungsten Photonic Lattice. Appl. Phys. Lett. 2005;86:244105.

[11]   Lee B, Fu C, Zhang Z. Coherent Thermal Emission from One-Dimensional Photonic Crystals. Appl. Phys. Lett. 2005;87:071904.

[12]   Basu S, Zhang Z, Fu C. Review of near-Field Thermal Radiation and Its Application to Energy Conversion. International Journal of Energy Research. 2009;33:1203-32.

[13]   Baughman RH, Zakhidov AA, de Heer WA. Carbon Nanotubes--the Route toward Applications. Science. 2002;297:787-92.

[14]   Dresselhaus MS, Dresselhaus G, Eklund PC, Rao AM. Carbon Nanotubes. In: Andreoni W, editor. The Physics of Fullerene-Based and Fullerene-Related Materials: Springer Netherlands; 2000. p. 331-79.

120

[15]   McEuen PL. Nanotechnology: Carbon-Based Electronics. Nature. 1998;393:15-7.

[16]   Avouris P, Chen Z, Perebeinos V. Carbon-Based Electronics. Nat. Nanotech. 2007;2:605-15.

[17]   Low T, Avouris P. Graphene Plasmonics for Terahertz to Mid-Infrared Applications. ACS Nano. 2014;8:1086-101.

[18]   Kroto HW, Heath JR, O'Brien SC, Curl RF, Smalley RE. C60: Buckminsterfullerene. Nature. 1985;318:162-3.

[19]   Iijima S, Ichihashi T. Single-Shell Carbon Nanotubes of 1-nm Diameter. Nature. 1993;363:603-5.

[20]   Yu M-F, Lourie O, Dyer MJ, Moloni K, Kelly TF, Ruoff RS. Strength and Breaking Mechanism of Multiwalled Carbon Nanotubes under Tensile Load. Science. 2000;287:637-40.

[21]   deHeer WA, Chatelain A, Ugarte D. A Carbon Nanotube Field-Emission Electron Source. Science. 1995;270:1179-80.

[22]   Collins PG, Avouris P. Nanotubes for Electronics. Sci. Amer. 2000;283:62-9.

[23]   Tans SJ, Verschueren ARM, Dekker C. Room-Temperature Transistor Based on a Single Carbon Nanotube. Nature. 1998;393:49-52.

[24]   Rueckes T, Kim K, Joselevich E, Tseng GY, Cheung C-L, Lieber CM. Carbon Nanotube-Based Nonvolatile Random Access Memory for Molecular Computing. Science. 2000;289:94-7.

[25]   Liu C, Fan YY, Liu M, Cong HT, Cheng HM, Dresselhaus MS. Hydrogen Storage in Single-Walled Carbon Nanotubes at Room Temperature. Science. 1999;286:1127-9.

[26]   Coleman JN, Khan U, Blau WJ, Gun'ko YK. Small but Strong: A Review of the Mechanical Properties of Carbon Nanotube–Polymer Composites. Carbon. 2006;44:1624-52.

[27]   Bachtold A, Hadley P, Nakanishi T, Dekker C. Logic Circuits with Carbon Nanotube Transistors. Science. 2001;294:1317-20.

[28]   Pop E, Mann D, Wang Q, Goodson K, Dai H. Thermal Conductance of an Individual Single-Wall Carbon Nanotube above Room Temperature. Nano Lett. 2006;6:96-100.

[29]   deHeer WA, Bacsa WS, Châtelain A, Gerfin T, Humphrey-Baker R, Forro L, et al. Aligned Carbon Nanotube Films: Production and Optical and Electronic Properties. Science. 1995;268:845-7.

[30]   Zhang ZM, Ye H. Measurements of Radiative Properties of Engineered Micro-/Nanostructures. Annu. Rev. of Heat Trans. 2013;16.

[31]   Yang Z-P, Ci L, Bur JA, Lin S-Y, Ajayan PM. Experimental Observation of an Extremely Dark Material Made by a Low-Density Nanotube Array. Nano Lett. 2008;8:446-51.

[32]   Yang Z-P, Hsieh M-L, Bur JA, Ci L, Hanssen LM, Wilthan B, et al. Experimental Observation of Extremely Weak Optical Scattering from an Interlocking Carbon Nanotube Array. Appl. Opt. 2011;50:1850-5.

[33]   Mizuno K, Ishii J, Kishida H, Hayamizu Y, Yasuda S, Futaba DN, et al. A Black Body Absorber from Vertically Aligned Single-Walled Carbon Nanotubes. Proc. Nat. Acad. Sci. (PNAS). 2009;106:6044-7.

[34]   Tarasov M, Svensson J, Kuzmin L, Campbell EE. Carbon Nanotube Bolometers. Appl. Phys. Lett. 2007;90:163503-.

[35]   Itkis ME, Borondics F, Yu A, Haddon RC. Bolometric Infrared Photoresponse of Suspended Single-Walled Carbon Nanotube Films. Science. 2006;312:413-6.

[36]   Lehman J, Sanders A, Hanssen L, Wilthan B, Zeng J, Jensen C. Very Black Infrared Detector from Vertically Aligned Carbon Nanotubes and Electric-Field Poling of Lithium Tantalate. Nano Lett. 2010;10:3261-6.

[37]   Lehman JH, Engtrakul C, Gennett T, Dillon AC. Single-Wall Carbon Nanotube Coating on a Pyroelectric Detector. Appl. Opt. 2005;44:483-8.

[38]   Lehman JH, Hurst KE, Radojevic AM, Dillon AC, Osgood RM, Jr. Multiwall Carbon Nanotube Absorber on a Thin-Film Lithium Niobate Pyroelectric Detector. Opt. Lett. 2007;32:772-4.

[39]   Lenert A, Bierman DM, Nam Y, Chan WR, Celanovic I, Soljacic M, et al. A Nanophotonic Solar Thermophotovoltaic Device. Nat. Nanotech. 2014;9:126-30.

[40]   Chen C, Lu Y, Kong ES, Zhang Y, Lee S-T. Nanowelded Carbon-Nanotube-Based Solar Microcells. Small. 2008;4:1313-8.

[41]   Ren L, Pint CL, Booshehri LG, Rice WD, Wang X, Hilton DJ, et al. Carbon Nanotube Terahertz Polarizer. Nano Lett 2009;9:2610-3.

[42]   Wu Z, Chen Z, Du X, Logan JM, Sippel J, Nikolou M, et al. Transparent, Conductive Carbon Nanotube Films. Science. 2004;305:1273-6.

[43]   Zhang M, Fang S, Zakhidov AA, Lee SB, Aliev AE, Williams CD, et al. Strong, Transparent, Multifunctional, Carbon Nanotube Sheets. Science. 2005;309:1215-9.

[44]   Maeng I, Kang C, Oh SJ, Son J-H, An KH, Lee YH. Terahertz Electrical and Optical Characteristics of Double-Walled Carbon Nanotubes and Their Comparison with Single-Walled Carbon Nanotubes. Appl. Phys. Lett. 2007;90:051914.

[45]   Maine S, Koechlin C, Rennesson S, Jaeck J, Salort S, Chassagne B, et al. Complex Optical Index of Single Wall Carbon Nanotube Films from the near-Infrared to the Terahertz Spectral Range. Appl. Opt. 2012;51:3031-5.

[46]   Ugawa A, Rinzler AG, Tanner DB. Far-Infrared Gaps in Single-Wall Carbon Nanotubes. Phys. Rev. B. 1999;60:R11305-R8.

[47]   Bachilo SM, Strano MS, Kittrell C, Hauge RH, Smalley RE, Weisman RB. Structure-Assigned Optical Spectra of Single-Walled Carbon Nanotubes. Science. 2002;298:2361-6.

[48]   Kampfrath T, von Volkmann K, Aguirre CM, Desjardins P, Martel R, Krenz M, et al. Mechanism of the Far-Infrared Absorption of Carbon-Nanotube Films. Phys. Rev. Lett. 2008;101:267403.

[49]   Paul MJ, Kuhta NA, Tomaino JL, Jameson AD, Maizy LP, Sharf T, et al. Terahertz Transmission Ellipsometry of Vertically Aligned Multi-Walled Carbon Nanotubes. Appl. Phys. Lett. 2012;101:111107.

[50]   Wang XJ, Flicker JD, Lee BJ, Ready WJ, Zhang ZM. Visible and near-Infrared Radiative Properties of Vertically Aligned Multi-Walled Carbon Nanotubes. Nanotech. 2009;20:215704.

[51]   Wang XJ, Wang LP, Adewuyi OS, Cola BA, Zhang ZM. Highly Specular Carbon Nanotube Absorbers. Appl. Phys. Lett. 2010;97:163116.

[52]   Novoselov KS, Geim AK, Morozov SV, Jiang D, Zhang Y, Dubonos SV, et al. Electric Field Effect in Atomically Thin Carbon Films. Science. 2004;306:666-9.

[53]   Schwierz F. Graphene Transistors. Nat. Nanotech. 2010;5:487-96.

[54]   Schedin F, Geim AK, Morozov SV, Hill EW, Blake P, Katsnelson MI, et al. Detection of Individual Gas Molecules Adsorbed on Graphene. Nat. Mater. 2007;6:652-5.

[55]   Ahn J-H, Hong BH. Graphene for Displays That Bend. Nat. Nanotech. 2014;9:737-8.

[56]   Chen P-Y, Alù A. Atomically Thin Surface Cloak Using Graphene Monolayers. ACS Nano. 2011;5:5855-63.

[57]   Fang Z, Wang Y, Schlather AE, Liu Z, Ajayan PM, García de Abajo FJ, et al. Active Tunable Absorption Enhancement with Graphene Nanodisk Arrays. Nano Lett. 2013;14:299-304.

[58]   Gao W, Shi G, Jin Z, Shu J, Zhang Q, Vajtai R, et al. Excitation and Active Control of Propagating Surface Plasmon Polaritons in Graphene. Nano Lett. 2013;13:3698-702.

[59]   Liu C-H, Chang Y-C, Norris TB, Zhong Z. Graphene Photodetectors with Ultra-Broadband and High Responsivity at Room Temperature. Nat. Nanotech. 2014;9:273-8.

[60]   Vakil A, Engheta N. Transformation Optics Using Graphene. Science. 2011;332:1291-4.

[61]   Li ZQ, Henriksen EA, Jiang Z, Hao Z, Martin MC, Kim P, et al. Dirac Charge Dynamics in Graphene by Infrared Spectroscopy. Nat. Phys. 2008;4:532-5.

[62]   Mak KF, Sfeir MY, Wu Y, Lui CH, Misewich JA, Heinz TF. Measurement of the Optical Conductivity of Graphene. Phys. Rev. Lett. 2008;101:196405.

[63]   Falkovsky LA. Optical Properties of Graphene. J. of Phys: Conf. Ser. 2008;129:012004.

[64]   Jablan M, Buljan H, Soljačić M. Plasmonics in Graphene at Infrared Frequencies. Phys. Rev. B. 2009;80:245435.

[65]   Alaee R, Farhat M, Rockstuhl C, Lederer F. A Perfect Absorber Made of a Graphene Micro-Ribbon Metamaterial. Opt. Exp. 2012;20:28017-24.

[66]   Liu X, Zhao B, Zhang Z. Blocking-Assisted Infrared Transmission of Subwavelength Metallic Gratings by Graphene. J. Opt. 2015;17:035004.

[67]   Othman MAK, Guclu C, Capolino F. Graphene-Based Tunable Hyperbolic Metamaterials and Enhanced near-Field Absorption. Opt. Exp. 2013;21:7614-32.

[68]   Nefedov IS, Valaginnopoulos CA, Melnikov LA. Perfect Absorption in Graphene Multilayers. J. Opt. 2013;15:114003.

[69]   Iorsh IV, Mukhin IS, Shadrivov IV, Belov PA, Kivshar YS. Hyperbolic Metamaterials Based on Multilayer Graphene Structures. Phys. Rev. B. 2013;87:075416.

[70]   Liu Z, Song L, Zhao S, Huang J, Ma L, Zhang J, et al. Direct Growth of Graphene/Hexagonal Boron Nitride Stacked Layers. Nano Lett. 2011;11:2032-7.

[71]   Xue J, Sanchez-Yamagishi J, Bulmash D, Jacquod P, Deshpande A, Watanabe K, et al. Scanning Tunnelling Microscopy and Spectroscopy of Ultra-Flat Graphene on Hexagonal Boron Nitride. Nat. Mater. 2011;10:282-5.

[72]   Woessner A, Lundeberg MB, Gao Y, Principi A, Alonso-González P, Carrega M, et al. Highly Confined Low-Loss Plasmons in Graphene–Boron Nitride Heterostructures. Nat. Mater. 2015;14:421-5.

[73]   Xu B-z, Gu C-q, Li Z, Niu Z-y. A Novel Structure for Tunable Terahertz Absorber Based on Graphene. Opt. Exp. 2013;21:23803-11.

[74]   Zhu B, Ren G, Zheng S, Lin Z, Jian S. Nanoscale Dielectric-Graphene-Dielectric Tunable Infrared Waveguide with Ultrahigh Refractive Indices. Opt. Exp. 2013;21:17089-96.

[75]   Pendry JB. Negative Refraction Makes a Perfect Lens. Phys. Rev. Lett. 2000;85:3966-9.

[76]   Poddubny A, Iorsh I, Belov P, Kivshar Y. Hyperbolic Metamaterials. Nat. Photon. 2013;7:948-57.

[77]   Cai W, Shalaev VM. Optical Metamaterials: Springer; 2010.

[78]   Shalaev VM. Optical Negative-Index Metamaterials. Nat. Phot. 2007;1:41-8.

[79]   Fang N, Lee H, Sun C, Zhang X. Sub–Diffraction-Limited Optical Imaging with a Silver Superlens. Science. 2005;308:534-7.

[80]   Liu XL, Zhang ZM. Metal-Free Low-Loss Negative Refraction in the Mid-Infrared Region. Appl. Phys. Lett. 2013;103.

[81]   Liu Y, Bartal G, Zhang X. All-Angle Negative Refraction and Imaging in a Bulk Medium Made of Metallic Nanowires in the Visible Region. Opt. Exp. 2008;16:15439-48.

[82]   Sun L, Feng S, Yang X. Loss Enhanced Transmission and Collimation in Anisotropic Epsilon-near-Zero Metamaterials. Appl. Phys. Lett. 2012;101.

[83]   Xu T, Agrawal A, Abashin M, Chau KJ, Lezec HJ. All-Angle Negative Refraction and Active Flat Lensing of Ultraviolet Light. Nature. 2013;497:470-4.

[84]   Guo Y, Cortes CL, Molesky S, Jacob Z. Broadband Super-Planckian Thermal Emission from Hyperbolic Metamaterials. Appl. Phys. Lett. 2012;101.

[85]   Cai W, Chettiar UK, Kildishev AV, Shalaev VM. Optical Cloaking with Metamaterials. Nat. Photon. 2007;1:224-7.

[86]   Lee BJ, Fu CJ, Zhang ZM. Coherent Thermal Emission from One-Dimensional Photonic Crystals. Appl. Phys. Lett. 2005;87:071904.

[87]   Lee BJ, Zhang ZM. Design and Fabrication of Planar Multilayer Structures with Coherent Thermal Emission Characteristics. J.Appl. Phys. 2006;100:063529.

[88]   Bright T, Wang L, Zhang Z. Performance of near-Field Thermophotovoltaic Cells Enhanced with a Backside Reflector. J. Heat Trans. 2014;136:062701.

[89]   Guo Y, Jacob Z. Thermal Hyperbolic Metamaterials. Opt. Exp. 2013;21:15014-9.

[90]   Nefedov IS, Valagiannopoulos CA, Hashemi SM, Nefedov EI. Total Absorption in Asymmetric Hyperbolic Media. Sci. Rep. 2013;3.

[91]   García-Vidal FJ, Pitarke JM, Pendry JB. Effective Medium Theory of the Optical Properties of Aligned Carbon Nanotubes. Phys. Rev. Lett. 1997;78:4289-92.

[92]   Yeh P. Optical Waves in Layered Media: Wiley; 2005.

[93]   Knoesen A, Moharam M, Gaylord T. Electromagnetic Propagation at Interfaces and in Waveguides in Uniaxial Crystals. Appl. Phys. B. 1985;38:171-8.

[94]   Smith GB. Effective Medium Theory and Angular Dispersion of Optical Constants in Films with Oblique Columnar Structure. Opt. Commun. 1989;71:279-84.

[95]   Sun J, Zhou J, Li B, Kang F. Indefinite Permittivity and Negative Refraction in Natural Material: Graphite. Appl. Phys. Lett. 2011;98.

[96]   Baker RTK. Catalytic Growth of Carbon Filaments. Carbon. 1989;27:315-23.

[97]   Betzig E, Chichester RJ. Single Molecules Observed by near-Field Scanning Optical Microscopy. Science. 1993;262:1422-5.

[98]   Inouye Y, Kawata S. Near-Field Scanning Optical Microscope with a Metallic Probe Tip. Opt. Lett. 1994;19:159-61.

[99]   Greffet J-J, Carminati R. Image Formation in near-Field Optics. Progress in Surface Science. 1997;56:133-237.

[100]   Chimmalgi A, Grigoropoulos C, Komvopoulos K. Surface Nanostructuring by Nano-/Femtosecond Laser-Assisted Scanning Force Microscopy. J. Appl. Phys. 2005;97:104319.

[101]   Mcleod E, Arnold CB. Subwavelength Direct-Write Nanopatterning Using Optically Trapped Microspheres. Nat. Nanotech. 2008;3:413-7.

[102]   Narayanaswamy A, Chen G. Surface Modes for near Field Thermophotovoltaics. Appl. Phys. Lett. 2003;82:3544-6.

[103]   Miller OD, Johnson SG, Rodriguez AW. Effectiveness of Thin Films in Lieu of Hyperbolic Metamaterials in the near Field. Phys. Rev. Lett. 2014;112:157402.

[104]   Joulain K, Carminati R, Mulet J-P, Greffet J-J. Definition and Measurement of the Local Density of Electromagnetic States Close to an Interface. Phys. Rev. B. 2003;68:245405.

[105]   Laroche M, Carminati R, Greffet J-J. Near-Field Thermophotovoltaic Energy Conversion. Journal of Appl. Phys. 2006;100:063704.

[106]   Shchegrov AV, Joulain K, Carminati R, Greffet J-J. Near-Field Spectral Effects Due to Electromagnetic Surface Excitations. Phys. Rev. Lett. 2000;85:1548.

[107]   Liu X, Wang L, Zhang ZM. Near-Field Thermal Radiation: Recent Progress and Outlook. Nano. and Micro. Thermo. Eng. 2015;19:98-126.

[108]   Chapuis P-O, Volz S, Henkel C, Joulain K, Greffet J-J. Effects of Spatial Dispersion in near-Field Radiative Heat Transfer between Two Parallel Metallic Surfaces. Phys. Rev. B. 2008;77:035431.

[109]   Francoeur M, Mengüç MP, Vaillon R. Near-Field Radiative Heat Transfer Enhancement Via Surface Phonon Polaritons Coupling in Thin Films. Appl. Phys. Lett. 2008;93:043109.

[110]   In: Palik ED, editor. Handbook of Optical Constants of Solids. Burlington: Academic Press; 1997. p. 3-9.

[111]   Smith DY. Dispersion Theory, Sum Rules, and Their Application to the Analysis of Optical Data. In: Palik ED, editor. Handbook of Optical Constants of Solids,. San Diego: Academic Press; 1985. p. 35-68.

[112]   Sato Y. Optical Study of Electronic Structure of Graphite. J. Phys. Soc. Japan. 1968;24:489-92.

[113]   Philipp HR. Infrared Optical Properties of Graphite. Phys. Rev. B. 1977;16:2896-900.

[114] Kuzmenko AB, van Heumen E, Carbone F, van der Marel D. Universal Optical Conductance of Graphite. Phys. Rev. Lett. 2008;100:117401.

[115] Venghaus H. Infrared Reflectance and Dielectric Properties of Pyrolytic Graphite for E ∥ C Polarization. Phys. Status Solidi B. 1977;81:221-5.

[116] Nemanich RJ, Lucovsky G, Solin SA. Infrared Active Optical Vibrations of Graphite. Sol. State Commun. 1977;23:117-20.

[117] Borghesi A, Guizzetti G. Graphite (C). In: Palik ED, editor. Handbook of Optical Constants of Solids Ii. San Diego: Academic Press; 1991. p. 449-60.

[118] Taft EA, Philipp HR. Optical Properties of Graphite. Phys. Rev. 1965;138:A197-A202.

[119] Draine BT, Lee HM. Optical-Properties of Interstellar Graphite and Silicate Grains. Astrophys. J. 1984;285:89-108.

[120] Li X, Cai W, An J, Kim S, Nah J, Yang D, et al. Large-Area Synthesis of High-Quality and Uniform Graphene Films on Copper Foils. Science. 2009;324:1312-4.

[121] Dean CR, Young AF, MericI, LeeC, WangL, SorgenfreiS, et al. Boron Nitride Substrates for High-Quality Graphene Electronics. Nat. Nanotech. 2010;5:722-6.

[122] Xu Y, He KT, Schmucker SW, Guo Z, Koepke JC, Wood JD, et al. Inducing Electronic Changes in Graphene through Silicon (100) Substrate Modification. Nano Lett. 2011;11:2735-42.

[123] Tan YW, Zhang Y, Bolotin K, Zhao Y, Adam S, Hwang EH, et al. Measurement of Scattering Rate and Minimum Conductivity in Graphene. Phys. Rev. Lett. 2007;99:246803.

[124] Bolotin KI, Sikes KJ, Jiang Z, Klima M, Fudenberg G, Hone J, et al. Ultrahigh Electron Mobility in Suspended Graphene. Sol. State Commun. 2008;146:351-5.

[125] Nomura K, MacDonald AH. Quantum Transport of Massless Dirac Fermions. Phys. Rev. Lett. 2007;98:076602.

[126] Zhu W, Perebeinos V, Freitag M, Avouris P. Carrier Scattering, Mobilities, and Electrostatic Potential in Monolayer, Bilayer, and Trilayer Graphene. Phys. Rev. B. 2009;80:235402.

[127] Falkovsky LA, Pershoguba SS. Optical Far-Infrared Properties of a Graphene Monolayer and Multilayer. Phys. Rev. B. 2007;76:153410.

[128]   Lim M, Lee SS, Lee BJ. Near-Field Thermal Radiation between Graphene-Covered Doped Silicon Plates. Opt. Exp. 2013;21:22173-85.

[129]   Sachs B, Wehling TO, Katsnelson MI, Lichtenstein AI. Adhesion and Electronic Structure of Graphene on Hexagonal Boron Nitride Substrates. Phys. Rev. B. 2011;84:195414.

[130]   Dutta AK. Electrical Conductivity of Single Crystals of Graphite. Phys. Rev. 1953;90:187-92.

[131]   Kim D-H, Jang H-S, Kim C-D, Cho D-S, Yang H-S, Kang H-D, et al. Dynamic Growth Rate Behavior of a Carbon Nanotube Forest Characterized by in Situ Optical Growth Monitoring. Nano Lett. 2003;3:863-5.

[132]   Murakami Y, Chiashi S, Miyauchi Y, Hu M, Ogura M, Okubo T, et al. Growth of Vertically Aligned Single-Walled Carbon Nanotube Films on Quartz Substrates and Their Optical Anisotropy. Chem. Phys. Lett. 2004;385:298-303.

[133]   Puretzky AA, Geohegan DB, Jesse S, Ivanov IN, Eres G. In Situ Measurements and Modeling of Carbon Nanotube Array Growth Kinetics During Chemical Vapor Deposition. Appl. Phys. A. 2005;81:223-40.

[134]   Nishimura H, Minami N, Shimano R. Dielectric Properties of Single-Walled Carbon Nanotubes in the Terahertz Frequency Range. Appl. Phys. Lett. 2007;91:011108.

[135]   Itkis ME, Niyogi S, Meng ME, Hamon MA, Hu H, Haddon RC. Spectroscopic Study of the Fermi Level Electronic Structure of Single-Walled Carbon Nanotubes. Nano Lett. 2001;2:155-9.

[136]   de los Arcos T, Garnier MG, Oelhafen P, Seo JW, Domingo C, García-Ramos JV, et al. In Situ Assessment of Carbon Nanotube Diameter Distribution with Photoelectron Spectroscopy. Phys. Rev. B. 2005;71:205416.

[137]   Ye H, Wang XJ, Lin W, Wong CP, Zhang ZM. Infrared Absorption Coefficients of Vertically Aligned Carbon Nanotube Films. Appl. Phys. Lett. 2012;101:141909.

[138]   Wang XJ, Abell JL, Zhao YP, Zhang ZM. Angle-Resolved Reflectance of Obliquely Aligned Silver Nanorods. Appl. Opt. 2012;51:1521-31.

[139]   Rytov SM. Electromagnetic Properties of a Finely Stratified Medium. Sov. Phys. JETP. 1956;2:466.

[140]   Jacob Z, Kim J-Y, Naik G, Boltasseva A, Narimanov E, Shalaev V. Engineering Photonic Density of States Using Metamaterials. Appl. Phys. B. 2010;100:215-8.

[141] Cortes CL, Newman W, Molesky S, Jacob Z. Quantum Nanophotonics Using Hyperbolic Metamaterials. J. Opt. 2012;14:063001.

[142] Schilling J. Uniaxial Metallo-Dielectric Metamaterials with Scalar Positive Permeability. Phys. Rev. E. 2006;74:046618.

[143] Halevi P, Mendoza-Hernández A. Temporal and Spatial Behavior of the Poynting Vector in Dissipative Media: Refraction from Vacuum into a Medium. J. Opt. Soc. Am. 1981;71:1238-42.

[144] Lee BJ, Zhang ZM. Coherent Thermal Emission from Modified Periodic Multilayer Structures. J. Heat Trans. 2006;129:17-26.

[145] Zhang ZM, Fu CJ. Unusual Photon Tunneling in the Presence of a Layer with a Negative Refractive Index. Appl. Phys. Lett. 2002;80:1097-9.

[146] Zhang Z, Lee BJ. Lateral Shift in Photon Tunneling Studied by the Energy Streamline Method. Opt. Ex. 2006;14:9963-70.

[147] Fu CJ, Zhang ZM. Nanoscale Radiation Heat Transfer for Silicon at Different Doping Levels. Int. J. Heat and Mass Trans. 2006;49:1703-18.

[148] Rytov SM, Kravstov YA, Tatarskii VI. Priciples of Statistical Radiophysics. New York: Springer-Verlag; 1987.

[149] Biehs SA, Rousseau E, Greffet JJ. Mesoscopic Description of Radiative Heat Transfer at the Nanoscale. Phys. Rev. Lett. 2010;105:234301.

[150] Bright TJ, Liu XL, Zhang ZM. Energy Streamlines in near-Field Radiative Heat Transfer between Hyperbolic Metamaterials. Opt. Exp. 2014;22:A1112-A27.

[151] Lee JK, Kong JA. Dyadic Green's Functions for Layered Anisotropic Medium. Electromagnetics. 1983;3:111-30.

[152] Sipe JE. New Green-Function Formalism for Surface Optics. J. Opt. Soc. Am. B. 1987;4:481-9.

[153] Auslender M, Hava S. Scattering-Matrix Propagation Algorithm in Full-Vectorial Optics Ofmultilayer Grating Structures. Opt. Lett. 1996;21:1765-7.

[154] Francoeur M, Pinar Mengüç M, Vaillon R. Solution of near-Field Thermal Radiation in One-Dimensional Layered Media Using Dyadic Green's Functions and the Scattering Matrix Method. J. Quant. Spect. Rad. Trans. 2009;110:2002-18.

[155] Zhang RZ, Liu X, Zhang Z. Modeling the Optical and Radiative Properties of Vertically Aligned Carbon Nanotubes in the Infrared. J. Heat Trans. 2015:In Press.

[156] Zhang RZ, Zhang Z. Negative Refraction and Self-Collimation in the Far Infrared with Aligned Carbon Nanotube Films. J. Quant. Spect. Rad. Trans. 2015:In Press.

[157] Feng S. Loss-Induced Omnidirectional Bending to the Normal in Epsilon-near-Zero Metamaterials. Phys. Rev. Lett. 2012;108:193904.

[158] Born M, Wolf E. Principles of Optics. 7th ed. Cambridge, UK: Cambridge University Press; 1999.

[159] Hoffman AJ, Alekseyev L, Howard SS, Franz KJ, Wasserman D, Podolskiy VA, et al. Negative Refraction in Semiconductor Metamaterials. Nat. Mat. 2007;6:946-50.

[160] Edwards DF. Silicon (Si). In: Palik ED, editor. Handbook of Optical Constants of Solids. San Diego: Academic Press; 1985. p. 547-69.

[161] Kidwai O, Zhukovsky SV, Sipe JE. Effective-Medium Approach to Planar Multilayer Hyperbolic Metamaterials: Strengths and Limitations. Phys. Rev. A. 2012;85:053842.

[162] Kumar A, Low T, Fung KH, Avouris P, Fang NX. Tunable Light–Matter Interaction and the Role of Hyperbolicity in Graphene–Hbn System. Nano Lett. 2015;15:3172-80.

[163] Wang L, Meric I, Huang PY, Gao Q, Gao Y, Tran H, et al. One-Dimensional Electrical Contact to a Two-Dimensional Material. Science. 2013;342:614-7.

[164] Geick R, Perry CH, Rupprecht G. Normal Modes in Hexagonal Boron Nitride. Phys. Rev. 1966;146:543-7.

[165] Naik GV, Liu J, Kildishev AV, Shalaev VM, Boltasseva A. Demonstration of Al: Zno as a Plasmonic Component for near-Infrared Metamaterials. PNAS. 2012;109:8834-8.

[166] Joannopoulos JD, Johnson SG, Winn JN, Meade RD. Photonic Crystals: Molding the Flow of Light: Princeton university press; 2011.

[167] Ben-Abdallah P, Biehs S-A. Near-Field Thermal Transistor. Phys. Rev. Lett. 2014;112:044301.

[168] Basu S, Wang L. Near-Field Radiative Heat Transfer between Doped Silicon Nanowire Arrays. Appl. Phys. Lett. 2013;102.

[169] Biehs SA, Tschikin M, Ben-Abdallah P. Hyperbolic Metamaterials as an Analog of a Blackbody in the near Field. Phys. Rev. Lett. 2012;109:104301.

[170] Neuer G, Jaroma-Weiland G. Spectral and Total Emissivity of High-Temperature Materials. Inter. J. Thermophys. 1998;19:917-29.

[171] Dimitrakakis GK, Tylianakis E, Froudakis GE. Pillared Graphene: A New 3-D Network Nanostructure for Enhanced Hydrogen Storage. Nano Lett. 2008;8:3166-70.

[172] Lee J, Varshney V, Brown JS, Roy AK, Farmer BL. Single Mode Phonon Scattering at Carbon Nanotube-Graphene Junction in Pillared Graphene Structure. Appl. Phys. Lett. 2012;100.

[173] Liu X, Zhang RZ, Zhang Z. Near-Perfect Photon Tunneling by Hybridizing Graphene Plasmons and Hyperbolic Modes. ACS Photonics. 2014;1:785-9.

[174] Wang B, Zhang X, Yuan X, Teng J. Optical Coupling of Surface Plasmons between Graphene Sheets. Appl. Phys. Lett. 2012;100.

[175] Hwang EH, Das Sarma S. Dielectric Function, Screening, and Plasmons in Two-Dimensional Graphene. Phys. Rev. B. 2007;75:205418.

[176] Gan CH, Chu HS, Li EP. Synthesis of Highly Confined Surface Plasmon Modes with Doped Graphene Sheets in the Midinfrared and Terahertz Frequencies. Phys. Rev. B. 2012;85:125431.

[177] Ilic O, Jablan M, Joannopoulos JD, Celanovic I, Buljan H, Soljačić M. Near-Field Thermal Radiation Transfer Controlled by Plasmons in Graphene. Phys. Rev. B. 2012;85:155422.

[178] Jablan M, Soljacic M, Buljan H. Plasmons in Graphene: Fundamental Properties and Potential Applications. Proc. IEEE. 2013;101:1689-704.

[179] Rodriguez-Lopez P, Tse W-K, Dalvit DAR. Radiative Heat Transfer in 2d Dirac Materials. arXiv. 2014;1410:4387.

[180] Basu S, Zhang ZM. Ultrasmall Penetration Depth in Nanoscale Thermal Radiation. Appl. Phys. Lett. 2009;95.

[181] Das A, Pisana S, Chakraborty B, Piscanec S, Saha SK, Waghmare UV, et al. Monitoring Dopants by Raman Scattering in an Electrochemically Top-Gated Graphene Transistor. Nat. Nano. 2008;3:210-5.

VITA

ZIHAO (RICHARD) ZHANG

Zihao Zhang was born on November 1, 1987 in Wuxi, China. He received his Bachelor of Science degree in Mechanical Engineering from the Massachusetts Institute of Technology in June 2010. In August 2010, he began his graduate studies in the School of Mechanical Engineering at the Georgia Institute of Technology. He received a Master of Science degree in Mechanical Engineering in August 2013. His graduate work was partially funded by the National Science Foundation.

His research interests include and are not limited to: Transformation optics of thermal radiation, subwavelength imaging, and characterization of nanomaterials. He has published papers in Applied Physics Letters, ACS Photonics, Journal of Heat Transfer, Journal of Quantitative Spectroscopy and Radiative Transfer, and many others. These works have been presented at international symposia such as Micro/Nanoscale Heat & Mass Transfer Conference, NanoRad, etc. He is a member of the American Society of Mechanical Engineers and the American Physical Society.